

Continuous Low-Thrust Trajectory Optimization: Techniques and Applications

Mischa Kim

Dipl.Ing. – Technische Universität Wien – 2001
M.S. – Virginia Polytechnic Institute and State University – 2003

Dissertation submitted to the Faculty of the
Virginia Polytechnic Institute and State University
in partial fulfillment of the requirements for the degree of

Doctor of Philosophy
in
Aerospace Engineering

Dr. Christopher D. Hall, Committee Chair
Dr. Scott L. Hendricks, Committee Member
Dr. Hanspeter Schaub, Committee Member
Dr. Daniel J. Stilwell, Committee Member
Dr. Craig A. Woolsey, Committee Member

April 18, 2005
Blacksburg, Virginia

Keywords: Trajectory Optimization, Low-Thrust Propulsion, Symmetry

Copyright © 2005 by Mischa Kim

Continuous Low-Thrust Trajectory Optimization: Techniques and Applications

Mischa Kim

(ABSTRACT)

Trajectory optimization is a powerful technique to analyze mission feasibility during mission design. High-thrust trajectory optimization problems are typically formulated as discrete optimization problems and are numerically well-behaved. Low-thrust systems, on the other hand, operate for significant periods of the mission time. As a result, the solution approach requires continuous optimization; the associated optimal control problems are in general numerically ill-conditioned. In addition, case studies comparing the performance of low-thrust technologies for space travel have not received adequate attention in the literature and are in most instances incomplete. The objective of this dissertation is therefore to design an efficient optimal control algorithm and to apply it to the minimum-time transfer problem of low-thrust spacecraft. We devise a cascaded computational scheme based on numerical and analytical methods. Whereas other conventional optimization packages rely on numerical solution approaches, we employ analytical and semi-analytical techniques such as symmetry and homotopy methods to assist in the solution-finding process. The first objective is to obtain a single optimized trajectory that satisfies some given boundary conditions. The initialization phase for this first trajectory includes a global, stochastic search based on Adaptive Simulated Annealing; the fine tuning of optimization parameters – the local search – is accomplished by Quasi-Newton and Newton methods. Once an optimized trajectory has been obtained, we use system symmetry and homotopy techniques to generate additional optimal control solutions efficiently. We obtain optimal trajectories for several interrelated problem families that are described as Multi-Point Boundary Value Problems. We present and prove two theorems describing system symmetries for solar sail spacecraft and discuss symmetry properties and symmetry breaking for electric spacecraft systems models. We demonstrate how these symmetry properties can be used to significantly simplify the solution-finding process.

für mine eltra und min bruadr edi

Acknowledgments

I would like to acknowledge my advisor, and mentor Dr. Chris D. Hall, for giving me the opportunity to study at Virginia Tech. His guidance and motivation have been an integral part in helping me to pursue my career goals. I also wish to express my gratitude to the members of my committee, Dr. Scott L. Hendricks, Dr. Hanspeter Schaub, Dr. Daniel J. Stilwell, and Dr. Craig A. Woolsey for their patience and support.

I extend my appreciation and sincere thanks to all the professors that I had the pleasure to learn from during my time at Virginia Tech. I would like to thank the aerospace and ocean engineering staff of Mrs. Gail Coe, Mr. Luke Scharf, Mrs. Wanda Foushee, and Mrs. Betty Williams, who were always able to lend a helping hand whenever needed.

Furthermore, I must acknowledge the funding agencies who made my graduate career possible: NASA Goddard Space Flight Center, Society of Satellite Professionals International, Österreichisches Bundesministerium für Bildung, Wissenschaft und Kunst, Austrian Space Agency, and Virginia Space Grant Consortium.

Finally, and most importantly, I would like to thank those closest to me. I am greatly indebted to my parents and my brother Edgar for all the moral and loving support and for their unshakable confidence in my abilities. A very special thank-you goes to my girlfriend, Kim Locraft, for her dedication within the past year. She has given me relentless encouragement and has stood by my side through both the good times and bad times. Lastly, I thank all my friends for sharing with me some of the most precious moments of my life.

Contents

| | |
|---|-------------|
| Abstract | ii |
| Dedication | iii |
| Acknowledgements | iv |
| List of Figures | viii |
| List of Tables | xi |
| List of Symbols, Constants and Acronyms | xii |
| 1 Introduction | 1 |
| 1.1 Trajectory Optimization for Low-Thrust Space Travel | 1 |
| 1.2 Dissertation Objectives and Problem Statement | 2 |
| 1.3 Dissertation Overview | 3 |
| 2 Literature Review | 5 |
| 2.1 Trajectory Optimization via Direct Methods | 5 |
| 2.2 Trajectory Optimization via Indirect Methods | 8 |
| 2.3 Stochastic Trajectory Optimization | 10 |
| 2.4 New Trends and Developments in the Field of Trajectory Optimization . | 11 |
| 2.5 Summary | 13 |
| 3 Trajectory Optimization | 14 |
| 3.1 Low-Thrust Trajectory Optimization | 14 |
| 3.1.1 Trajectory optimization objectives | 15 |

| | | |
|----------|---|-----------|
| 3.1.2 | Low-thrust versus high-thrust trajectory optimization | 16 |
| 3.1.3 | Mission scenarios | 17 |
| 3.2 | Optimization Theory | 17 |
| 3.2.1 | The optimal control problem | 18 |
| 3.2.2 | Direct and indirect methods | 19 |
| 3.2.3 | Optimization techniques | 21 |
| 3.2.4 | Additional methods to solve MPBVP | 31 |
| 3.3 | Developing an Optimization Algorithm | 35 |
| 3.4 | Summary | 35 |
| 4 | System Models and Motion Equations | 37 |
| 4.1 | System Models | 37 |
| 4.2 | Electric Propulsion Spacecraft | 38 |
| 4.2.1 | Nuclear-electric propulsion systems | 40 |
| 4.2.2 | Solar-electric propulsion systems | 40 |
| 4.2.3 | Motion equations for electric propulsion system | 41 |
| 4.3 | Solar Sail Spacecraft | 42 |
| 4.3.1 | Solar radiation pressure model | 42 |
| 4.3.2 | Motion equations for solar sail system | 43 |
| 4.4 | Summary | 44 |
| 5 | Optimal Control Analysis | 45 |
| 5.1 | Two-dimensional Analysis | 45 |
| 5.1.1 | Nuclear-electric propulsion systems | 46 |
| 5.1.2 | Solar-electric propulsion systems | 48 |
| 5.1.3 | Solar sail spacecraft | 49 |
| 5.1.4 | Symmetry analysis | 50 |
| 5.1.5 | Results and propulsion system performance comparison | 54 |
| 5.2 | Three-dimensional Analysis | 62 |
| 5.2.1 | Nuclear-electric propulsion systems | 65 |
| 5.2.2 | Solar sail spacecraft | 70 |
| 5.2.3 | Coordinate transformation of solution trajectories | 73 |
| 5.2.4 | Defining a homotopy problem | 74 |
| 5.2.5 | Results and propulsion system performance comparison | 75 |
| 5.3 | Summary | 77 |

| | | |
|----------|--|------------|
| 6 | Work in Progress and Future Challenges | 80 |
| 6.1 | Integrating Satellite Attitude Dynamics | 80 |
| 6.2 | Control system design considerations | 81 |
| 6.3 | System models and motion equations | 82 |
| 6.4 | Optimal control analysis for solar sail spacecraft | 85 |
| 6.4.1 | Spacecraft design parameters | 86 |
| 6.4.2 | Optimality conditions | 87 |
| 6.4.3 | Singular control arc analysis | 88 |
| 6.5 | Optimal control analysis for nuclear-electric spacecraft | 90 |
| 6.6 | Simulation results | 91 |
| 6.7 | Summary and conclusions | 92 |
| 7 | Summary and Conclusions | 95 |
| | Bibliography | 98 |
| A | Optimal Control of Time-Continuous Systems | 108 |
| B | Nondimensional Motion Equations | 112 |
| C | Orbital Elements and Cartesian Coordinates | 115 |
| | Vita | 119 |

List of Figures

| | | |
|-----|--|----|
| 3.1 | Flowchart of the Adaptive Simulated Annealing algorithm | 24 |
| 3.2 | Interval reduction with Golden Section search algorithm | 27 |
| 3.3 | Numeric and algebraic continuation | 35 |
| 3.4 | Cascaded numerical algorithm for solving the optimal control problem . . | 36 |
| 4.1 | Dynamical systems representations in two dimensions | 39 |
| 4.2 | Dynamical systems representations in three dimensions | 39 |
| 5.1 | System symmetry shown with three transfer trajectories for $\beta = 0.33784$ | 53 |
| 5.2 | Transfer trajectory and solar sail orientation angle history for an Earth-to-Mars transfer with $\beta = 0.16892$ | 55 |
| 5.3 | Transfer trajectory and solar sail orientation angle history for an Earth-to-Mars transfer with $\beta = 0.33784$ | 56 |
| 5.4 | Transfer trajectory and thrust angle history for an Earth-to-Mars transfer with $\tau_0 = 0.16892$ and $\kappa = 0.50604$ | 56 |
| 5.5 | Transfer trajectory and thrust angle history for an Mars-to-Earth transfer with $\tau_0 = 0.16892$ and $\kappa = 0.50604$ | 57 |
| 5.6 | Transfer time as a function of target orbit radius for solar sail spacecraft (solid-dotted lines) and nuclear-electric propulsion spacecraft (solid lines). The initial orbit radius is 1 AU | 57 |
| 5.7 | Minimum-time Earth-Mars-Earth double orbit transfer trajectory and solar sail orientation angle history for $\beta = 0.33784$ | 59 |

| | | |
|------|--|----|
| 5.8 | Minimum-time Earth-Mars-Earth double orbit transfer trajectory and thrust angle history for $\tau = 0.16892$ and $\kappa = 1.01208$ | 59 |
| 5.9 | Minimum-time Mars-to-Earth rendezvous trajectories at first crossover point for $\beta = 0.135136$ | 60 |
| 5.10 | Minimum transfer time for Mars-to-Earth rendezvous for $\beta = 0.16892$. . | 61 |
| 5.11 | Minimum-time Mars-to-Earth rendezvous trajectories for second crossover point and for $\beta = 0.33784$ | 62 |
| 5.12 | Trajectory geometry comparison for sleep-type and catch-type solution trajectories for minimum-time Mars-to-Earth rendezvous for a solar sail spacecraft | 62 |
| 5.13 | Minimum transfer time for Earth-to-Mars rendezvous comparing solar sail spacecraft (solid-dotted lines) and nuclear-electric spacecraft (solid lines) | 63 |
| 5.14 | Minimum transfer time for Mars-to-Earth rendezvous comparing solar sail spacecraft (solid-dotted lines) and nuclear-electric spacecraft (solid lines) | 64 |
| 5.15 | Minimum transfer time for Earth-to-Mars rendezvous comparing solar-electric spacecraft (upward-triangle solid lines) and nuclear-electric spacecraft (solid lines) | 65 |
| 5.16 | Earth-to-Mars transfer trajectory and control angle histories for a solar sail spacecraft obtained from the corresponding transfer solution of a nuclear-electric spacecraft and using homotopy | 76 |
| 5.17 | Continuation parameter σ_i and continuation parameter step size $\Delta\sigma_i$ as a function of homotopy iteration step for the homotopy problem illustrated in Figure 5.16 | 76 |
| 5.18 | 3D Minimum-time Earth-to-Mars rendezvous for $\kappa = 0.50604$ and initial thrust of $\tau_0 = 0.16892$ for varying initial Earth-Mars constellations. . . . | 78 |
| 5.19 | Minimum transfer time for 3D Earth-to-Mars rendezvous for $\kappa = 0.50604$ and initial thrust of $\tau_0 = 0.16892$ (downward triangle solid lines) and $\tau_0 = 0.33784$ (upward triangle solid lines). The solid line corresponds to planar transfers for $\tau_0 = 0.16892$, $\kappa = 0.50604$ | 79 |
| 6.1 | Spacecraft control system design comparison | 82 |
| 6.2 | Interplanetary missions using solar sail spacecraft | 83 |

| | | |
|-----|---|-----|
| 6.3 | Transfer trajectory and solar sail orientation angle history for an Earth-to-Mars transfer. Simulation parameters are $\beta = 0.33784$, $\varsigma = 1$, and $\varepsilon = 1$ | 92 |
| 6.4 | Lagrange multipliers λ_i , nondimensional angular velocity ω and control torque g_u as a function of time for an Earth-to-Mars transfer. Simulation parameters are $\beta = 0.33784$, $\varsigma = 1$ and $\varepsilon = 1$ | 93 |
| 6.5 | Transfer trajectory and thrust vector angle history for an Earth-to-Mars transfer for a nuclear-electric spacecraft with $\tau_0 = 0.16892$, $\kappa = 0.50604$, and $\varphi = 1$ | 93 |
| C.1 | Cartesian Barycenter versus Orbital Element Barycenter location for a formation of two spacecraft | 116 |
| C.2 | Orbital elements | 117 |

List of Tables

| | | |
|-----|--|----|
| 4.1 | Solar-electric propulsion system performance parameters | 41 |
| 5.1 | Minimum transfer times and corresponding costates for Earth-to-Mars transfers | 55 |
| 5.2 | Partial transformation of initial condition of costate vector using control angles | 74 |
| 6.1 | Spacecraft design parameters for a 50 kg payload and a square solar sail . | 87 |

List of Symbols, Constants and Acronyms

Latin symbols:

| | | | |
|-----------------|--------------------------------------|----------------------|---|
| a | Semi-major axis | v | Velocity magnitude |
| b | Semi-minor axis | f | Homotopy function base |
| a_i, b_i, c_i | Arbitrary constants | h | Homotopy function |
| d | Distance | \mathbf{b}_\square | Unit vector in \square -direction in body reference frame |
| d_{cm} | Control force torque arm | \mathbf{e} | Eccentricity vector |
| d_u | Control distance | \mathbf{e}_\square | Unit vector in \square -direction in inertial reference frame |
| e | Eccentricity | \mathbf{f} | Motion equations RHS |
| f | True anomaly | \mathbf{f} or | Force vector |
| or | Force magnitude | \mathbf{f} | Combined state-costate motion equations RHS |
| g | Symmetry transformation of Lie group | \mathbf{g} | Gradient of cost function |
| or | Torque magnitude | \mathbf{h} | Specific angular momentum |
| i | Inclination | \mathbf{n} | Node vector |
| i, j, k | Integer numbers | \mathbf{n}_γ | Solar sail thrust vector direction |
| m | Spacecraft mass | \mathbf{n}_τ | Electric spacecraft thrust vector direction |
| m_p | Payload mass | \mathbf{o}_\square | Unit vector in \square -direction in orbital reference frame |
| m_s | Solar sail mass | \mathbf{p} | Deterministic search parameter |
| n | Integer number | \mathbf{r} | Position vector |
| p | Semi-latus rectum | \mathbf{s} | Search parameter step |
| q_i | Generalized coordinate vector | | |
| t | Time | | |
| t_0 | Initial time | | |
| t_f | Final time | | |

Latin symbols: CONTINUED

| | | | |
|-----------------|---|---------------------|--------------------------------------|
| \mathbf{u} | Control vector | \mathbf{R} | General rotation matrix |
| \mathbf{v} | Velocity vector | \mathbf{S} | Solar flux vector |
| \mathbf{x} | State vector | \mathbf{S}_\perp | Solar flux vector normal |
| \mathbf{x} | Combined state-costate vector | \mathcal{E} | Inertial reference frame |
| \mathbf{y} | Change-in-gradient vector | \mathcal{B} | Body-fixed reference frame |
| A | Solar sail surface area | \mathcal{O} | Orbital reference frame |
| A | Metropolis acceptance probability | \mathbb{H} | Approximated Hessian matrix |
| E | System energy | \mathbb{H} | Approximated inverse Hessian matrix |
| or | Eccentric anomaly | \mathbb{U} | Hessian update matrix |
| G | Lie group | \mathcal{H} | System Hamiltonian |
| H | Hessian of cost function | \mathcal{J} | Performance index |
| H | Acceptance probability | \mathcal{J}^+ | Augmented performance index |
| I_\square | Moment of inertia about the \square -axis | \mathcal{J}^\star | Extended augmented performance index |
| I_{sp} | Specific impulse | \mathcal{L} | Accumulated cost function |
| M | Mean anomaly | \mathcal{S} | Switching function |
| P | Spacecraft electric power | \mathcal{L} | Lagrangian |
| P | Probability density of parameter space | \mathcal{T} | Kinetic energy |
| Q_i | Generalized forces | \mathcal{V} | Potential energy |
| T | Transfer time | \mathcal{P}_i | i th problem family |
| or | Spacecraft thrust | I | Interval |
| C_i | Single-axis rotation matrix about i th axis | \mathbf{U} | Control vector space |
| | | \mathbf{X} | State space |

Greek symbols:

| | | | |
|---------------|--|---------------|--|
| α_{ij} | Spacecraft control angle | ϵ | Weighing constant |
| β | Characteristic acceleration of solar sail spacecraft | ε | Group transformation parameter |
| γ | Photon | ζ | Control panel deflection angle |
| γ_a | Fraction of absorbed γ | η | Random number, $\eta \in [0, 1]$ |
| γ_d | Fraction of diffusely reflected γ | η_i | Acceptance measure at i th annealing level |
| γ_s | Fraction of specularly reflected γ | θ | Azimuth angle |

Greek symbols: CONTINUED

| | | | |
|-------------|---|-----------|--|
| ϑ | Annealing temperature | σ | State-control variable constraint vector |
| κ | Thrust efficiency parameter | ψ | One-sided boundary conditions on the states |
| μ | Mass flow function | ψ_0 | Initial boundary conditions on the states |
| ν | Spacecraft orientation angle | ψ_f | Final boundary conditions on the states |
| ρ | Solar sail mass density | Γ | Solution trajectory |
| ϱ | Step length parameter | Δ | System of differential equations |
| σ | Continuation parameter | Θ | Initial angular reference location of celestial body |
| ς | Gravity gradient form factor | Λ | One-parameter group transformation of independent variable |
| τ | Specific thrust | Φ | Vector field |
| v | Step length in search direction | Ξ | Ratio of final to initial orbit radii |
| ϕ | Elevation angle | Π | Permutation |
| or | Terminal cost function | Ω | One-parameter group transformation of dependent variable |
| φ | Thrust vector torque | or | Right ascension of the ascending node |
| χ | Cost function | Λ | Costate vector space |
| ω | Angular velocity | Γ | Orbital elements to cartesian coordinates mapping |
| or | Argument of perigee | Ψ | Boundary conditions on the states |
| α | Control angles vector | Ψ | Boundary conditions on combined states-costates vector |
| ζ | Search direction | | |
| ι | Interior-point boundary conditions on the states | | |
| λ | Costate vector | | |
| μ | Vector of dependent variable | | |
| ν | Boundary conditions Lagrange multipliers | | |
| ξ | Vector of independent variable | | |
| or | Statistical search parameter | | |
| π | Interior-point boundary conditions Lagrange multipliers | | |

Special symbols:

| | | | |
|-----------|----------------------------|------------|----------------------------|
| \oplus | Center of mass | \odot | Sun |
| \ominus | Center of pressure | \odot | Vector of orbital elements |
| \otimes | Orbital element barycenter | Υ | Vernal equinox direction |

Mathematical notation:

| | | | |
|-----------------------|------------------------------|--------------------------|---|
| \square | Arbitrary variable | \square' | $(d/d\tilde{t})\square$ |
| $*\square, \square^*$ | Intermediate variables | $\partial\square$ | Partial differential of \square |
| $[\square]$ | Numerical value of \square | $\nabla\square$ | Gradient of \square |
| $[\square]$ | Physical unit of \square | \square^k | k th power of \square |
| (\square) | Vector | $\square^{(k)}$ | k th derivative of \square |
| $[\square]$ | Matrix | $\text{pr}^{(k)}\square$ | k th prolongation of \square |
| $[\square]^{-1}$ | Matrix inverse | $\exp\square$ | Exponential of \square |
| \square^T | Transpose of \square | $\cos\square$ | Cosine of \square |
| $\tilde{\square}$ | Dimensional \square | $\sin\square$ | Sine of \square |
| $\hat{\square}$ | Transformed \square | $\tan\square$ | Tangent of \square |
| $\bar{\square}$ | Upper bound of \square | $\text{atan}\square$ | Arctangent of \square , $\in [-\pi/2, \pi/2]$ |
| \square^* | Optimal \square | $\text{atan2}\square$ | Arctangent of \square , $\in [0, 2\pi]$ |
| \square° | Singular optimal \square | <i>iff</i> | “...if and if only...” |
| $\delta\square$ | Variation of \square | \in | Element of a set |
| $\Delta\square$ | Difference in \square | \subset | Subset |
| $\text{abs}\square$ | Absolute value of \square | $[\square] > 0$ | Positive definite matrix |
| $\text{arg}\square$ | Argument of \square | $\mathbf{1}$ | Unity matrix |
| $\text{max}\square$ | Maximum of \square | \mathcal{O} | Order symbol |
| $\text{min}\square$ | Minimum of \square | \mathbb{N} | Set of positive integer numbers |
| $\text{sign}\square$ | Sign of \square | \mathbb{R} | Set of real numbers |
| $\ \square\ _p$ | p -Norm of \square | \mathbb{R}^n | n -dimensional real vector space |
| $\ \square\ $ | 2-Norm of \square | \mathbb{Z} | Set of integer numbers |
| $\dot{\square}$ | $(d/dt)\square$ | | |

Sub- and superscripts:

| | | | |
|------|-----------------------|----------|-------------------------|
| 0 | ↓ initial | per | ↓ periapsis |
| a | ↓ absorbed | s | ↓ specularly reflected |
| cart | ↓ cartesian | spher | ↓ spherical |
| cm | ↓ center of mass | u | ↓ upper |
| d | ↓ diffusely reflected | or | ↓ controlled |
| f | ↓ final | γ | ↓ solar sail spacecraft |
| G | ↓ gravity gradient | τ | ↓ electric spacecraft |
| l | ↓ lower | max | ↑ maximum |

Sub- and superscripts: CONTINUED

| | | | |
|-----|-----------|-----|-------------|
| min | ↑ minimum | pes | ↑ pessimal |
| opt | ↑ optimal | ref | ↑ reference |

Constants:¹

Astronomical unit distance

$$\text{AU} = 1.49597870691 \times 10^{11} (\pm 3) \text{ m}$$

Gravitational acceleration at Earth's surface

$$g_0 = 9.80665 \text{ (exact by definition)} \frac{\text{m}}{\text{s}^2}$$

Gravitational constant

$$G = 6.67259 \times 10^{-11} (\pm 3 \times 10^{-15}) \frac{\text{m}^3}{\text{kg s}^2}$$

Mass of Sun

$$M = 1.98893 \times 10^{30} (\pm 59 \times 10^{25}) \text{ kg}$$

Nominal solar radiation pressure at 1 AU⁶¹

$$p_\gamma = 4.563 \times 10^{-6} \frac{\text{N}}{\text{m}^2}$$

Sidereal year (quasar reference frame)

$$T_{\text{sid}} = 365.25636 \text{ days}$$

Time unit

$$\text{TU} = T_{\text{sid}}/(2\pi) = 58.13223 \text{ days}$$

Heliocentric gravitational constant

$$\mu_\odot = GM = 1.32713430118 \times 10^{20} (\pm 8 \times 10^9) \frac{\text{m}^3}{\text{s}^2}$$

The number π ²

$$\pi = 3.1415926535897932384626433832 \text{ (accurate to 29 digits)}$$

Golden ratio²²

$$\varpi = 2/(1 + \sqrt{5})$$

¹ http://ssd.jpl.nasa.gov/astro_constants.html

² The current world record marked by Kanada et. al. computes π to 1,241,100,000,000 digits accuracy – <http://pi2.cc.u-tokyo.ac.jp>

Acronyms:

| | | | |
|--------|---|--------|---|
| AAS | American Astronautical Society | JPL | Jet Propulsion Laboratory |
| AIAA | American Institute of Aeronautics and Astronautics | NASA | National Aeronautics and Space Administration |
| ASA | Adaptive Simulated Annealing | NPDOT | Nonlinear Programming for Direct Optimization of Trajectories |
| AU | Astronomical unit | MPBVP | Multi-Point Boundary Value Problem |
| BFGS | Broyden-Fletcher-Goldfarb-Shanno | NSTAR | NASA Solar Electric Propulsion Technology Application Readiness |
| BC | Boundary conditions | RAPTOR | Rapid Trajectory Optimization Resource |
| BVP | Boundary value problem | RHS | Right-hand side |
| COV | Calculus of Variations | 3BP | Three-Body Problem |
| CR3BP | Circular-Restricted Three-Body Problem | SA | Simulated Annealing |
| CTOP | Chebyshev Trajectory Optimization Program | SEPTOP | Solar Electric Propulsion Trajectory Optimization Program |
| DFP | Davidon-Fletcher-Powell | SNOPT | Sparse Nonlinear Optimizer |
| DU | Distance unit | SOCS | Sparse Optimal Control Software |
| FC | Final conditions | STOUR | Satellite Tour Design Program |
| GA | Genetic algorithm | TCM | Trajectory Correction Maneuver |
| GALLOP | Gravity-Assist Low-thrust Local Optimization Program | TPBVP | Two-Point Boundary Value Problem |
| GALTOP | Gravity Assisted Low Thrust Optimization Program | TU | Time unit |
| GEO | Geostationary Earth orbit | UNCMIN | Unconstrained Minimization |
| HILTOP | Heliocentric Interplanetary Low Thrust Optimization Program | | |
| IC | Initial conditions | | |
| IBFGS | Inverse Broyden-Fletcher-Goldfarb-Shanno | | |

Introduction

Deep-space exploration missions require large velocity increments and therefore demand for sophisticated, capable propulsion technologies. Mission designs using state-of-the-art high-thrust propulsion technologies (such as chemical propulsion systems) in combination with gravity assist maneuvers typically feature complicated and inflexible mission profiles. Low-thrust propulsion systems, on the other hand, can significantly enhance mission feasibility by using propellant more efficiently. As a direct consequence, low-thrust propulsion systems provide significantly larger velocity increments, which in turn allows for an increased spacecraft payload ratio and/or a considerably decreased spacecraft volume and therefore launch vehicle size.

1.1 Trajectory Optimization for Low-Thrust Space Travel

One of the most important tasks during the analysis and design of space missions is the design and optimization of suitable mission trajectories. This dissertation addresses the problem of computing optimal interplanetary trajectories for continuous, low-thrust spacecraft. Generally, optimality is defined with respect to a set of mission constraints such as mission time and overall propellant consumption. Solar sail spacecraft^{61,104} do not consume propellant; as a result solar sail mission trajectories are typically optimized with respect to transfer time, only. In the case of electric spacecraft, optimization problems are in general less straightforward to formulate because for typical applications both mission

time and propellant consumption need to be taken into account but are (in general) subject to competing mission constraints.

Except for a small number of “academic” problems spacecraft trajectories in general and optimal spacecraft trajectories in particular are obtained from the numerical integration of a set of differential equations describing the system dynamics. These differential equations typically account for inertial force terms as well as force terms due to control variable inputs (e.g. control thrust or torque). Therefore, the optimization problem is to find an “optimizing” function of the control variables that results in an optimized trajectory solution.

Compared to low-thrust spacecraft optimization problems, optimal control problems for high-thrust systems are relatively straightforward. With high-thrust spacecraft the duration of (control) thrust arcs is usually short in comparison to the mission time. As a result, thrust arcs are typically modeled as isolated, singular events justifying the usage of discrete optimization theory to obtain optimal trajectories. Low-thrust propulsion systems, on the other side, operate for a significant part of the overall mission time. Consequently, the control variables need to be modeled as continuous functions requiring tools based on continuous optimization to solve optimal control problems adequately.

Several strategies have been suggested and used in the literature to solve continuous optimization problems for spacecraft transfer applications. Indirect approaches based on the *Calculus of Variations* (COV) provide a means to formulate optimal control problems as low-dimensional, discrete optimizations problems. However, convergence characteristics of trajectory optimization techniques based on the Calculus of Variations heavily depend on the “quality” of the initial guess of optimization parameters as well as the skill level of the individual operating the optimization tool. As a consequence, the search for optimized trajectories for continuous low-thrust spacecraft is typically a rather tedious and time-consuming process.

1.2 Dissertation Objectives and Problem Statement

In light of the drawbacks of traditional trajectory optimization methods and algorithms discussed in the previous section we devise a new optimization scheme with the goal of enhancing the versatility of existing software tools, thereby simplifying and accelerating the solution finding process. This is achieved by combining the globality of a stochastic search algorithm – Simulated Annealing (SA) – with the efficiency of local, deterministic

optimizers based on Quasi-Newton and Newton methods. The novelty of our optimization algorithm is the implementation of analytic and semi-analytic techniques such as symmetry and homotopy methods, which are used to great advantage to compute a wide variety of optimized transfer trajectories starting with a single solution trajectory. In fact, the main idea behind the proposed algorithm is that the global optimization problem has to be solved only once, for a particular spacecraft system. Emanating from this initial solution we compute solution trajectories for arbitrary boundary conditions and even different spacecraft system models by relying exclusively on homotopy and symmetry methods.

The primary research objective is to validate the optimization algorithm and to prove its efficiency. We employ the optimization algorithm to analyze the continuous, minimum-time, low-thrust spacecraft transfer problem for interplanetary travel. We consider several different low-thrust propulsion technologies, namely, solar-electric, nuclear-electric and solar sail propulsion systems. A comparative analysis between the different spacecraft system models addresses the secondary research objective of evaluating the performance of low-thrust propulsion technologies for interplanetary missions.

1.3 Dissertation Overview

The dissertation is organized as follows:

In Chapter 2 we briefly summarize research related to the field of trajectory optimization. We discuss some papers on direct methods in Section 2.1 and then focus on optimization techniques based on indirect approaches in Section 2.2. In Section 2.3 we review some works on trajectory optimization via stochastic algorithms and conclude the chapter by discussing recent developments in optimal control theory.

Chapter 3 develops the framework for the devised optimization algorithm. We formulate the general optimal control problem in Section 3.1 and discuss in detail techniques and algorithms used for our optimization tool in Section 3.2. We introduce Adaptive Simulated Annealing (ASA) and describe local optimizers in Section 3.2.3. Section 3.2.4 is devoted to the theory and implementation of homotopy and symmetry methods.

System models are developed in Chapter 4 for two- and three-dimensional analysis for electric and solar sail spacecraft. Motion equations for nuclear-electric and solar electric spacecraft models are derived in Section 4.2. Section 4.3 focuses on the derivation of

equations of motion for solar sail spacecraft.

Chapter 5 forms the main part of the dissertation. We mathematically formulate and solve optimal control problems in two dimensions in Section 5.1 and extend the analysis to three dimension in Section 5.2. We demonstrate the usage of symmetry and homotopy methods to solve the optimal control problem and present new solution families to the minimum-time transfer problem.

Extensions to the system models investigated in Chapter 5 are studied in Chapter 6. In Section 6.1 we analyze optimal control problems for spacecraft models including the attitude dynamics.

Chapter 7 summarizes the findings of this research effort and concludes with recommendations for future work.

In Appendix A we review the theory of continuous trajectory optimization. Appendix B provides a short tutorial demonstrating the process of non-dimensionalization of differential equations. Finally, in Appendix C we discuss the functional relationship between cartesian coordinates and the set of orbital elements.

Literature Review

In this chapter we briefly summarize the works related in the field of trajectory optimization. First we review some papers analyzing the optimal control problem via direct methods and discuss some of the more advanced optimization software packages. Subsequently, we discuss results of trajectory optimization problems obtained using indirect approaches and then present some works analyzing optimal control problems with stochastic optimization algorithms. The last section of this chapter is devoted to new trends and recent developments in the field trajectory optimization.

Two survey papers for optimal control theory and trajectory optimization methods are of particular interest and deserve mentioning. The paper by Betts⁵ gives a brief overview of the most common and popular numerical methods to solve trajectory optimization problems. One of the final paragraphs of his paper is devoted to trajectory optimization methods based on genetic algorithms (GA). Interestingly, the author classifies these stochastic techniques as not being overly appropriate for trajectory optimization problems and as computationally inferior when compared to methods using gradient information. The survey paper by Paiewonsky⁷¹ approaches optimal control problems from a broader perspective and is oriented to aeronautical and astronautical applications alike.

2.1 Trajectory Optimization via Direct Methods

Early research efforts to develop trajectory optimization tools based on direct methods date back to the 1980's. To the author's best knowledge, Hargraves and Paris³² first

implemented optimization algorithms based on embedded collocation schemes to solve a wide variety optimal control problems.

Interestingly, half a decade earlier Bahls and Paris² had introduced a mission analysis tool to investigate complex interplanetary missions using low-thrust propulsion technologies. Unsatisfied with the performance and flexibility of existing optimization packages based on indirect methods Bahls and Paris, suggested a direct approach using trajectory segmentation. Their research effort led to the development of the Gravity Assisted Low Thrust Optimization Program (GALTOP). With GALTOP individual thrust arcs were computed using Chebyshev collocation and subsequently patched together satisfying appropriate sets of boundary conditions. When compared to then state-of-the-art optimizer based on indirect methods such as HILTOP (Heliocentric Interplanetary Low Thrust Optimization Program), Bahls and Paris reported a typical improvement in required computation time of up to 30% and classified GALTOP to be “... *accurate enough for useful results and trends to be discerned.*”

In 1987, Hargraves and Paris developed an optimization algorithm based on direct methods introducing – according to Herman and Spencer³⁷ – the new concept of *collocation* or *direct transcription*. In their approach, Hargraves and Paris used linear interpolation for the control variables and a third-order Hermite interpolation for the state vector. Various higher-order interpolation schemes were compared but were found to be less suitable when implemented in the authors’ optimization package NPDOT (Nonlinear Programming for Direct Optimization of Trajectories). NPDOT was validated against the software code CTOP (Chebyshev Trajectory Optimization Program) and provided comparable performance with respect to computation time.

A paper by Betts and Erb⁶ demonstrated the full potential of advanced algorithms based on collocation when applied to complex systems. Specifically, the authors analyzed optimal (minimum-time and minimum-fuel scenarios) low-thrust trajectories for Earth-Moon transfers for solar-electric propulsion spacecraft and using a thrust-coast-thrust sequence. The authors used the Sparse Optimal Control Software (SOCS) capable of solving general, sparse, and large-scale optimization problems.³ Betts and Erb discussed the importance of an accurate initial set of optimization parameters and proposed a discretization scheme suitable for spiral-type transfer trajectories. As outlined in their paper, SOCS proved to be a computationally efficient tool to solve the optimal control problem with 211,031 variables and 146,285 constraints for the final mesh-refined system description. Compared

³ SOCS is Boeing’s prime trajectory optimization tool and offers advanced system modeling capabilities to account, for example, for perturbation effects due to celestial bodies and the Earth oblateness; SOCS also provides an integrated mesh refinement algorithm.

to the study performed by Schoenmaekers et al.⁸⁵, Betts and Erb’s analysis resulted in an improvement in transfer time of approximately 40% with an increased fuel consumption of 25%, which was attributed to the fact that Schoenmaekers et al. used a multiple-thrust-arc approach.^{53,108}

Higher-order collocation methods were studied by Herman and Spencer³⁷ for optimal, low-thrust, thrust-coast-thrust Earth-orbit transfers. More specifically, the authors implemented the so-called Higher-Order Collocation 7th degree system model with SNOPT, an optimization package for large-scale, nonlinear programming problems. The results of the investigation were compared to earlier studies performed by the second author. The algorithm developed by Herman and Spencer resulted in an increase in Δv performance of 10% on average and as high as 14%.

McConaghy et al.⁶⁰ analyzed more complex mission scenarios for low-thrust missions using solar-electric propulsion. In their paper, the authors combined the benefits of low-thrust propulsion technologies and gravity-assist maneuvers as means to reduce fuel consumption and to shorten mission duration. The global search for optimal trajectories was performed using the STOUR (Satellite Tour Design Program) software package; the GALLOP (Gravity-Assist Low-thrust Local Optimization Program) optimization tool was used for the local search. The algorithm was compared to SEPTOP (Solar Electric Propulsion Trajectory Optimization Program, developed by Carl Sauer of JPL) a software package based on indirect methods. Both optimization packages showed comparable performance characteristics and to be in good agreement with respect to propellant consumption and overall mission time.

Kluever⁵² studied the geostationary orbit transfer problem with specific impulse modulation for solar-electric spacecraft using Hall thrusters. The author used a direct method discretizing the state and costate time histories of the corresponding Two-Point Boundary Value Problem (TPBVP). He obtained several maximum-payload, geostationary Earth-orbit transfers with an 5–6% improvement in propellant usage as compared to fixed specific impulse engines. The decrease in required propellant however came at the cost of increased transfer times of up to 30% and additional electronic hardware requirements.

Fiehler and Oleson²¹ used direct methods to compare the performance of solar-electric spacecraft using Hall and ion propulsion systems. The authors analyzed Earth-Mars transfers with a thrust-coast-thrust profile and concluded that “... *the Hall thruster delivered more payload mass at the shortest trip times and the ion thruster delivered more mass at the longest trip times [for the mission scenarios considered]*”. However, for the analyzed transfer options, the power levels for the Hall thruster was on average 10% less

than the power levels for the ion thruster. Comparing the performance of solar-electric spacecraft to conventional, chemically propelled spacecraft, Fiehler and Oleson noted that for typical Earth-Mars transfer times of about 200 days chemical propulsion systems could be considered an equitable transfer option with respect to delivered payload mass.

Options for optimal transfers to the outer planets have been studied by Vasile et al.⁹⁷ In particular, the authors compared two classes of mission options: chemical propulsion spacecraft using aero-gravity assist maneuvers and nuclear-electric spacecraft using gravity assist maneuvers. The trajectory optimization problem was solved via direct method using a software package developed by the first author.⁹⁶

2.2 Trajectory Optimization via Indirect Methods

Indirect methods have been successfully applied to a wide variety of low-thrust trajectory optimization problems. Kechichian⁴³ analyzed the minimum-time, rendezvous problem for constant acceleration spacecraft based on non-singular, equinoctial orbital elements. The author used the UNCMIN⁴ (Unconstrained Minimization) package to calculate three-dimensional, near-GEO-to-GEO transfer trajectories. In an earlier paper, Kechichian⁴² studied the time-fixed, minimum-fuel transfer problem for bounded thrust, again, based on a set of non-singular, equinoctial orbital elements. For this problem, Kechichian considered both thrust magnitude and thrust direction as control variables with constant power levels. Starting with optimal transfers for unbounded thrust levels, the author obtained corresponding solution trajectories for bounded thrust levels which resulted in a slight improvement in total propellant consumption. Guelman^{25,26} analyzed the related problem of power-limited, minimum-time Earth-to-Moon transfers. He considered both Moon impact and Moon orbit injection scenarios within the Circular-Restricted Three-Body Problem (CR3BP). The trajectories were obtained by considering a sequence of Two-Body Problems, one at a time, and subsequently patching together the individual trajectory segments.

Optimal low-thrust maneuvers in the presence of Earth shadowing effects were studied by Colasurdo and Casalino¹⁷. The authors considered circular-to-circular transfers and compared analytical solutions to numerically computed results obtained via indirect methods. The paper also studied the dual problem of maximizing the eccentricity

⁴ UNCMIN is a software package for solving unconstrained optimization problems via the Quasi-Newton method using the BFGS update formula to compute the approximated Hessian matrix.

change while maintaining a constant semi-major axis. Nah and Vadali⁶⁵ investigated three-dimensional, fuel-optimal Earth-to-Mars trajectories for variable specific impulse propulsion systems. They used a multiple-shooting approach and Newton’s method to optimize individual trajectory segments in the general four-body problem of Sun, Earth, Moon, and spacecraft. The spacecraft design considered a fast⁵ human transit to Mars including a 10 MW nuclear power plant, a propulsion system with maximum specific impulse of 35,000 s, and an initial spacecraft mass of 525,000 kg.

A more theoretically motivated minimum-fuel orbit transfer problem was investigated by Oberle and Taubert⁶⁹. In particular, the authors analyzed the existence of multiple optimal control solutions for Earth-to-Mars and Mars-to-Earth trajectories by considering transfer options with multiple thrust and coast arcs. Oberle and Taubert considered planar, circular-to-circular transfers with thrust magnitude and thrust direction as the control variables. They proved the existence of fuel-optimal solutions for prescribed, upper-bounded transfer times and solved the optimization problem using the multiple-shooting BNDSCO software code. The authors obtained and classified various solution families characterized by an increasing number of thrust and coast arcs. They noted that the problem was of less practical interest since an increase in the number of thrust and/or coast arcs resulted in an increase in transfer time while keeping the fuel consumption unchanged.

Caillau et al.¹⁰ treated the problem of minimum-time geosynchronous transfers for low-thrust spacecraft. The authors used continuation methods on the thrust to calculate fuel-efficient multi-revolution transfer trajectories. To justify the homotopy approach the authors studied the dependence of the cost function on the bound of the control variables. The optimization problem was solved with single-shooting and using a Hybrid-Powell method. Solution trajectories were first obtained for planar low-thrust transfers with high maximum thrust levels. From these solutions Caillau et al. showed how to compute more general, three-dimensional transfer trajectories for decreasing values of maximum thrust levels.

Trajectory optimization problems for solar sail spacecraft have been analyzed by several research teams over the past five decades.^{12,38,50,54,57,92,93} The first solar sail trajectories were calculated by Tsu⁹⁴ and London⁵⁷. Tsu investigated various means of propulsion and showed that in many cases solar sails show superior performance when compared to chemical and ion propulsion systems. The author used approximated heliocentric motion equations to obtain spiraling trajectories for a “. . . *fixed sail setting*”. London presented

⁵ Typical one-way Earth-to-Mars transfer times for exhaust-modulated plasma rocket spacecraft are as short as 90-110 days according to Chang-Díaz et al.¹⁴

similar spiral solutions for Earth-Mars transfers with constant sail orientation using the exact equations of motion. Optimal solar sail trajectories were first computed by Zhukov and Lebedev¹⁰⁷ for interplanetary missions between coplanar circular orbits. In 1980 Jayaraman⁴¹ published similar minimum-time trajectories for transfers between the Earth and Mars. He used a penalty function approach using a conjugate gradient method. Two years later, Wood et al.¹⁰³ presented an analytical proof to show that the orbital transfer times obtained by Jayaraman were incorrect due to the incorrect application of a transversality condition of variational calculus and an erroneous control law. About two decades later Powers et al.⁷⁷ and Powers and Coverstone⁷⁶ obtained results similar to those reported in Wood's paper, but evidently used the same incorrect control law used in Jayaraman⁴¹. The more general time-optimal control problem of three-dimensional, inclined and elliptic departure and rendezvous planet orbits was discussed by Sauer⁸³.

Minimum-time trajectories for compound and non-ideal solar sail spacecraft were analyzed by McInnes⁶² and Colasurdo and Casalino¹⁶, respectively. McInnes studied the effect of different solar sail configuration on delivered payload with minimum-time Earth-to-Mars transfers. According to the author, compound solar sail configurations could theoretically offer greater performance than conventional "flat" solar sails by using a large, sun-facing collector that directs the solar flux onto a smaller secondary directing mirror. McInnes presented motion equations for the compound solar sail configuration as an extension of the flat sail arrangements. His results showed an increase in delivered payload mass of up to 30% for typical transit times of 300 days for Earth-to-Mars transfers. The performance of non-ideal solar sails were investigated by Colasurdo and Casalino. The solar sail performance was measured with a constant efficiency parameter that enters the system motion equations as a multiplicative coefficient. Not surprisingly, the authors obtained results similar to those reported earlier in the literature.

2.3 Stochastic Trajectory Optimization

Williams and Coverstone-Carroll¹⁰¹ studied the minimum-fuel problem for solar-electric propulsion spacecraft using a genetic algorithm approach. They analyzed various transfer options for Earth-to-Mars and Mars-to-Earth mission for NSTAR-type (NASA Solar Electric Propulsion Technology Applications Readiness Program) satellite configurations for constant flight times between 1.5 and 3.0 years. The authors used a two-body dynamics model and an optimization approach based on an indirect method. Trajectories were optimized using the SEPTOP (Solar Electric Propulsion Trajectory Optimization Program) software code combined with a genetic algorithm previously studied by Hart-

mann et al.^{34,35} The results confirmed the feasibility of interplanetary missions using solar-electric spacecraft when compared to conventional, chemically propelled spacecraft systems. The study also revealed the advantages of using stochastic algorithms to solve trajectory optimization problems especially for more complex missions scenarios. A similar analysis was performed by Wuerl et al.¹⁰⁵ The authors used the software tool RAPTOR (Rapid Trajectory Optimization Resource) combining the strengths of genetic algorithms with the rapid convergence behavior of the Quasi-Newton methods. The performance of the genetic algorithm was further enhanced by implementing a Baldwinian learning strategy enabled by the use of an active feedback from the deterministic optimizer.

Lu and Khan⁵⁸ and Tekinalp and Bingol⁹⁰ used Simulated Annealing for the global search of optimized trajectories. In their paper, Lu and Khan analyzed various minimum-time maneuvers for advanced fighter aircraft via direct methods. The control variables were parameterized using cubic spline functions resulting in a high-dimensional optimization problem. According to the authors, the search algorithm showed good convergence characteristics and performed well when compared to the Principal Axis method and the Nelder-Mead Simplex. Tekinalp and Bingol investigated the missile optimization problems and in particular the missile trajectory optimization problem. They used an adaptive Simulated Annealing algorithm and implemented a direct method to solve the optimal control problem. The authors compared two formulations for maximum-range missile trajectories and showed how to embed the trajectory optimization problem into the general missile optimization problem.

2.4 New Trends and Developments in the Field of Trajectory Optimization

The direct methods discussed in Section 2.1 are based on the idea of locally approximating polynomials for the state, costate, and control variables. In recent years the concept of using globally orthogonal polynomials has gained in importance and received increasing attention in the literature.^{79,80,81,98,99} Globally orthogonal polynomials offer an alternative approach of transforming trajectory optimization problems into nonlinear programming problems and provide the means to conveniently reformulate optimal control problems as problems involving systems of purely algebraic equations. One of the benefits of using globally orthogonal polynomials functions such as the Legendre and Chebyshev polynomials lies in the fact that the same order of accuracy for the states and costates is guaranteed, which is usually not the case for transcription methods using a locally

approximating polynomial function description. As a result, costate information is in general available to relatively high accuracy providing a “good” initial set of optimization parameters for subsequent usage in indirect methods.

Early work dates back to the 1960s when Urabe⁹⁵ proposed a method based on Chebyshev polynomials to solve Multi-Point Boundary Value Problems (MPBVP). Vlassenbroeck⁹⁸ and Vlassenbroeck and Van Dooren⁹⁹ applied the concept of Chebyshev polynomials to solve optimal control problems and in particular the minimum-time, low-thrust, planar Earth-to-Mars transfer problem. The authors compared the performance of the method to other techniques based on direct approaches and concluded that their algorithm showed superior performance in terms of accuracy and required computation time. Ross and Fahroo⁸⁰ developed the so-called Legendre Pseudospectral method. The method was implemented in the software package DIDO⁸² and applied to a variety of optimization problems. Stevens and Ross⁸⁹, for example, investigated the minimum-time problem of Earth-Mars cyclers using solar sail spacecraft and showed the efficiency of DIDO⁶ with trajectory optimization problems. Mendy⁶³ applied the software package to validate a multi-satellite optimization model for spacecraft formation control based on a single-satellite model.

A different approach of solving optimal control problems makes use of the Hamiltonian structure of the optimality conditions as derived via the variation of calculus. With this approach generating functions are determined as a complete integral of the Hamilton-Jacobi or the Hamilton-Jacobi-Bellman equation.

Popescu⁷⁵ applied the theory of canonical transformations to the study of optimal, elliptic orbit transfers. The author proposed an algorithm for obtaining a set of canonical constants that defines the coast arc and analyzed nonsingular arcs for minimum-time trajectories in the Keplerian two-body system. The study was somewhat limited as it only considered the control of the system during periods of null control.

The work of Scheeres et al.⁸⁴ builds on the results reported by Popescu and extends the analysis to be applicable to a wider spectrum of optimal control problems. In particular, the authors showed that certain solutions to the Hamilton-Jacobi equation can directly yield optimal control laws for a general system. The algorithm proposed by the authors provided a means to compute the initial costate vector for arbitrary boundary conditions by algebraic manipulations of the corresponding generating function. They applied the algorithm to the fixed-time transfer problem in the presence of a central gravitational field

⁶ Named after Dido, Queen of Carthage, supposedly the first individual to formulate and solve an (isoperimetric) optimization problem.

minimizing a quadratic cost function of the control variables. In a related paper, Guibout and Scheeres²⁷ solved the problem of nonlinear targeting of a formation of spacecraft by analyzing the associated Two-Point Boundary Value Problem via the Hamilton-Jacobi equations. The authors showed how direct solutions for the Taylor series expansion of the corresponding generating function can be obtained from a nominal, numerically computed initial trajectory. The algorithm was applied to the reconfiguration problem of a spacecraft system about the libration point in the Hill's Three-Body Problem.

2.5 Summary

We have reviewed in this chapter much work related to the field of trajectory optimization. We have discussed analyses using direct and indirect approaches for solving optimal control problems and introduced literature on stochastic trajectory optimization. With the acquired expertise we now proceed to develop an optimization algorithm.

Trajectory Optimization

In this chapter, we formulate and characterize the low-thrust trajectory optimization problem and show how low-thrust trajectory optimization problems are traditionally solved by using optimal control theory. In Section 3.1 we state the trajectory optimization problem from a general point of view and from the perspective of optimal control theory. We place special emphasis on potential objectives for trajectory optimization and on differences between high-thrust and low-thrust trajectory optimization. We show that low-thrust trajectory optimization is equivalent to the search for optimal control functions in an infinite dimensional function space, a numerically difficult problem. Section 3.2 presents a brief survey on trajectory optimization methods. We discuss Adaptive Simulated Annealing, a stochastic technique for global optimization and local search techniques such as Newton and Quasi-Newton methods. In addition, we show how symmetry and homotopy methods can be used to great advantage to assist in finding optimal control solutions. In the final section of this chapter we outline an efficient computational scheme to solve the low-thrust trajectory optimization problem.

3.1 Low-Thrust Trajectory Optimization

From a systems theory perspective, a spacecraft trajectory is defined as a mapping from some time interval $t \in [t_0, t_f] \subset \mathbb{R}$ into state space $\mathbf{X} \subset \mathbb{R}^n$. Choosing a control function $\mathbf{u} = \mathbf{u}(t) \subset \mathbf{U} \subset \mathbb{R}^m$ completely defines the magnitude and direction of the spacecraft thrust vector for a given propulsion system. The trajectory is then obtained by integrat-

ing the motion equations of the spacecraft, which are typically given by a set of first-order differential equations of the form $\dot{\mathbf{x}} = \mathbf{f}(\mathbf{x}, \mathbf{u}, t)$. For later reference we note that the equations of motion enter the optimal control problem as a set of dynamic constraints.

3.1.1 Trajectory optimization objectives

The optimality of spacecraft trajectories is measured with a *performance index* or *cost function* that considers a series of mission objectives identified during the mission design process. Typical mission objectives are:

- (1) Minimize transfer time for a given payload or propellant mass.
- (2) Minimize propellant mass for a given mission transfer time and launch mass.
- (3) Minimize propellant mass for a given mission transfer time and payload mass.

The performance index for a minimum-propellant transfer problem is formulated in “optimization” language as

$$\mathcal{J}_{m_p} = \int_{t_0}^{t_f} \dot{m}_p dt = m_p(t_f) - m_p(t_0) \quad (3.1)$$

where m_p is the propellant mass. For minimum-time problems the cost function can be written as

$$\mathcal{J}_T = \int_{t_0}^{t_f} dt = t_f - t_0 \equiv T \quad (3.2)$$

Since we are only concerned with minimum-time transfer problems we define the corresponding performance index as $\mathcal{J} \equiv \mathcal{J}_T$ and omit the subscript henceforth.

In practice, spacecraft trajectories have to be optimized with respect to several conflicting mission objectives, e.g. minimize transfer time and propellant mass. Such multi-objective optimization problems are usually reformulated as a series of single-objective problems. Various strategies for have been proposed in the literature; the most common ones are as follows:

- The primary mission objective is subject to optimization. Remaining objectives are redefined as mission constraints.
- All mission objectives are treated equivalently by defining weighting factors. The weighted objectives are combined into a single scalar quantity. The challenge is to identify a meaningful combination of weighting factors to reflect the scientific relationships of the mission objectives.

Both strategies provide only single solution trajectories that do not reflect the possible compromises between conflicting objectives. Hajela²⁸ discusses various methods to analyze multi-objective optimization problems. Another powerful approach to address multi-objective optimization problems is to resort to *Pareto-optimal* concepts.³⁶ Pareto-optimality describes “. . . the best that could be achieved without disadvantaging at least one . . .”, in our case, optimization objective.

3.1.2 Low-thrust versus high-thrust trajectory optimization

Trajectory optimization for spacecraft using high-thrust propulsion systems is mathematically relatively straightforward. Thrust phases for high-thrust missions are typically short compared to the overall mission time. As a result, thrust arcs are modelled as isolated, singular events, and the continuous optimal control problem can be reduced to a discrete optimization problem.^{4,18,72} A typical high-thrust optimal control problem is the extended version of *Lambert’s Problem*:³

Definition (Extended Lambert Problem). Let $\mathbf{r}_0 = \mathbf{r}(t_0)$ and $\mathbf{r}_f = \mathbf{r}(t_f)$ be the initial and final spacecraft position vectors, respectively. Find the transfer orbit that connects \mathbf{r}_0 and \mathbf{r}_f for a given transfer time $T = t_f - t_0$ and given initial and final spacecraft velocities and such that the velocity increment $\Delta v = \|\Delta \mathbf{v}_0\| + \|\Delta \mathbf{v}_f\|$ is minimized.

In the Extended Lambert Problem the unknown optimization parameters are the velocity increments \mathbf{v}_0 and \mathbf{v}_f corresponding to the infinitesimally short thrust arcs at $t = t_0$ and $t = t_f$. The performance index is therefore a function of six **numbers**, and the numerical difficulties involved in the optimization problem are moderate.

Unlike high-thrust systems, low-thrust propulsion systems operate for significant periods of the mission time; the corresponding trajectory optimization problem has to be modelled as a continuous system and the dimension of the solution space is infinite. Therefore, the low-thrust trajectory optimization problem is equivalent to the problem of finding the optimal control function $\mathbf{u}^* = \mathbf{u}^*(t)$ in an infinite-dimensional function space \mathbf{U} . The low-thrust optimal control problem is comparatively challenging in general and considered to be numerically difficult when required to be solved exactly.

One of the major issues of continuous low-thrust trajectory optimization problems lies in constructing a reasonably accurate reference trajectory to initiate the optimization

process. For discrete optimization problems such as the Extended Lambert Problem, on the other hand, one can typically come up with a rough estimate on the magnitude of the optimization parameters, for example, based on experience.

3.1.3 Mission scenarios

We analyze optimization algorithms from the perspective of the general minimum-time optimal control problem and with particular focus on time-optimal interplanetary transfers. Depending on specific mission objectives various solution families can be identified. Of particular interest are the intercept problem, the orbit transfer problem, and the rendezvous problem:

\mathcal{P}_0 **Intercept problem:** Minimum-time intercept with target object.

\mathcal{P}_1 **Orbit transfer problem:** Minimum-time transfer between an initial Keplerian and a target Keplerian orbit. There is no additional angular end-point constraint.

\mathcal{P}_2 **Double orbit transfer problem:** \mathcal{P}_1 transfer with subsequent \mathcal{P}_1 return transfer to initial orbit. There are no additional angular interior- and end-point constraints.

\mathcal{P}_3 **Rendezvous problem:** Minimum-time rendezvous with a target object. The angular end-point constraint depends on the initial angular separation between initial and target object, and the synodic period of the target object.

\mathcal{P}_4 **Double rendezvous problem:** Minimum-time transfer including a target object rendezvous and subsequent rendezvous with initial object.

Problem families \mathcal{P}_0 through \mathcal{P}_4 represent optimal control problems with increasing levels of complexity. While the intercept problem only involves a constraint on the final position of the spacecraft, for rendezvous problems both the final position and velocity of the spacecraft have to match final position and velocity of the target planet. Accordingly, additional midpoint constraints have to be satisfied for the double rendezvous problem.

3.2 Optimization Theory

Continuous trajectory optimization problems are traditionally solved via direct or indirect methods. A distinguishing feature of direct methods is that they are numerically more robust than indirect methods. The “quality” of the initial guess (closeness of initial guess from global minimum) is therefore not as crucial as for indirect methods, which is often

the decisive factor when opting for direct methods. Both optimization approaches require an initial set of optimization parameters – an *initial guess* – to initiate the optimization procedure. The generation of a proper initial set of optimization parameters is usually the most computationally expensive phase of an optimization algorithm.

In this section we briefly discuss optimization strategies based on direct and indirect methods. We then focus on designing an optimization algorithm that relies exclusively on indirect methods. To address the issue of initial guess generation we introduce a global search algorithm known in the literature as Adaptive Simulated Annealing.⁴⁰ In addition, we present advanced mathematical concepts such as symmetry and homotopy methods to assist in the solution finding process.

3.2.1 The optimal control problem

The optimal control problem is to find an optimal control input $\mathbf{u}^* \in \mathbf{U} \subset \mathbb{R}^m$ for a set of generally nonlinear, coupled differential equations of the form

$$\dot{\mathbf{x}} = \mathbf{f}(\mathbf{x}, \mathbf{u}, t), \quad t \in [t_0, t_f] \quad (3.3)$$

subject to boundary conditions

$$\Psi(\mathbf{x}(t_0), \mathbf{x}(t_f), t_0, t_f) = (\psi_0(\mathbf{x}(t_0), t_0), \psi_f(\mathbf{x}(t_f), t_f))^T = \mathbf{0} \quad (3.4)$$

and such that the associated cost function^{8,56}

$$\mathcal{J} = \phi(\mathbf{x}(t_f), t_f) + \int_{t_0}^{t_f} \mathcal{L}(\mathbf{x}, \mathbf{u}, t) dt \quad (3.5)$$

is minimized. In general, constraints on state and control variables have to be considered, as well. These constraints enter the optimal control analysis in the form of inequality and equality constraints

$$\sigma(\mathbf{x}, \mathbf{u}, t) \geq \mathbf{0} \quad (3.6)$$

For example, for spacecraft applications the maximum available thrust (or equivalently, the magnitude of the control input) presents a typical control variable constraint;^{22,24} that is, $0 \leq \|\mathbf{u}\| \leq u^{\max}$. Note that this two-sided control variable constraint has to be rewritten as two separate one-sided constraints to match the form of equation (3.6). For a detailed analysis on the implementation of state and control variable constraints we refer to Bryson and Ho⁸, Hartl et al.³³

3.2.2 Direct and indirect methods

Analytical solutions are available only for some special classical optimal control problems.^{8,19,78} In general, it is necessary to resort to numerical methods to obtain solutions to the optimization problem. In the literature these methods are classified into two categories: direct and indirect methods^{5,100}. As the names suggest, direct methods *directly* solve for the unknown control variables. With indirect methods the control variables are solved for *indirectly* via the associated Two-Point Boundary Value Problem.

Direct methods

In direct algorithms the optimal control problem is transformed into a nonlinear programming problem, which is solved either via a penalty function method or methods of augmented Lagrangian functions.

The basic idea behind direct approaches as realized in collocation methods is to introduce a discretization of the time interval $t \in [t_0, t_f]$. The control parameters of the nonlinear programming problem – the unknowns of the optimization problem – are the values of the state and control variables at the grid points. For collocation methods, piecewise linear interpolating functions between the grid points are chosen for the controls. The states are chosen to be continuously differentiable and piecewise cubic functions. More advanced discretization schemes use higher-order polynomial approximations and other finite sum expansions to improve accuracy of the solution trajectory. However, using more sophisticated discretization models also significantly increases numerical difficulties, especially in the presence of path constraints.⁵ For a more detailed discussion on the theory of direct methods we refer to Betts⁵.

The major advantage of direct methods lies in their numerical robustness; there is no equivalent to the numerically sensitive costate system as present in indirect methods. One of the drawbacks of direct methods, on the other hand, is that only approximate solutions are obtained. Increasing the number of control parameters yields, in general, an improvement in the accuracy of the solution. The increased number of unknowns, however, leads to a considerable increase in computational complexity and computation time. Another disadvantage of direct methods is the existence of multiple minima (also called pseudo-minima) as a result of the discretization process.⁵² Even though pseudo-minima satisfy all necessary conditions for the optimal solution, the corresponding parameter set may not be “close” to the parameter set of the actual minimum.

Indirect methods

Indirect methods are based on the calculus of variation⁸ and Pontryagin's minimum principle.^{8,74} The optimization problem is obtained via variation of an *augmented performance index* \mathcal{J}^+ that includes motion equations (constraints) and – when necessary – state and control variable constraints. The motion equation constraints are associated with the vector of costates $\boldsymbol{\lambda} \in \Lambda \subset \mathbb{R}^n$; the infinite-dimensional optimization problem is transformed into a \underline{n} -dimensional (and therefore discrete) optimization problem for the unknown costates. Note that for the unconstrained (with respect to path and control constraints) minimum-time problem $\underline{n} = n$.⁷

Assuming the absence of path and control variable constraints for the time being, the *Hamiltonian function* \mathcal{H} is obtained from the augmented performance index as

$$\mathcal{H} = \mathcal{L}(\mathbf{x}, \mathbf{u}, t) + \boldsymbol{\lambda}^\top \mathbf{f}(\mathbf{x}, \mathbf{u}, t) \quad (3.7)$$

Under certain smoothness conditions⁸ the following first-order necessary conditions for the state and control vectors are then obtained from the first variation of \mathcal{J}^+ . As demonstrated in Appendix A the conditions yield

$$\dot{\mathbf{x}} = \frac{\partial \mathcal{H}}{\partial \boldsymbol{\lambda}} = \mathbf{f}(\mathbf{x}, \mathbf{u}, t) \quad \text{and} \quad \dot{\boldsymbol{\lambda}} = -\frac{\partial \mathcal{H}}{\partial \mathbf{x}} = -\frac{\partial \mathcal{L}(\mathbf{x}, \mathbf{u}, t)}{\partial \mathbf{x}} - \frac{\partial \mathbf{f}(\mathbf{x}, \mathbf{u}, t)}{\partial \mathbf{x}} \boldsymbol{\lambda} \quad (3.8)$$

which represent a Boundary Value Problem (BVP). In general, the boundary conditions for the state variables are given; the boundary conditions for the costates, or more precisely, their initial $\boldsymbol{\lambda}(t_0)$ or final values $\boldsymbol{\lambda}(t_f)$ are the unknowns of the optimization problem. The optimal control law is determined by minimizing the Hamiltonian function with respect to the control vector; that is,

$$\frac{\partial \mathcal{H}}{\partial \mathbf{u}} = \mathbf{0} \quad \text{and} \quad \frac{\partial^2 \mathcal{H}}{\partial \mathbf{u}^2} > [0] \quad (3.9)$$

where $> [0]$ denotes positive definiteness of a matrix. The optimal control law \mathbf{u}^* can then be written as

$$\mathbf{u}^* = \arg \min_{\mathbf{u} \in \mathbf{U}} \mathcal{H}(\mathbf{x}^*, \boldsymbol{\lambda}^*, \mathbf{u}), \quad \forall t \geq 0 \quad (3.10)$$

There exists a wide variety of techniques to solve the general Boundary Value Problem. The most frequently used approach for trajectory optimization problems is based on the *multiple-shooting method*. Contrary to most other techniques, the multiple-shooting method has the distinct advantage that all kinds of constraint scenarios can be implemented conveniently and exact solutions to the optimal control problems can be obtained.

⁷ For dynamical systems with ignorable coordinates $\underline{n} < n$, in general.

Therefore, we decide to implement the shooting method in our optimization algorithm. As mentioned in the previous section, the system of costate equations (3.8) is extremely sensitive to variations in the initial conditions. Consequently, the successful application of indirect methods heavily depends on the availability of a “good” initial guess of the optimization parameters. Therefore, the first phase of every optimization algorithm, the generation of an acceptable set of optimization parameters,^{20,87} is typically the most work-intensive and mathematically complex stage of the optimization procedure. Another drawback of indirect methods is that the switching structure of the constraints has to be known a-priori. For a detailed review of solution techniques for constrained optimal control problems we refer to Betts⁵.

3.2.3 Optimization techniques

The ultimate success of optimization algorithms heavily depends on whether or not a reasonable accurate guess of the optimization parameters is available or can be generated during the optimization process. As a result, most approaches use a cascaded scheme including both global and local optimization tools. In general, global optimization techniques feature a large convergence radius with limited convergence rate and are used in the first phase of the optimization process. For low-thrust trajectory optimization problems the objective of the global optimizers is to identify a bounded region in the search space that encloses the global minimum. Once the approximate neighborhood of the global minimum is detected local optimization techniques are applied to compute the optimal parameter set with increased convergence rate.

We employ a global, stochastic search algorithm known as *Adaptive Simulated Annealing* and use deterministic approaches such as Quasi-Newton and Newton methods to perform the fine-tuning of the optimization parameters.

A stochastic approach: Adaptive Simulated Annealing

The difficulty of global optimization problems is to find the “best” optimum – the global optimum – from a multitude of local optima. For many practical optimization problems the application of deterministic search algorithms often proves inefficient or simply unfeasible. Simulated Annealing is a stochastic, global optimization scheme, initially designed for discrete – also known as *combinatorial* – optimization applications such as optimal chip placement, electronic circuit wiring, and logistic problems such as the *Traveling*

Salesman Problem.^{9,13,51,73}

Definition (Traveling Salesman Problem). Given the locations of N cities find the shortest closed “tour” to connect the cities passing through each city exactly once. The distance between every pair of cities i and j is $d_{i,j}$.⁸

The Simulated Annealing algorithm can then be applied in the following way:

- The solution space is represented by the set of all cyclic permutations π , that is, $\Pi = (\Pi(1), \Pi(2), \dots, \Pi(N))$, where $\Pi(i)$ denotes the successor city of city i in the tour represented by the set Π .
- The performance index is chosen as $\chi(\Pi) = \sum_{i=1}^n d_{i,\Pi(i)}$.
- New solutions are generated by choosing two arbitrary cities labeled k and l , and reversing the sequence in which the cities in between cities k and l are traversed.
- The difference in the performance index is calculated incrementally from the following expression: $\Delta\chi(\Pi) = -d_{k,\Pi(k)} - d_{\Pi^{-1}(l),l} + d_{k,\Pi^{-1}(l)} + d_{\Pi(k),l}$. $\Pi^{-1}(i)$ denotes the predecessor city of city i .

Characteristic for global optimization problems, the number of possible itineraries in the Traveling Salesman Problem is finite but prohibitively large. For example, for 15 cities the number of different tours that need to be examined to find the solution to the Traveling Salesman Problem already exceeds 10^{12} , which clearly reflects the global nature of the optimization problem.

The term simulated annealing (SA) derives from the analogous physical process of thermal annealing (metallurgy) to obtain a defect-free (and so in some sense optimized) crystalline structure. In an annealing process a melt, initially at high temperature and disordered, is cooled in a controlled, slow manner to keep the system in an approximate state of thermodynamic equilibrium (adiabatic cooling). As cooling proceeds, the system becomes ordered and approaches a ground state. In a SA optimization algorithm, the annealed substance corresponds to the system being optimized. Similarly, the current “energy” state of the substance corresponds to the current value of the system cost function, with the goal of identifying the ground state of the system, the global minimum. The internal microscopic interactions that keep the substance in a state of thermodynamical equilibrium are simulated in SA by a sequence of parameter perturbations described

⁸ The original version of the Traveling Salesman Problem assumes that the effort to travel between two cities is directly proportional to distance between them. Of course, the systems dynamics can be adapted ad libitum.

by Markov chains. One major difficulty of implementing a SA algorithm is that there is no obvious analog to the temperature in the physical process. The corresponding SA control parameter serves as a reference energy defining the boundary between the local and global vicinity of the current optimal parameter set in parameter space.

In general, stochastic optimization methods such as Simulated Annealing differ from deterministic techniques in that the iteration procedure need not converge towards a local optimum since transitions thereout are always possible. Another feature is that an adaptive exploration of the search space occurs: coarse features of the optimal parameter set appear at higher temperatures, fine details develop at lower temperatures. The method incorporates the three functional relationships

$P(\boldsymbol{\xi}_i)$ Probability density of parameter-space. $\boldsymbol{\xi}_i = (\xi_{i,1}, \dots, \xi_{i,l})^\top$ is the l -dimensional parameter vector at the i th iteration step.

$H(\Delta E_i)$ Probability for accepting a new performance index given the previous value thereof.

ϑ_i Annealing schedule for temperature ϑ_i at the i th annealing level.

The basic features of SA are illustrated in Figure 3.1: Starting from a randomly generated initial point – a first candidate – $\boldsymbol{\xi}_{i=i_0} \equiv \boldsymbol{\xi}_0$ in the parameter domain of interest and with an assigned initial temperature $\vartheta_{i=i_0}$ the algorithm identifies a new point $\boldsymbol{\xi}_{i+1}$, the best candidate of the $(i + 1)$ st sequence of trial points and evaluates the performance index, the “energy” of the system $E_{i+1} \equiv E(\boldsymbol{\xi}_{i+1})$. If the energy change between the two candidates and $\Delta E_i = E_i - E_{i+1}$ represents a decrease in the performance index, the new point is accepted right away. Otherwise, the new point is accepted with a probability $H(\Delta E_i) \propto \exp(\Delta E_i / \vartheta_i)$. The sequence of generated points with probabilistic acceptance is referred to in the literature as a *Markov chain*. After a sufficient number of trial points have been generated a new Markov chain is generated at a lower temperature level ϑ_{i+1} .

The cooling schedule ϑ_i critically affects the tendency of the algorithm to find the region enclosing the global minimum. Initially the temperature is chosen relatively high; most trial points are accepted and there is little chance of the algorithm converging towards a local minimum. As the temperature is decreased for later generations of Markov chains trial points accumulate more regionally and the search becomes localized. However, unlike for deterministic optimization techniques, with SA statistical temperature fluctuations can always cause uphill steps out of a local minimum. Another important aspect of the SA algorithm is trial point generation. Various approaches have been proposed, for example, using a uniform distribution on the domain of interest or a mix of a uniformly distributed draw and deterministic steps into a descent direction from the

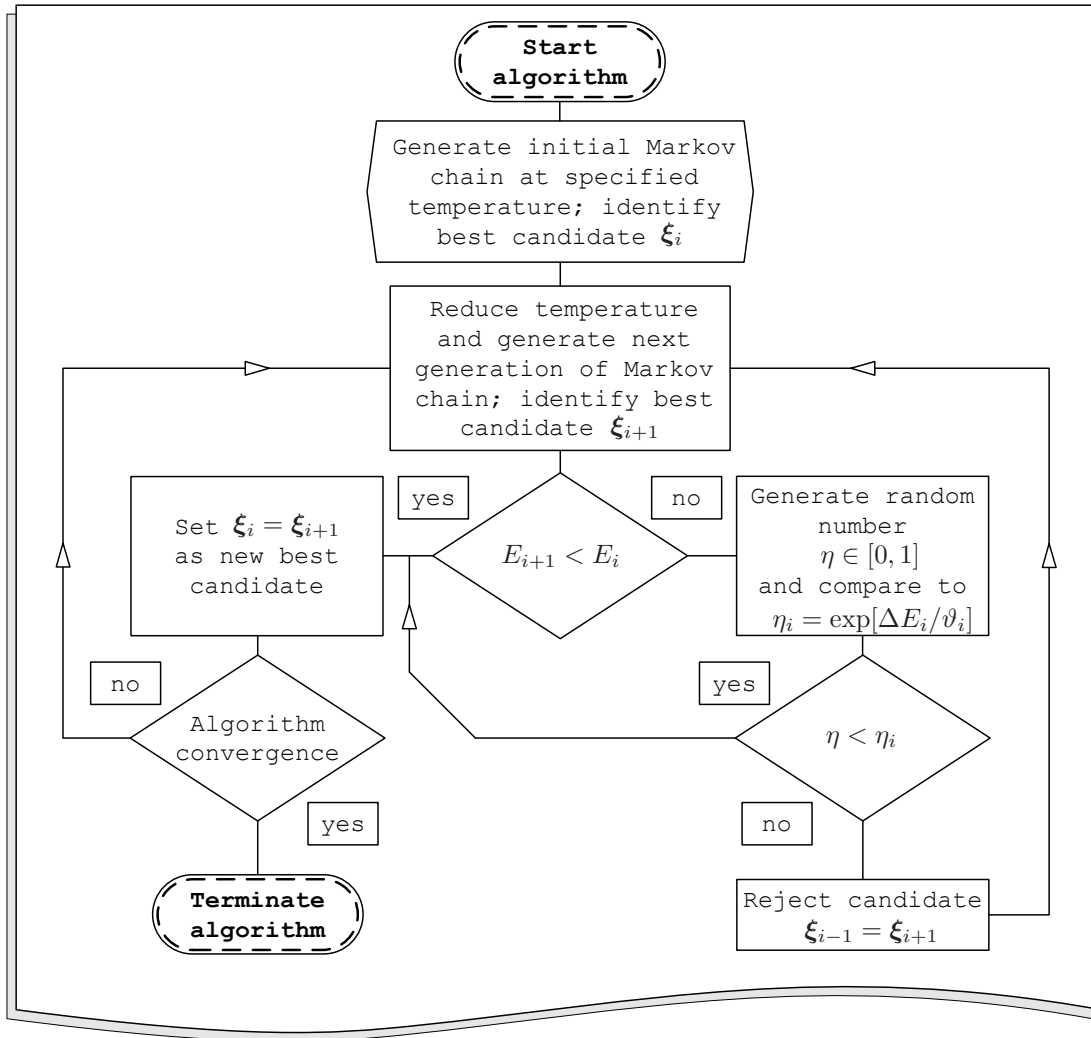


Figure 3.1: Flowchart of the Adaptive Simulated Annealing algorithm.

current point. One of the more popular ways to generate trial points is based on the *Metropolis acceptance probability*⁶⁴

$$A(\boldsymbol{\xi}_i, \vartheta_i) = \min \{1, \exp [-(\boldsymbol{\xi}_{+i} - \boldsymbol{\xi}_i)/\vartheta_i]\} \quad (3.11)$$

where $A(\boldsymbol{\xi}_i, \vartheta_i)$ is the probability of accepting a point $\boldsymbol{\xi}_{+i}$ if $\boldsymbol{\xi}_i$ is the current point and $\boldsymbol{\xi}_{+i}$ is generated as a possible new point.

Compared to other global search methods such as Genetic Algorithms, Simulated Annealing has been shown to provide superior performance variance with increased convergence rate.⁵⁸ Additionally, Genetic Algorithms are not designed to ergodically sample and cover

the parameter space in the most efficient manner and hence can not provide a complete system representation. The prime benefit of Genetic Algorithms, on the other hand, occurs when candidate evaluations can be performed in parallel, making Genetic Algorithms an excellent technique to run on parallel processing hardware. In comparison, the Simulated Annealing process is largely sequential in evaluating possible candidates.

Newton and Quasi-Newton methods

Common to all deterministic optimization methods is the strategy of *iterative improvement* requiring the cost function to decrease at every iteration step. Iterative improvement is achieved by taking steps into a descent directions of the performance index.

Optimization techniques based on iterative improvement such as Newton and Quasi-Newton methods typically follow a generic algorithm:

Algorithm UC (Unconstrained optimization)

- UC1** Test for convergence. If convergence conditions are satisfied, the algorithm terminates.
- UC2** Compute a search (descent) direction ζ_i .
- UC3** Compute a step length v_i that achieves a sufficient decrease in the cost function.
- UC4** Update current estimate of the minimum and proceed to step **UC1**; $i \rightarrow i + 1$.

In the following section we discuss the practical implementation of the outlined algorithm and specifics of Newton and Quasi-Newton methods with respect to low-thrust trajectory optimization.

To keep the analysis general, we denote the cost function of a general optimization problem by $\chi(\mathbf{p})$, and by $\chi(\mathbf{p}_i)$, when evaluated at a particular point \mathbf{p}_i . The gradient and Hessian of the cost function are denoted by $\mathbf{g}_i = \nabla\chi(\mathbf{p}_i)$ and $H_i = \nabla^2\chi(\mathbf{p}_i)$, respectively.

Step length computation To ensure the convergence of the optimization scheme the iterative steps into descent directions have to produce a sufficient decrease in the cost function. The sufficiency requirement can be satisfied choosing several conditions on the step length v_i . As an example, a sufficient decrease is achieved when the step size satisfies the Goldstein-Armijo principle:⁶⁷

$$v_{i,0} = \begin{cases} 1, & \text{if } \chi(\mathbf{p}_i - \zeta_i) \leq \chi(\mathbf{p}_i) - \mathbf{g}_i^\top \zeta_i \\ \bar{v}_i, & \text{else} \end{cases} \quad (3.12)$$

where

$$\bar{v}_i = \max \left\{ c_1, \min \left\{ c_2, \frac{\mathbf{g}_i^\top \boldsymbol{\zeta}_i}{2(\chi(\mathbf{p}_i - \boldsymbol{\zeta}_i) - \chi(\mathbf{p}_i) + \mathbf{g}_i^\top \boldsymbol{\zeta}_i)} \right\} \right\} \quad (3.13)$$

and with

$$v_i = v_{i,0} \rho_j \quad \text{max, such that} \quad \chi(\mathbf{p}_i - v_i \boldsymbol{\zeta}_i) - \chi(\mathbf{p}_i) \leq v_i \mathbf{g}_i^\top \boldsymbol{\zeta}_i \quad (3.14)$$

and where $0 < \rho_j < 1$. In equation (3.13) scalars c_1 and c_2 are chosen to satisfy $0 < c_1 \ll 1 \ll c_2$. In typical applications based on the Goldstein-Armijo principle, the trial values of v_i are defined in terms of an initial step length $v_{i,0}$ and the step reduction factor ρ_j . The value of v_i is then chosen as the first member of the sequence $\{v_{i,0} \rho_j\}$ as outlined in equation (3.14), for which equation (3.12) is satisfied for some c_1 and c_2 .

In our experience, the performance of the optimization algorithm, that is, its convergence range and rate, depends critically on the choice of the initial step length and parameters in equation (3.13). The usual convention to take $v_{i,0}$ as unity proves to be moderately successful. Conservative choices for c_1 and c_2 typically guaranteed convergence, however, usually with unacceptable low convergence rate. For overly optimistic values of c_i , the algorithm did not converge at all in most cases. In general, the successful choice of a set of step length parameters was based on an intuitive feeling developed during extensive testing of the overall optimization algorithm.

There is an obvious tradeoff between the effort expended to determine a “good” set of step length parameters and the resulting benefits of improving the cost function. Alternative conditions on step length computations are available in the literature; for example, the Powell-Wolfe principle.⁶⁷ However, we decide to compare the performance of the step length formula based on the Goldstein-Armijo principle to the performance of a relatively simplistic search method, the Golden Section search.⁶⁷

The Golden Section search is a line search technique based on interval reduction via bracketing and represents an elegant and robust approach. The algorithm is illustrated in Figure 3.2 and works as follows: Given a scalar, unimodal function $\chi(p)$ in one variable and defined over the normalized search interval $[p_0, p_1] \sim [0, 1] \equiv I$ identify the two intervals $I_l = [0, 1 - \varpi]$ and $I_u = [\varpi, 1]$ where $\varpi = 2/(1 + \sqrt{5}) \approx 0.618$ is the so-called *Golden ratio* and evaluate the cost function at $p_l = 1 - \varpi$ and $p_u = \varpi$. Depending on the relative values of $\chi(p_l)$ and $\chi(p_u)$ the minimum is located either in $I'_l = I \setminus [0, 1 - \varpi]$ or in $I'_u = I \setminus [\varpi, 1]$. The bracketing procedure is then repeated with the reduced interval $[0', 1']$ until conditions for convergence are satisfied.

With the Golden Section search, there is a linear reduction of the interval of uncertainty by the factor ϖ at every step. The difficulty of this method, of course, lies in determining

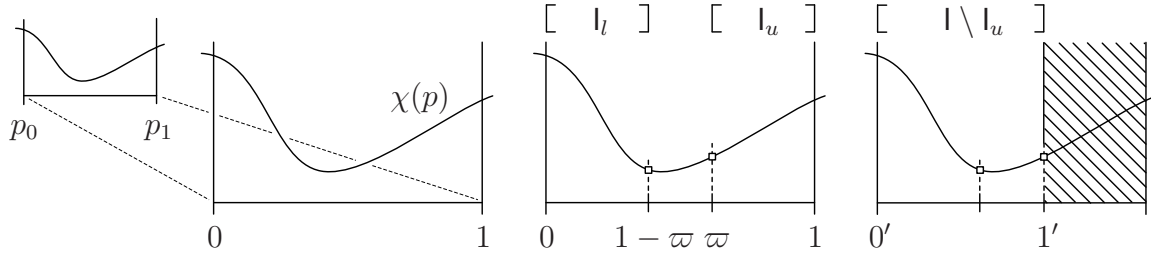


Figure 3.2: Interval reduction with Golden Section search algorithm.

the maximum range of the interval $[p_0, p_1]$ in which the $\chi(p)$ is unimodal. So in some sense, the challenge of finding the best step length with the previously discussed step length algorithms appears as a related problem with the Golden Section search method. The advantage of the Golden Section Search lies in its structural simplicity and the fact that no derivative information of the cost functions is required. If, however, such information is available it can be used to improve the convergence of the algorithm.⁶⁷

In comparison with the step length algorithm based on the Goldstein-Armijo principle, the Golden Section search proved to be surprisingly robust for trajectory optimization typically providing an acceptable convergence rate. In particular, for more complex optimization problems (e.g. minimum-time transfer for Solar Sail propulsion systems in three dimensions) the Golden Section search showed better convergence behavior.

Search direction computation Assuming that the cost function can be locally approximated by the first two terms of a Taylor series expansion

$$\chi(\mathbf{p}_i + \boldsymbol{\zeta}_i) = \chi(\mathbf{p}_i) + \mathbf{g}_i^\top \boldsymbol{\zeta}_i + \boldsymbol{\zeta}_i^\top H_i \boldsymbol{\zeta}_i + \mathcal{O}((\boldsymbol{\zeta}_i)^3) \approx \chi(\mathbf{p}_i) + \mathbf{g}_i^\top \boldsymbol{\zeta}_i \quad (3.15)$$

one way to obtain a sufficient decrease in $\chi(\mathbf{p})$ is to minimize a normalized⁹ expression of the second term in the expansion (3.15) $\mathbf{g}_i^\top \boldsymbol{\zeta}_i$. In other words, choose $\boldsymbol{\zeta}_i$ so that, amongst all suitably normalized vectors, $\mathbf{g}_i^\top \boldsymbol{\zeta}_i$ is a minimum. For a given p -norm $\|\cdot\|_p$, $\boldsymbol{\zeta}_i$ is therefore the solution of the minimization problem

$$\min_{\boldsymbol{\zeta} \in \mathbb{R}^n} \frac{\mathbf{g}_i^\top \boldsymbol{\zeta}}{\|\boldsymbol{\zeta}\|_p} \quad (3.16)$$

and the solution depends on the specific choice of p . For example, choosing the 2-Norm $\|\boldsymbol{\zeta}_i\|_2 = (\boldsymbol{\zeta}_i^\top \boldsymbol{\zeta}_i)^{1/2}$, it is straightforward to show that the solution is the negative

⁹ Normalization is necessary to eliminate the possibility of arbitrarily large step sizes, which would lead the first-order series expansion approximation of the cost function *ad absurdum*.

gradient, $\zeta_i = -\mathbf{g}_i$, which is known to be the *direction of the steepest descent*. Algorithms utilizing the steepest descent direction as the search direction are commonly referred to in the literature as *Steepest Descent* methods. Even though it is tempting to assume that Steepest Descent methods automatically yield rapid convergence we need to keep in mind that the analysis above is based on the assumption that the cost function can indeed be approximated by a first-order Taylor series expansion, which is usually not the case in practice. To improve the local model of the cost function, most optimization algorithms – such as Newton and Quasi-Newton methods – utilize second-order derivative information or an approximation thereof.

Newton’s method Newton’s method is the optimization algorithm par excellence and is therefore used as a standard to compare more complex optimization schemes against to. Newton’s methods are based on a quadratic model of $\chi(\mathbf{p})$ and therefore provide, at least locally, quadratic convergence. Expanding the cost function about the current point \mathbf{p}_i yields

$$\chi(\mathbf{p}_i + \zeta_i) \approx \chi(\mathbf{p}_i) + \mathbf{g}_i^\top \zeta_i + \zeta_i^\top H_i \zeta_i \quad (3.17)$$

The right-hand side of equation (3.17) is minimized by requiring that ζ_i is a minimum of the quadratic function

$$q(\zeta_i) = \mathbf{g}_i^\top \zeta_i + \zeta_i^\top H_i \zeta_i \quad (3.18)$$

Differentiating equation (3.18) with respect to ζ_i , a stationary point of satisfies

$$\zeta_i^\top H_i \zeta_i = -\mathbf{g}_i^\top \zeta_i \quad (3.19)$$

and the associated solution for ζ_i is termed Newton direction. Note that for $H_i > 0$, only a single iteration is required to reach the minimum of the model function in equation (3.17) from any starting point. Therefore, Newton’s method provides good convergence characteristics when the quadratic model is an accurate representation of $\chi(\mathbf{p})$, which requires \mathbf{p}_i to be sufficiently close to the minimum for most general nonlinear cost functions $\chi(\mathbf{p})$.

For the trajectory optimization problem Newton’s method proved to be a valuable part of the overall optimization algorithm. Especially for planar minimum-time transfers Newton’s method showed rapid convergence for an acceptable convergence range. Convergence characteristics degraded, however, noticeably for the more complex three-dimensional optimization problems. In particular, for the minimum-time transfer problem using solar sail propulsion the convergence rate dropped in most case into sub-linear range. Poor convergence characteristics, or, the unavailability of a sufficiently accurate starting point to employ Newton’s method require a more “tolerant” optimization scheme, e.g. Quasi-Newton methods.

Quasi-Newton methods Compared to Newton's method, Quasi-Newton methods belong to the category of pseudo first-order techniques that use second-order information via approximated function Hessian. Rather than computing the exact Hessian at every iteration step, Quasi-Newton methods are based on the idea of building up curvature information as the iterations proceed by using the observed behavior of the cost function and its first derivative.

The curvature of $\chi(\mathbf{p})$ along a specified direction $\mathbf{s}_i \equiv v_i \zeta_i = \mathbf{p}_{i+1} - \mathbf{p}_i$ is given by the second term in a Taylor series expansion $\mathbf{s}_i^\top H_i \mathbf{s}_i$ and can be approximated using first-order information

$$\mathbf{s}_i^\top H_i \mathbf{s}_i \approx (\nabla \chi(\mathbf{p}_i + \mathbf{s}_i) - \nabla \chi(\mathbf{p}_i))^\top \mathbf{s}_i \quad (3.20)$$

At the beginning of the i th iteration step of a Quasi-Newton method, an approximate Hessian matrix \mathbb{H}_i is calculated that contains the curvature information already accumulated. Typically, the initial Hessian approximation \mathbb{H}_0 is taken as the identity matrix if no additional information is available *a priori*. After \mathbf{p}_{i+1} has been computed, the Hessian is updated to take account of the current curvature information. The Hessian is updated according to the update formula

$$\mathbb{H}_{i+1} = \mathbb{H}_i + \mathbb{U}_i \quad (3.21)$$

where \mathbb{U}_i is termed the update matrix. The conditions required of an approximated Hessian are that it should approximate the curvature of the cost function along the step direction and – ideally – converge towards the true Hessian as the iteration process proceeds. Denoting by $\mathbf{y}_i = \mathbf{g}_{i+1} - \mathbf{g}_i$ the change in gradient and based on equation (3.20), the approximated Hessian is therefore required to satisfy the following conditions

$$\mathbb{H}_{i+1} \mathbf{s}_i = \mathbf{y}_i, \quad \text{and} \quad \mathbb{H}_i \text{ symmetric} \quad (3.22)$$

Since the (true) Hessian matrix is symmetric by construction, it seems reasonable to require symmetry for the approximated Hessian, as well.

Various update formulas have been suggested in the literature.⁶⁷ The so-called *symmetric rank-one update* has the form

$$\mathbb{H}_{i+1} = \mathbb{H}_i + \frac{1}{(\mathbf{y}_i - \mathbb{H}_i \mathbf{s}_i)^\top \mathbf{s}_i} (\mathbf{y}_i - \mathbb{H}_i \mathbf{s}_i)(\mathbf{y}_i - \mathbb{H}_i \mathbf{s}_i)^\top \quad (3.23)$$

The corresponding symmetric rank-two update formula – better known as the *Davidon-Fletcher-Powell (DFP) update* formula – can be written as

$$\mathbb{H}_{i+1} = \mathbb{H}_i - \frac{1}{\mathbf{s}_i^\top \mathbb{H}_i \mathbf{s}_i} \mathbb{H}_i \mathbf{s}_i \mathbf{s}_i^\top \mathbb{H}_i + \frac{1}{\mathbf{y}_i^\top \mathbf{s}_i} \mathbf{y}_i \mathbf{y}_i^\top + (\mathbf{s}_i^\top \mathbb{H}_i \mathbf{s}_i) \mathbf{w}_i \mathbf{w}_i^\top \quad (3.24)$$

where

$$\mathbf{w}_i = \frac{1}{\mathbf{y}_i^\top \mathbf{s}_i} \mathbf{y}_i - \frac{1}{\mathbf{s}_i^\top \mathbb{H}_i \mathbf{s}_i} \mathbb{H}_i \mathbf{s}_i \quad (3.25)$$

Extensive research has been performed in order to identify a “best” update strategy for the Hessian. The so-called *Broyden-Fletcher-Goldfarb-Shanno (BFGS) update* given by

$$\mathbb{H}_{i+1} = \mathbb{H}_i - \frac{1}{\mathbf{s}_i^\top \mathbb{H}_i \mathbf{s}_i} \mathbb{H}_i \mathbf{s}_i \mathbf{s}_i^\top \mathbb{H}_i + \frac{1}{\mathbf{y}_i^\top \mathbf{s}_i} \mathbf{y}_i \mathbf{y}_i^\top \quad (3.26)$$

is currently believed to produce Hessian information most efficiently⁶⁷ for a wide variety of practical applications.

Note that in order to obtain the search direction ζ_i it is necessary to solve the left-hand side equation (3.22) which involves $\mathcal{O}(n^3)$ operations. Using instead the inverse Hessian $\mathbb{H}_i = \mathbb{H}_i^{-1}$ to obtain the search direction reduces required operations to an order of $\mathcal{O}(n^2)$. This order-reduction significantly decreases computation time for complex systems of equations; calculation of the inverse Hessian is therefore the preferred approach to obtain the search direction.⁶⁷

The *inverse symmetric rank-one update* has the form

$$\mathbb{H}_{i+1} = \mathbb{H}_i + \frac{1}{(\mathbf{s}_i - \mathbb{H}_i \mathbf{y}_i)^\top \mathbf{y}_i} (\mathbf{s}_i - \mathbb{H}_i \mathbf{y}_i)(\mathbf{s}_i - \mathbb{H}_i \mathbf{y}_i)^\top \quad (3.27)$$

The inverse updated formula corresponding to the *Davidon-Fletcher-Powell update* can be written as

$$\mathbb{H}_{i+1} = \mathbb{H}_i - \frac{1}{\mathbf{y}_i^\top \mathbb{H}_i \mathbf{y}_i} \mathbb{H}_i \mathbf{y}_i \mathbf{y}_i^\top \mathbb{H}_i + \frac{1}{\mathbf{y}_i^\top \mathbf{s}_i} \mathbf{s}_i \mathbf{s}_i^\top \quad (3.28)$$

Finally, the *inverse Broyden-Fletcher-Goldfarb-Shanno (IBFGS) update* is given by

$$\mathbb{H}_{i+1} = \left(\mathbf{1} - \frac{1}{\mathbf{y}_i^\top \mathbf{s}_i} \mathbf{s}_i \mathbf{y}_i^\top \right) \mathbb{H}_i \left(\mathbf{1} - \frac{1}{\mathbf{y}_i^\top \mathbf{s}_i} \mathbf{y}_i \mathbf{s}_i^\top \right) + \frac{1}{\mathbf{y}_i^\top \mathbf{s}_i} \mathbf{s}_i \mathbf{s}_i^\top \quad (3.29)$$

where $\mathbf{1}$ is the n -dimensional unity matrix.

Comparing the performance of the various update formulas for the Hessian and its inverse, the BFGS and its corresponding inverse update formula slightly outperform the DFP and the rank-one updates. Provided good initial information on the Hessian matrix or its inverse are available, performance differences are subtle for most cases. However, when using the unity matrix to initiate the optimization procedure the BFGS update formula shows advantageous behavior in terms of converge rate compared to other update formulas. Performance differences between the regular and the inverse version of the update formula are noticeable especially from the perspective of computation time. Therefore, for our analysis we use the IBFGS update formula to compute search directions for the Quasi-Newton method.

3.2.4 Additional methods to solve MPBVP

We have discussed to this point conventional, numerical methods necessary to solve the Two-Point Boundary Value Problem. Even though being an essential element of the overall optimization algorithm, the application of these techniques is computationally expensive and therefore to be reduced to a minimum. The exploration of alternative, analytical methods is in order.

Symmetry methods

The Norwegian mathematician Sophus Lie put forward many of the fundamental ideas behind symmetry methods and pioneered the study of *Lie transformation groups* that leave systems of differential equations invariant.^{7,70,88} For ordinary differential equations, Lie's infinitesimal transformation method provides a widely applicable technique to find closed form similarity solutions. In addition, symmetries of differential equations often provide insight into the physical nature of the system.

In general, a symmetry group of a system of differential equations is a group that transforms solutions of the system to other solutions. Consider a system of differential equations

$$\Delta_i(\boldsymbol{\xi}, \boldsymbol{\mu}^{(k)}) = \mathbf{0}, \quad i = 1, 2, \dots, m \quad (3.30)$$

of order k , with p independent variables $\boldsymbol{\xi} = (\xi_1, \xi_2, \dots, \xi_p) \in \mathbb{R}^p$, and q dependent variables $\boldsymbol{\mu} = (\mu^1, \mu^2, \dots, \mu^q) \in \mathbb{R}^q$. Given a solution trajectory $(\boldsymbol{\mu}(\boldsymbol{\xi}), \boldsymbol{\xi})$ that satisfies equations (3.30) and given a symmetry transformation $g \in G$ in the Lie group G of differential equations (3.30) the transformed solution trajectory $(\hat{\boldsymbol{\mu}}(\hat{\boldsymbol{\xi}}), \hat{\boldsymbol{\xi}})$ given by

$$g \cdot \Gamma_{\boldsymbol{\mu}} = \left\{ (\hat{\boldsymbol{\xi}}, \hat{\boldsymbol{\mu}}) = g \cdot (\boldsymbol{\xi}, \boldsymbol{\mu}) : (\boldsymbol{\xi}, \boldsymbol{\mu}) \in \Gamma_{\boldsymbol{\mu}} \right\} \quad (3.31)$$

satisfies equations (3.30), as well.

In the framework provided by Lie these groups consist of geometric transformations on the space of both dependent and independent variables for the system. Frequently encountered examples of group transformations are translation, rotation, and scaling. Lie's most profound finding was that the generally complex and nonlinear conditions of invariance of the system under group transformation can be replaced by equivalent, linear – and therefore local – conditions reflecting the corresponding form of infinitesimal invariance of the system under the action of the infinitesimal generators of the group.

There are three major methods to compute Lie symmetries, respectively, their corresponding infinitesimal generators. The first and most widely used method is implemented in numerous symbolic software packages and uses so-called *prolonged vector fields*⁷, the second approach uses *Cartan's exterior calculus*.⁷ The application of these methods involves tedious and unwieldy computations that require a great amount of experience and a high level of mathematical proficiency. The third method applies the principle of *invariance under transformation* directly to the set of differential equations and relies on the more intuitive, engineering-type expertise. Especially for more complex, highly non-linear and coupled systems the third approach is often the preferred choice.

The steps of the prolongation method are described in detail in Olver⁷⁰ and can be summarized as follows:

For a system of differential equations (3.30) the partial derivatives of μ^l are represented as

$$\mu_J^l = \frac{\partial^{|J|} \mu^l}{\partial \xi_1^{j_1} \partial \xi_2^{j_2} \dots \partial \xi_p^{j_p}} \quad (3.32)$$

where for $J = (j_1, j_2, \dots, j_p) \in \mathbb{N}^p$, $|J| = \sum_{i=1}^p j_i$, and $\mu^{(k)}$ denotes the vector whose components are the partial derivatives up to order k of all μ^l .

One-parameter group transformations are parameterized by a parameter ϵ and have the form $\hat{\xi} = \Lambda_G(\xi, \mu; \epsilon)$, $\hat{\mu} = \Omega_G(\xi, \mu; \epsilon)$ where the transformations Λ_G and Ω_G are to be determined. Lie showed that the one-parameter Lie group G can be recovered from the knowledge of the linear terms in the Taylor series expansion of Λ_G and Ω_G , that is,

$$\hat{\xi}(\epsilon) = \hat{\xi}(\epsilon)|_{\epsilon=0} + \epsilon \left. \frac{\partial \Lambda_G(\xi, \mu; \epsilon)}{\partial \epsilon} \right|_{\epsilon=0} + \mathcal{O}(\epsilon^2) = \xi + \epsilon \eta(\xi, \mu) + \mathcal{O}(\epsilon^2) \quad (3.33)$$

$$\hat{\mu}(\epsilon) = \hat{\mu}(\epsilon)|_{\epsilon=0} + \epsilon \left. \frac{\partial \Omega_G(\xi, \mu; \epsilon)}{\partial \epsilon} \right|_{\epsilon=0} + \mathcal{O}(\epsilon^2) = \mu + \epsilon \varphi(\xi, \mu) + \mathcal{O}(\epsilon^2) \quad (3.34)$$

where $\hat{\xi}(\epsilon = 0) = \xi$ and $\hat{\mu}(\epsilon = 0) = \mu$. Therefore, instead of using the Lie group G directly, in the method of prolonged vector fields one uses the associated *Lie algebra* as defined by the corresponding vector fields

$$\Phi = \sum_{i=1}^p \eta^i(\xi, \mu) \frac{\partial}{\partial \xi_i} + \sum_{l=1}^q \varphi_l(\xi, \mu) \frac{\partial}{\partial \mu^l} \quad (3.35)$$

To obtain the determining equations for coefficients $\eta^i(\xi, \mu)$ and $\varphi_l(\xi, \mu)$ the k th prolongation $\text{pr}^{(k)}\Phi$ is constructed and applied to the system of differential equations (3.30). The result is a system of linear homogeneous partial differential equations – termed

the *determining system for the symmetries* – for η^i and φ_l , in which $\boldsymbol{\xi}$ and $\boldsymbol{\mu}$ are treated equally, and as independent variables. Solution of the system then yields the explicit forms of $\eta^i(\boldsymbol{\xi}, \boldsymbol{u})$ and $\varphi_l(\boldsymbol{\xi}, \boldsymbol{u})$. For a more detailed discussion on the method of prolonged vector fields we refer to Olver⁷⁰.

We have used the method of prolonged vector fields to solve for symmetry groups of several basic differential equations such as the *Heat Equation*, the *Wave Equation*, and the *Korteweg-de Vries Equation*. In trying to identify symmetries for our Two-Point Boundary Value Problems we encountered considerable difficulties on various levels. First, as compared with Initial Value Problems (and ordinary differential equations without any boundary conditions, for that matter) the existence of two sets of boundary conditions in Two-Point Boundary Value Problems severely restricts the number of possible symmetry groups. Secondly and more importantly, the complexity (nonlinearity, coupling) of the motion equations used for our analysis resulted in highly complex systems of determining equations. Solving the determining equations proved to be highly non-trivial and out of the scope of this dissertation. Just for comparison, to our best knowledge the classical Kepler problem is to date the most “complex” system that has been successfully analyzed to its entirety with respect to symmetry properties.^{55,68}

For these reasons we decide to approach the problem of finding symmetry groups by working directly with the differential equations and boundary conditions.

Continuation methods

The method of continuation is a method that augments the capabilities of conventional numerical techniques for solving sensitive Two-Point Boundary Value Problems by softening the requirements on the quality of the initial guess. Continuation methods imbed a problem in the family of neighboring Two-Point Boundary Value Problems which depend continuously on the so-called *continuation parameter* σ that can be varied smoothly in a predefined interval, typically $\sigma \in [\sigma_0, \sigma_N] = [0, 1]$ is chosen. The problem family is built in such a way that for $\sigma = \sigma_0$ the family degenerates to a problem with an available solution or a relatively easily obtainable solution. For $\sigma = \sigma_N$ reduces to the problem whose solution is desired. In general, continuation methods decrease the condition number of the problem at hand and guarantee good convergence provided no bifurcation or turning points are present in the problem.¹

In general, a homotopy function for a continuation method is defined as a mapping

$$\mathfrak{h} : \mathbb{R}^n \times \mathbb{R} \rightarrow \mathbb{R}^n \quad (3.36)$$

describing a parameter dependent family of problems $\mathfrak{h}(\mathbf{p}, \sigma) = 0$

$$\mathfrak{h}(\mathbf{p}, \sigma) \triangleq \mathfrak{f}(\mathbf{p}) - (1 - \sigma)\mathfrak{f}(\mathbf{p}_0) = 0 \quad (3.37)$$

for a given problem $\mathfrak{f}(\mathbf{p})$ and a given value \mathbf{p}_0 . By construction the problem family contains two limiting problems: on one hand, for $\sigma = 0$

$$\mathfrak{h}(\mathbf{p}, 0) = \mathfrak{f}(\mathbf{p}) - \mathfrak{f}(\mathbf{p}_0) = 0 \quad (3.38)$$

which represents a system of equations with $\mathbf{p} \equiv \mathbf{p}_0$ as the trivially known solution. On the other hand, setting $\sigma = \sigma_N = 1$ equation (3.36) simplifies to

$$\mathfrak{h}(\mathbf{p}, 1) = \mathfrak{f}(\mathbf{p}) = 0 \quad (3.39)$$

which is the problem whose solution is desired. The idea of continuation methods is to choose an “appropriate” partition of the interval $[\sigma_0, \sigma_N] \rightarrow \{\sigma_0, \sigma_1, \dots, \sigma_N\}$ and to iteratively solve a sequence of problems

$$\mathfrak{h}(\mathbf{p}, \sigma_i) = 0, \quad i = 1, 2, \dots, N \quad (3.40)$$

The key point of this approach is that if parameter step sizes $\Delta\sigma_i = \sigma_i - \sigma_{i-1}$ are sufficiently small, the solution \mathbf{p}_{i-1} of the $(i-1)$ st problem can be chosen as the initial guess for the subsequent problem and the iteration procedures converges. Using for example a Quasi-Newton or Newton method an “appropriate” partitioning of the parameter interval guarantees convergence while providing a rapid convergence rate.

We have applied continuation methods extensively to compute entire families of minimum-time trajectories by varying boundary conditions for a particular system model (that is to say, propulsion system). We refer to the problem of calculating solution trajectories for varying boundary conditions as *numeric continuation*. As illustrated in Figure 3.3 starting with an optimal (solid trajectory) for initial and final conditions IC and FC, we obtain another transfer solution (dashed trajectory) by slightly varying the final conditions $\text{FC} \rightarrow \text{FC}'$. Similarly, we have used continuation methods successfully to generate trajectories from the corresponding trajectory of a different system model while keeping the boundary conditions unchanged. For example, the problem of calculating minimum-time trajectories in three dimensions for solar sail spacecraft presents serious numerical difficulties. However, with the availability of an “analogous” solution trajectory for a nuclear-electric propulsion system these difficulties can be addressed appropriately using continuation methods. Figure 3.3 illustrates the process we refer to as *algebraic continuation*.

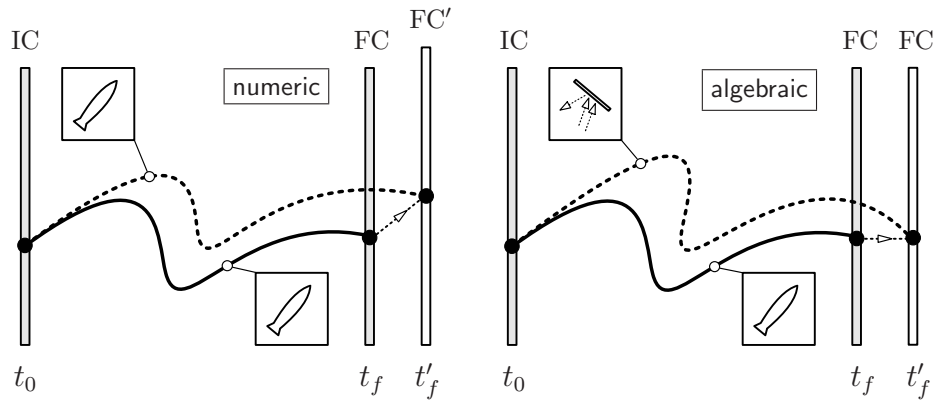


Figure 3.3: Numeric and algebraic continuation.

3.3 Developing an Optimization Algorithm

We have devised a cascaded computational scheme based on numerical and analytical methods. Whereas other conventional optimization packages rely on numerical solution approaches, we employ analytical and semi-analytical techniques such as symmetry and homotopy methods to assist in the solution-finding process. Figure 3.4 illustrates the basic concept of the optimization algorithm: The first objective is to obtain a single optimized trajectory that satisfies some given boundary conditions. The initialization phase for this first trajectory includes a global, stochastic search based on Adaptive Simulated Annealing. ASA provides a large convergence radius but only limited convergence rate and accuracy as indicated by the stars in the rating table on the left-hand side of Figure 3.4. The fine tuning of optimization parameters – the local search – is accomplished by Quasi-Newton and Newton methods. Both Newton and Quasi-Newton methods feature an increased convergence rate and accuracy when compared to the stochastic optimization method. Once an optimized trajectory has been obtained, we use system symmetry and continuation methods to generate additional optimal control solutions efficiently.

3.4 Summary

In this chapter we have discussed stochastic and deterministic optimization methods implemented in our algorithm. The innovation of our approach is the usage of homotopy and symmetry methods which allow for efficient computation of optimal control solutions.

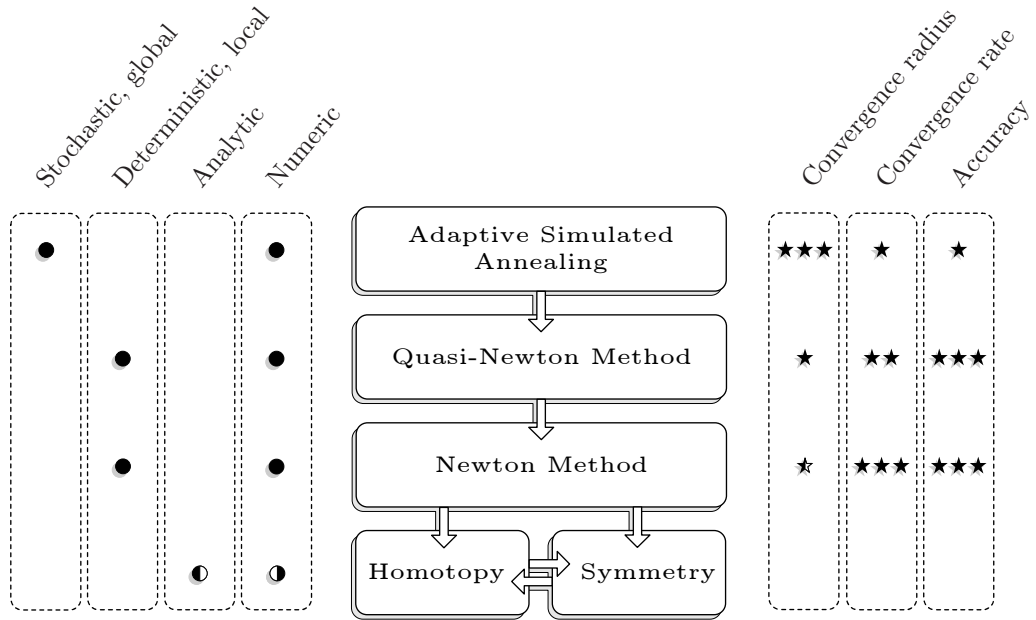


Figure 3.4: Cascaded numerical algorithm for solving the optimal control problem.

In the following chapter we introduce spacecraft system models and corresponding motion equations. The resulting optimal control problems are then solved in Chapter 5.

System Models and Motion Equations

In this chapter we introduce system models for solar-electric, nuclear-electric, and solar sail spacecraft and discuss corresponding motion equations. We analyze spacecraft system models for two- and three-dimensional analyses in Section 4.1 and derive the corresponding equations of motion for electric spacecraft in Section 4.2 and for solar sail spacecraft in Section 4.3.

4.1 System Models

Figure 4.1 and Figure 4.2 illustrate two- and three-dimensional system descriptions. We employ an unperturbed two-body system model of Sun and spacecraft neglecting the presence of other celestial bodies and other perturbation effects. The Sun is modeled as a point mass with spherically symmetric gravitation and solar radiation fields. Solar sail spacecraft are modelled as perfectly flat and perfectly reflective sails of mass m and surface area A and are treated dynamically as point masses. Spacecraft with nuclear- or solar-electric propulsion systems are modeled as point masses with variable mass $m(t)$. Solar flux \mathcal{S} and available solar power p_γ are functions of the distance r of the spacecraft from the Sun. Hence, for solar sail and solar-electric spacecraft the thrust $T(r)$ is also a function of r , whereas for nuclear electric spacecraft the thrust is assumed constant.

The equations of motion for all spacecraft system models are described with respect

to an inertial reference frame \mathcal{E} , which is defined by a set of mutually perpendicular vectors $\{\mathbf{e}_x, \mathbf{e}_y, \mathbf{e}_z\}$ with \mathbf{e}_x pointing in the vernal equinox direction Υ . We employ several different coordinate descriptions depending on the respective application. For two-dimensional analysis we use polar coordinates with $\mathbf{r} = (r, \theta)^\top$; cartesian $\mathbf{r} = (x, y, z)^\top$ and spherical $\mathbf{r} = (r, \theta, \phi)^\top$ coordinates are used for three-dimensional system models.

The control variables of the system – the unknowns of the optimization problem – are the thrust angles (e.g. $\boldsymbol{\alpha} = (\alpha_r, \alpha_{\phi\theta})^\top$) as measured with respect to an orbital reference frame, e.g. $\mathcal{O} = \{\mathbf{o}_r, \mathbf{o}_\theta, \mathbf{o}_\phi\}$. We use the following notation to unambiguously identify a set of control variables: Control angles with a single subscript are measured with respect to the axis of the corresponding orbital reference frame, for example, α_r is the angle between the control angles vector and the radial direction \mathbf{o}_r . Control variables with two subscripts are measured in the plane that corresponds to the two subscripts; the first subscript identifies the axis of the orbital frame from which the angle is measured. As an example, $\alpha_{\phi\theta}$ is the angle in the $\mathbf{o}_\phi\mathbf{o}_\theta$ -plane and measured with respect to the \mathbf{o}_ϕ -axis.

For the two-dimensional analysis initial and target spacecraft trajectories are modelled as heliocentric, circular, and coplanar orbits. Periodic Keplerian orbits are used to model planetary trajectories for the three-dimensional transfer problem. Trade studies exploring the physical behavior of optimal spacecraft transfers are more readily facilitated in two dimensions. In addition, usage of circular, coplanar planetary orbits minimizes the number of key system parameters. Most importantly, we show in Chapter 5 that the two-dimensional analysis accurately predicts the overall system behavior when compared to the three-dimensional analysis.

4.2 Electric Propulsion Spacecraft

In this section we briefly discuss electric spacecraft systems using nuclear-electric and solar-electric propulsion technologies. Compared to solar-electric spacecraft, nuclear-electric systems offer, in general, superior performance characteristics. Especially for missions into the outer regions of the solar system the solar flux decrease severely constraints the available electrical power and in turn the range of applications of solar-electric systems. On the other hand, nuclear-electric propulsion concepts come encumbered with public safety concerns as well as significant potential technical problems as discussed in a paper by Cameron and Herbert¹¹. As a consequence of the (public) lack in confidence in this highly controversial technology, development of nuclear spacecraft systems has suffered significant setbacks.

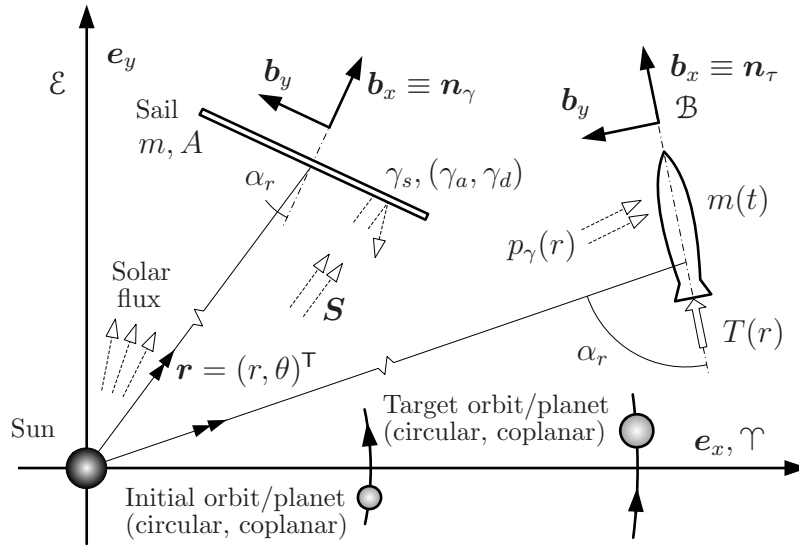


Figure 4.1: Dynamical systems representations in two dimensions.

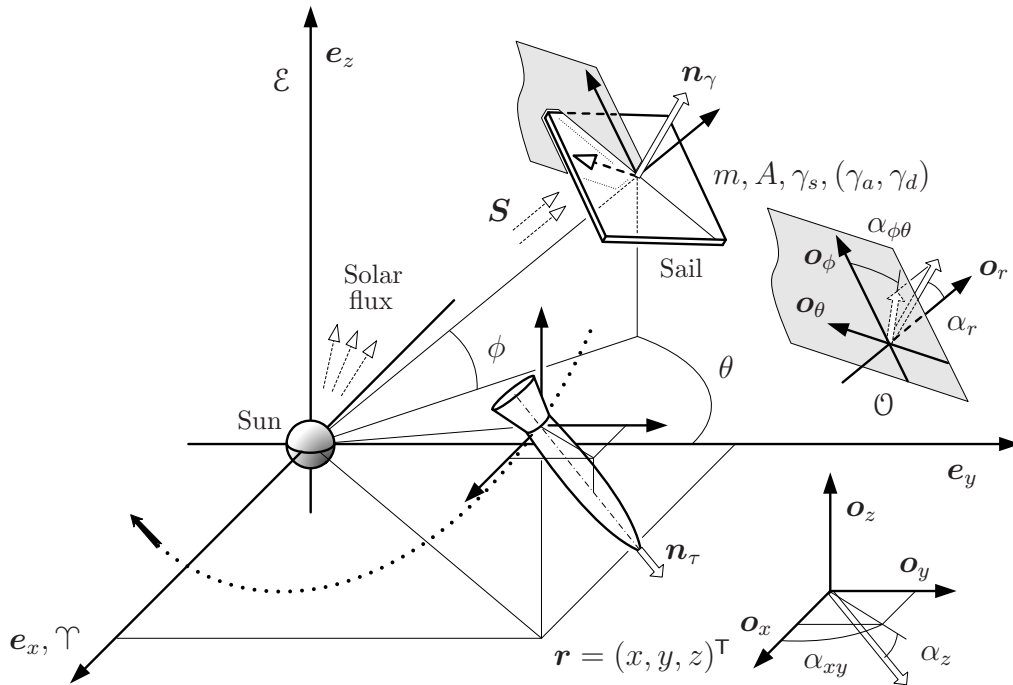


Figure 4.2: Dynamical systems representations in three dimensions.

4.2.1 Nuclear-electric propulsion systems

For nuclear-electric propulsion systems we assume a constant specific impulse I_{sp} and a constant thrust $T(r) = T$. With these assumptions the mass flow function $\mu(r)$ and the specific thrust $\tau(r)$ are given by³⁹

$$\mu(r) = \mu = -\frac{\tau m}{g_0 I_{sp}} = -c = \text{const.}, \quad \text{where} \quad \tau(r) = \frac{T}{m} \quad (4.1)$$

and where $c > 0$ is the mass flow rate and g_0 is the gravitational acceleration at the surface of the Earth.

4.2.2 Solar-electric propulsion systems

The model for solar-electric propulsion system is significantly more complex. First of all, the available electrical power is a function of the distance of the spacecraft from the Sun. Neglecting power fluctuations due to the spacecraft rotational motion the solar radiation flux decreases $\sim 1/r^2$ provided $r^{\min} < r < r^{\max}$. At some cutoff distance $r = r^{\max}$ all available electrical power is required to maintain operations of vital spacecraft systems (e.g. navigation, communication, etc.) of the spacecraft. As a result, power requirements are not met to reliably operate the propulsion system beyond the cutoff point. For decreasing values of r the available electrical power reaches a saturation level at some $r = r^{\min}$ which is defined by the standard of technology of the power system (efficiency and degradation of solar cells, efficiency of power conversion and storage units, etc.).

To reduce analysis complexity we assume that $r^{\min} = 0$ and $r^{\max} \rightarrow \infty$ and employ a simplified system model used in Circi¹⁵ and proposed by Williams and Coverstone-Carroll¹⁰²:

$$\tau(r) = [b_1 + b_2 P(r)]/m, \quad \mu(r) = c_1 + c_2 P(r), \quad [\tau(r)] = \text{mN}, \quad [\mu(r)] = \text{mg/s} \quad (4.2)$$

where the solar array performance, $P(r)$, is modelled as a polynomial of the form¹⁰²

$$P(r) = P_0 \frac{a_1 r^2 + a_2 r + a_3}{r^4 (1 + a_4 r)}, \quad [P(r)] = \text{kW}, \quad [r] = \text{AU} \quad (4.3)$$

In equation (4.3) P_0 is the reference power at 1 AU, the power is measured in kilowatts and the radial distance is measured in AU. Constants a_i , b_i , and c_i in equations (4.2,4.3) are parameters describing propulsion system characteristics and are given in Table 4.1.

Table 4.1: Solar-electric propulsion system performance parameters.¹⁰²

| Parameter | $i = 1$ | 2 | 3 | 4 |
|-----------|---------|---------|---------|---------|
| a_i | 1.1063 | 0.1495 | -0.2990 | -0.0423 |
| b_i | -1.9137 | 36.2429 | | |
| c_i | -0.4756 | -0.9021 | | |

For comparison we restate the propulsion system models for nuclear-electric and solar-electric spacecraft

Nuclear-electric propulsion

$$\tau(r) = T/m$$

$$\mu(r) = -c$$

Solar-electric propulsion

$$\tau(r) = [b_1 + b_2 P(r)]/m \quad (4.4)$$

$$\mu(r) = c_1 + c_2 P(r)$$

In the following section we derive corresponding motion equations for electric propulsion spacecraft.

4.2.3 Motion equations for electric propulsion system

For our analysis a system description with respect to a polar coordinate system is beneficial for planar transfers; that is, the position vector $\mathbf{r} = (r, \theta)^T$. For the three-dimensional analysis we use a cartesian coordinate description. The equations of motion are then derived in a straightforward manner using Lagrange's equation

$$\frac{d}{dt} \frac{\partial \mathcal{L}}{\partial \dot{q}_i} - \frac{\partial \mathcal{L}}{\partial q_i} = Q_i, \quad i = 1, \dots, n \quad (4.5)$$

In equation (4.5) the Lagrangian $\mathcal{L} = \mathcal{T} - \mathcal{V}$ is computed as the difference between the kinetic and the potential energy of the system, q_i are the generalized coordinates, and Q_i are the generalized forces of the system.

Using polar coordinates, the general motion equations for the planar system model of a controlled electric spacecraft are then readily obtained as

$$\ddot{r} = r\dot{\theta}^2 - \mu_{\odot}/r^2 + \tau(r) \cos \alpha_r \quad (4.6)$$

$$r\ddot{\theta} = -2\dot{r}\dot{\theta} + \tau(r) \sin \alpha_r \quad (4.7)$$

$$\dot{m} = \mu(r) \quad (4.8)$$

where α_r is the control variable. The specific thrust $\tau(r)$ and the mass flow function $\mu(r)$ depend on the particular spacecraft propulsion system and are presented in equations (4.4) for nuclear-electric and solar-electric systems.

For the three-dimensional analysis we use a cartesian coordinate description with $\mathbf{r} = (x, y, z)^\top$. Applying Lagrange's equations the equations of motion are readily obtained as

$$\ddot{x} = -\frac{\mu_\odot x}{r^3} + \tau(r) \cos \alpha_z \cos \alpha_{xy} \quad (4.9)$$

$$\ddot{y} = -\frac{\mu_\odot y}{r^3} + \tau(r) \cos \alpha_z \sin \alpha_{xy} \quad (4.10)$$

$$\ddot{z} = -\frac{\mu_\odot z}{r^3} + \tau(r) \sin \alpha_z \quad (4.11)$$

$$\dot{m} = \mu(r) \quad (4.12)$$

In the subsequent section we discuss system models and equations of motion for solar sail spacecraft.

4.3 Solar Sail Spacecraft

In this section we discuss a solar radiation pressure model and subsequently derive motion equations for solar sail spacecraft for planar and three-dimensional analysis.

4.3.1 Solar radiation pressure model

The solar radiation pressure forces are due to photons γ impinging on the spacecraft surface, for example, the solar sail. If a fraction, γ_a , of the interacting photons is absorbed, a fraction, γ_s , is specularly reflected, and a fraction, γ_d , is diffusely reflected, then by conservation of energy

$$\gamma_a + \gamma_s + \gamma_d = 1 \quad (4.13)$$

The radiation forces due to absorption, specular and diffuse reflection can be written as⁶¹

$$\mathbf{f}_a = \frac{\gamma_a f_\gamma \text{AU}^2}{r^2} (\mathbf{n}_\gamma^\top \mathbf{S}) \mathbf{S}, \quad \mathbf{f}_s = \frac{2\gamma_s f_\gamma \text{AU}^2}{r^2} (\mathbf{n}_\gamma^\top \mathbf{S})^2 \mathbf{n}_\gamma, \quad (4.14)$$

and

$$\mathbf{f}_d = \frac{\gamma_d f_\gamma \text{AU}^2}{r^2} (\mathbf{n}_\gamma^\top \mathbf{S}) (\mathbf{S} + 2\mathbf{n}_\gamma/3), \quad \text{with} \quad f_\gamma = p_\gamma A \quad (4.15)$$

and where A is the solar sail surface area, $p_\gamma = 4.563 \times 10^{-6}$ N/m² is the nominal solar radiation pressure constant at 1 AU, where the unit of AU is chosen such that $[AU] = [r]$. Furthermore, \mathbf{n}_γ is the solar sail surface area vector, and \mathbf{S} is the unit vector pointing from the Sun center to the spacecraft as illustrated in Figure 4.2. The total solar radiation pressure force may then be written as

$$\mathbf{f}_\gamma = \mathbf{f}_a + \mathbf{f}_s + \mathbf{f}_d = \frac{f_\gamma \text{AU}^2}{r^2} (\mathbf{n}_\gamma^\top \mathbf{S}) \{ (1 - \gamma_s) \mathbf{S} + [2\gamma_s (\mathbf{n}_\gamma^\top \mathbf{S}) + 2\gamma_d/3] \mathbf{n}_\gamma \} \quad (4.16)$$

which simplifies to

$$\begin{aligned} \mathbf{f}_\gamma &= \frac{f_\gamma \text{AU}^2}{r^2} \cos \alpha_r \{ (1 - \gamma_s) \mathbf{S} + [2\gamma_s \cos \alpha_r + 2\gamma_d/3] (\mathbf{S} \cos \alpha_r + \mathbf{S}_\perp \sin \alpha_r) \} \\ &= \frac{f_\gamma \text{AU}^2}{r^2} \cos \alpha_r \{ (1 - \gamma_s + \cos \alpha_r (2\gamma_s \cos \alpha_r + 2\gamma_d/3)) \mathbf{S} \\ &\quad + \sin \alpha_r (2\gamma_s \cos \alpha_r + 2\gamma_d/3) \mathbf{S}_\perp \} \\ &\triangleq f_\gamma^{\mathbf{S}} \mathbf{S} + f_\gamma^{\mathbf{S}_\perp} \mathbf{S}_\perp \end{aligned} \quad (4.17)$$

observing that $(\mathbf{n}_\gamma^\top \mathbf{S}) = \cos \alpha_r$ and introducing \mathbf{S}_\perp as the unit vector in the $\mathbf{n}_\gamma \mathbf{S}$ -plane and orthogonal to \mathbf{S} . Note that we assume the solar sail to be perfectly flat with homogeneous solar radiation pressure distribution over the entire sail surface.

For later reference we derive the solar radiation pressure torque g_γ for the solar sail spacecraft. With the surface area of other parts of the spacecraft being negligibly small, g_γ results

$$g_\gamma = d_s (-\sin \alpha_r f_\gamma^{\mathbf{S}} + \cos \alpha_r f_\gamma^{\mathbf{S}_\perp}) = d_s \frac{f_\gamma \text{AU}^2}{r^2} \cos \alpha_r \sin \alpha_r (1 - \gamma_s) \quad (4.18)$$

where d_s is the distance between the spacecraft center of mass \bullet and the center of solar radiation pressure of the sail \odot . Note that we assume the solar sail to be perfectly flat and a homogeneous solar radiation pressure distribution over the entire sail surface. Note that the solar radiation pressure torque does not depend on γ_a and is equal to zero for a perfectly reflective solar sail where $\gamma_s = 1$.

4.3.2 Motion equations for solar sail system

Using equations (4.17) we introduce the solar sail characteristic acceleration as

$$\beta = 2f_\gamma \text{AU}^2/m \quad (4.19)$$

For the planar analysis we then employ a system description based on polar coordinates. With the solar radiation pressure model discussed in Section 4.3.1 the equations of motion yield

$$\ddot{r} = r\dot{\theta}^2 - \frac{\mu_{\odot}}{r^2} + \frac{\beta}{r^2} \cos^3 \alpha_r \quad (4.20)$$

$$\ddot{\theta} = -\frac{2\dot{r}\dot{\theta}}{r} + \frac{\beta}{r^3} \cos^2 \alpha_r \sin \alpha_r \quad (4.21)$$

We employ spherical coordinates $\mathbf{r} = (r, \theta, \phi)^T$ for the three-dimensional analysis. Using Lagrange's equation the resulting motion equations result in

$$\ddot{r} = r\dot{\theta}^2 \cos^2 \phi + r\dot{\phi}^2 - \frac{\mu_{\odot}}{r^2} + \frac{\beta}{r^2} \cos^3 \alpha_r \quad (4.22)$$

$$\ddot{\theta} = \frac{1}{r \cos \phi} [2r\dot{\theta}\dot{\phi} \sin \phi - 2\dot{r}\dot{\theta} \cos \phi + \beta \cos^2 \alpha_r \sin \alpha_r \sin \alpha_{\phi\theta}/r^2] \quad (4.23)$$

$$\ddot{\phi} = -\frac{2\dot{r}\dot{\phi}}{r} - \dot{\theta}^2 \sin \phi \cos \phi + \frac{\beta}{r^3 \cos \phi} \cos^2 \alpha_r \sin \alpha_r \cos \alpha_{\phi\theta} \quad (4.24)$$

4.4 Summary

In this chapter we have introduced system models for solar-electric, nuclear-electric, and solar sail spacecraft for two- and three-dimensional analysis. We have used Lagrange's equation to derive the equations of motion for the system models and now proceed to the next chapter to investigate optimal control problems for minimum-time transfers.

Optimal Control Analysis

In this chapter we formulate the optimal control problem for various low-thrust systems and derive necessary optimality conditions. We first focus on two-dimensional system descriptions and then generalize the problem formulation to three dimensions. In Section 5.1 we analyze the planar minimum-time optimal control problem for nuclear-electric, solar-electric, and solar sail spacecraft. We perform symmetry analysis and identify and derive various symmetry transformations in Section 5.1.4. Subsequently, in Section 5.1.5 we validate the optimization algorithm developed in Chapter 3 and present new solution families to the optimal control problem. The trade studies presented in Section 5.1.5 are the starting point for the three-dimensional optimal control analysis discussed in Section 5.2 in which we focus on the implementation of homotopy methods. In particular, we demonstrate how to compute transfer trajectories for a solar sail spacecraft using corresponding solution trajectories of a nuclear-electric spacecraft.

5.1 Two-dimensional Analysis

We employ polar coordinates to develop the system descriptions for planar transfer scenarios. The gravitational potential and the solar radiation field of the Sun are naturally described in polar coordinates and so are the boundary conditions for transfers between circular (and elliptical) planetary orbits. In this section we set up the optimal control problem for nuclear-electric, solar-electric, and solar sail spacecraft. The system models and corresponding equations of motion are discussed in Chapter 4.

5.1.1 Nuclear-electric propulsion systems

The motion equations for a nuclear-electric propulsion spacecraft in polar coordinates were derived in Section (4.9–4.12) and are given by

$$\ddot{r} = r\dot{\theta}^2 - \frac{\mu_{\odot}}{r^2} + \frac{T}{m} \cos \alpha_r \quad (5.1)$$

$$\ddot{\theta} = -\frac{2\dot{r}\dot{\theta}}{r} + \frac{T}{mr} \sin \alpha_r \quad (5.2)$$

$$\dot{m} = -c \quad (5.3)$$

By defining a set of intermediate variables $v_{\theta} \triangleq r\dot{\theta}$ and $v_r \triangleq \dot{r}$ we can rewrite the second-order differential equations (5.1,5.2) as a set of first-order differential equations. By a minor abuse of notation and following the procedure outlined in Appendix B, we use $r, \theta,$ and m to denote nondimensional variables henceforth; the tilde-notation $\tilde{\square}$ is used for dimensional variables. The nondimensional motion equations can then be written as

$$\dot{r} = v_r \quad (5.4)$$

$$\dot{\theta} = \frac{v_{\theta}}{r} \quad (5.5)$$

$$\dot{v}_r = \frac{v_{\theta}^2}{r} - \frac{1}{r^2} + \tau \cos \alpha_r \quad (5.6)$$

$$\dot{v}_{\theta} = -\frac{v_r v_{\theta}}{r} + \tau \sin \alpha_r \quad (5.7)$$

$$\dot{\tau} = \tau^2 \kappa \quad (5.8)$$

Note that we replaced the spacecraft mass m by a new state variable, the specific, nondimensional thrust τ via

$$\frac{\tilde{T}}{\tilde{m}} \triangleq \tilde{\tau}, \quad \text{and with } \tilde{m}' = -\tilde{c} \quad \rightarrow \quad \tilde{\tau}' = -\frac{\tilde{T}\tilde{m}'}{\tilde{m}^2} \equiv \frac{\tilde{\tau}^2 \tilde{c}}{\tilde{T}} \triangleq \tilde{\tau}^2 \tilde{\kappa} \quad (5.9)$$

introducing the so-called thrust efficiency parameter κ . Choosing the specific thrust rather than the spacecraft mass as a state variable simplifies the costate analysis and yields less complex expressions for the costate differential equations.

The Hamiltonian \mathcal{H} can then be written as

$$\mathcal{H} = \lambda_1 v_r + \lambda_2 v_{\theta}/r + \lambda_3 \left(\frac{v_{\theta}^2}{r} - \frac{1}{r^2} + \tau \cos \alpha_r \right) + \lambda_4 \left(-\frac{v_r v_{\theta}}{r} + \tau \sin \alpha_r \right) + \lambda_5 \tau^2 \kappa \quad (5.10)$$

The corresponding costate equations $\dot{\lambda} = -\partial\mathcal{H}/\partial\mathbf{x}$ are

$$\dot{\lambda}_1 = -\lambda_2 v_\theta / r^2 + \lambda_3 (-2/r^3 + v_\theta^2 / r^2) + \lambda_4 (-v_r v_\theta / r^2) \quad (5.11)$$

$$\lambda_2 = \text{const.} \quad \begin{cases} = 0 & \text{iff } \theta(t_f) = \text{free} \\ \neq 0 & \text{iff } \theta(t_f) = \theta_f \end{cases} \quad (5.12)$$

$$\dot{\lambda}_3 = -\lambda_1 + \lambda_4 v_\theta / r \quad (5.13)$$

$$\dot{\lambda}_4 = -\lambda_2 / r - 2\lambda_3 v_\theta / r + \lambda_4 v_r / r \quad (5.14)$$

$$\dot{\lambda}_5 = -\lambda_3 \cos \alpha_r - \lambda_4 \sin \alpha_r - 2\lambda_5 \tau \kappa \quad (5.15)$$

Note that θ is an ignorable coordinate; the corresponding costate λ_2 is therefore a constant and zero if $\theta(t_f)$ is free. In this case the dimensionality of the search space decreases by one. For $\theta(t_f)$ given, $\lambda_2(t_0) \equiv \lambda_2$ remains an unknown of the optimization problem.

The optimal control angle is obtained by setting the first derivative of the Hamiltonian with respect to the control angle equal to zero.

$$\frac{\partial\mathcal{H}}{\partial\alpha_r} = 0 = -\lambda_3 \tau \sin \alpha_r + \lambda_4 \tau \cos \alpha_r \rightarrow \frac{\sin \alpha_r}{\cos \alpha_r} = \frac{\lambda_4}{\lambda_3} \quad (5.16)$$

To remove sign ambiguities in the optimal control law we note that

$$\frac{\partial^2\mathcal{H}}{\partial\alpha_r^2} = -\lambda_3 \tau \cos \alpha_r - \lambda_4 \tau \sin \alpha_r > 0 \quad (5.17)$$

Using information from equation (5.16) we identify two conditions on the sign of the cosine and the sine of the control angle in the form

$$\begin{aligned} -\lambda_3 \cos \alpha_r > 0 & \rightarrow \text{sign}(\lambda_3) = -\text{sign}(\cos \alpha_r) \\ -\lambda_4 \sin \alpha_r > 0 & \rightarrow \text{sign}(\lambda_4) = -\text{sign}(\sin \alpha_r) \end{aligned} \quad (5.18)$$

and therefore the correct control law for α_r is obtained as

$$\alpha_r^* = \text{atan2} \left(\frac{-\lambda_4}{-\lambda_3} \right), \quad \text{with } \alpha_r^* \in [0, 2\pi) \quad (5.19)$$

In the following section we discuss the optimal control problem for solar-electric spacecraft.

5.1.2 Solar-electric propulsion systems

The dimensional motion equations for a solar-electric spacecraft in the gravitational field of the Sun in polar coordinates are given by

$$\ddot{r} = r\dot{\theta}^2 - \frac{\mu_{\odot}}{r^2} + \frac{b_1 + b_2P(r)}{m} \cos \alpha_r \quad (5.20)$$

$$\ddot{\theta} = -\frac{2\dot{r}\dot{\theta}}{r} + \frac{b_1 + b_2P(r)}{mr} \sin \alpha_r \quad (5.21)$$

$$\dot{m} = c_1 + c_2P(r) \quad (5.22)$$

where the electric power $P(r)$ is given by¹⁵

$$P(r) = P_0 \frac{a_1r^2 + a_2r + a_3}{r^4(1 + a_4r)} \quad (5.23)$$

and constants a_i, b_i , and c_i are listed in Section 4.2.2. As in Section 5.1.1, we nondimensionalize the equations of motion and adjust the notation for the variables. The nondimensional motion equations are then given by

$$\dot{r} = v_r \quad (5.24)$$

$$\dot{\theta} = \frac{v_{\theta}}{r} \quad (5.25)$$

$$\dot{v}_r = \frac{v_{\theta}^2}{r} - \frac{1}{r^2} + \frac{b_1 + b_2P(r)}{m} \cos \alpha_r \quad (5.26)$$

$$\dot{v}_{\theta} = -\frac{v_r v_{\theta}}{r} + \frac{b_1 + b_2P(r)}{m} \sin \alpha_r \quad (5.27)$$

$$\dot{m} = c_1 + c_2P(r) \quad (5.28)$$

From the system Hamiltonian we can derive the differential equations for the costates in the form

$$\begin{aligned} \dot{\lambda}_1 = & -\lambda_2 v_{\theta}/r^2 + \lambda_3 \left(-2/r^3 + v_{\theta}^2/r^2 - \frac{\partial P(r)}{\partial r} \frac{b_2}{m} \cos \alpha_r \right) + \\ & \lambda_4 \left(-v_r v_{\theta}/r^2 - \frac{\partial P(r)}{\partial r} \frac{b_2}{m} \sin \alpha_r \right) - \lambda_5 \frac{\partial P(r)}{\partial r} c_2 \end{aligned} \quad (5.29)$$

$$\lambda_2 = \text{const.} \begin{cases} = 0 & \text{iff } \theta(t_f) = \text{free} \\ \neq 0 & \text{iff } \theta(t_f) = \theta_f \end{cases} \quad (5.30)$$

$$\dot{\lambda}_3 = -\lambda_1 + \lambda_4 v_{\theta}/r \quad (5.31)$$

$$\dot{\lambda}_4 = -\lambda_2/r - 2\lambda_3 v_{\theta}/r + \lambda_4 v_r/r \quad (5.32)$$

$$\dot{\lambda}_5 = -\frac{1}{m^2} [b_1 + b_2P(r)] (\lambda_3 \cos \alpha_r - \lambda_4 \sin \alpha_r) \quad (5.33)$$

Note that both the state and costate systems for a solar-electric propulsions system are significantly more complex than for a nuclear-electric propulsion system.

The optimal control angle is obtained by setting the first derivative of the Hamiltonian with respect to the control angle equal to zero:

$$\frac{\partial \mathcal{H}}{\partial \alpha_r} = 0 = [b_1 + b_2 P(r)](-\lambda_3 \sin \alpha_r + \lambda_4 \cos \alpha_r) \rightarrow \frac{\sin \alpha_r}{\cos \alpha_r} = \frac{\lambda_4}{\lambda_3} \quad (5.34)$$

Using similar arguments as before in Section 5.1.1 regarding sign and quadrant ambiguities of the control angle it is straightforward to show that the correct control law for α_r has the form

$$\alpha_r^* = \text{atan2} \left(\frac{-\lambda_4}{-\lambda_3} \right), \quad \text{with } \alpha_r^* \in [0, 2\pi) \quad (5.35)$$

The next section is devoted to analyze the optimal control problem of solar sail spacecraft.

5.1.3 Solar sail spacecraft

Dimensional motion equations for a solar sail spacecraft in polar coordinates can be written in the form

$$\ddot{r} = r\dot{\theta}^2 - \frac{\mu_\odot}{r^2} + \frac{\beta}{r^2} \cos^3 \alpha_r \quad (5.36)$$

$$\ddot{\theta} = -\frac{2\dot{r}\dot{\theta}}{r} + \frac{\beta}{r^3} \cos^2 \alpha_r \sin \alpha_r \quad (5.37)$$

The corresponding nondimensional equations of motion are given by

$$\dot{r} = v_r \quad (5.38)$$

$$\dot{\theta} = \frac{v_\theta}{r} \quad (5.39)$$

$$\dot{v}_r = \frac{v_\theta^2}{r} - \frac{1}{r^2} + \frac{\beta}{r^2} \cos^3 \alpha_r \quad (5.40)$$

$$\dot{v}_\theta = -\frac{v_r v_\theta}{r} + \frac{\beta}{r^2} \cos^2 \alpha_r \sin \alpha_r \quad (5.41)$$

From the system Hamiltonian we can derive the differential equations for the costates in the form

$$\dot{\lambda}_1 = \lambda_2 v_\theta / r^2 + \lambda_3 (2\beta \cos^3 \alpha / r^3 + v_\theta^2 / r^2 - 2/r^3) + \lambda_4 (2\beta \sin \alpha \cos^2 \alpha / r^3 - v_r v_\theta / r^2) \quad (5.42)$$

$$\lambda_2 = \text{const.} \begin{cases} = 0 & \text{iff } \theta(t_f) = \text{free} \\ \neq 0 & \text{iff } \theta(t_f) = \theta_f \end{cases} \quad (5.43)$$

$$\dot{\lambda}_3 = -\lambda_1 + \lambda_4 v_\theta / r \quad (5.44)$$

$$\dot{\lambda}_4 = -\lambda_2 / r - 2\lambda_3 v_\theta / r + \lambda_4 v_r / r \quad (5.45)$$

Applying Pontryagin's Minimum Principle, the stationary condition yields

$$\frac{\partial \mathcal{H}}{\partial \alpha} = 0 = -3\lambda_3 \beta \sin \alpha \cos^2 \alpha / r^2 + \lambda_4 \beta (\cos^3 \alpha - 2 \sin^2 \alpha \cos \alpha) / r^2 \quad (5.46)$$

which is satisfied if

$$\begin{cases} \cos \alpha_r^* = 0 \\ \cos \alpha_r^* \neq 0 \quad \text{and} \quad \tan^2 \alpha_r^* + \frac{3\lambda_3}{2\lambda_4} \tan \alpha_r^* - \frac{1}{2} = 0 \end{cases} \quad (5.47)$$

The optimal control angle α_r^* that minimizes the Hamiltonian in equation is then given by

$$\alpha_r^* = \begin{cases} \text{atan} \left((-3\lambda_3 - \sqrt{9\lambda_3^2 + 8\lambda_4^2}) / (4\lambda_4) \right) & \text{if } \lambda_4 \neq 0 \\ 0 & \text{if } \lambda_4 = 0, \lambda_3 < 0 \\ \pm \pi / 2 & \text{if } \lambda_4 = 0, \lambda_3 > 0 \end{cases} \quad (5.48)$$

As a side-note, the second minus sign in the argument of the arctangent in the control law (5.48) is in agreement with the analysis in Wood et al.¹⁰³ and replaces the plus sign used in other papers.^{41,76,77}

5.1.4 Symmetry analysis

In this section we analyze system symmetries starting with the solar sail spacecraft model. For electric-propulsion systems corresponding symmetries are present only for the rather restrictive case of null mass flow. However, by employing homotopy methods these symmetry properties can be used to great advantage to calculate additional solution trajectories for non-zero mass flow, as well.

Solar sail spacecraft

In the following we present and prove two system symmetries summarized in Theorem 1 and Theorem 2. Theorem 1 provides an effective tool to determine optimal return trajectories, which can be used to compute solutions of the \mathcal{P}_1 family efficiently. As pointed out previously, solving the associated Three-Point Boundary Value Problem is not only numerically challenging but is also a time-consuming process. Another interesting symmetry property is formulated in Theorem 2. Using nondimensional analysis one can show similarity of minimum-time solutions for the case when $r(t_f)/r(t_0) = \text{const}$. Moreover, there exists a simple relationship between transfer times and initial (or final) orbit radii for trajectories with $r(t_f)/r(t_0) = \text{const}$.

Definition (Solution Trajectory). A function $\mathbf{\Omega} = (\mathbf{X}, \mathbf{\Lambda}, U, T)^T$ is called a solution trajectory of the optimal control problem if \mathbf{X} and $\mathbf{\Lambda}$ are compatible solutions to the state equations (5.38–5.41) and costate equations (5.42–5.45), respectively, with control history U and transfer time T , for a given set of boundary values.

Theorem 1. *Let $\mathbf{\Omega}$ be a \mathcal{P}_0 solution trajectory satisfying the boundary conditions $\mathbf{X}(t_0) = \mathbf{X}_0$, $\mathbf{X}(t_f) = \mathbf{X}_f$, $\mathbf{\Lambda}(t_0) = \mathbf{\Lambda}_0$, and $\mathbf{\Lambda}(t_f) = \mathbf{\Lambda}_f$, then the costate solution for the corresponding return trajectory $\mathbf{\Omega}^* = (\mathbf{X}^*, \mathbf{\Lambda}^*, U^*, T^*)^T$ satisfies*

$$\Lambda_1^*(t^*) = -\Lambda_1(t), \quad \Lambda_2^*(t^*) = \Lambda_2(t) = 0, \quad \Lambda_3^*(t^*) = \Lambda_3(t), \quad \Lambda_4^*(t^*) = -\Lambda_4(t),$$

with

$$t^* = T - t$$

and where $T = t_f - t_0 = t_f^* - t_0^* = T^*$.

Proof. The boundary conditions for the states are trivially compatible under the symmetry transformation for the independent variable t . With $(d/dt^*) = -(d/dt)$ it follows from equation (5.38) that $v_r^*(t^*) = -v_r(t)$ and from equation (5.40) that $r^*(t^*) = r(t)$. For system invariance the control angle satisfies $\alpha_r^*(t^*) = -\alpha_r(t)$ [equation (5.41)], which is compatible with the symmetry transformations for the Lagrange multipliers and the control law (5.48). Similarly, with the proposed symmetry transformations the costate equations are rendered invariant. \square

Remark. Obviously, $(-\Lambda_1(t_f), \Lambda_3(t_f), -\Lambda_4(t_f)) \mapsto (\Lambda_1^*(t_0^*), \Lambda_3^*(t_0^*), \Lambda_4^*(t_0^*))$ and the return trajectory is readily propagated forward in time. For \mathcal{P}_0 solution trajectories θ is an ignorable coordinate and does not appear in any algebraic constraints; therefore, $\Lambda_2 = \Lambda_2^* = 0$ without loss of generality.

Theorem 2. Let Ω be a \mathcal{P}_0 solution trajectory with $\Xi \triangleq r(t_f)/r(t_0)$ then the equivalent \mathcal{P}_0 solution trajectory Ω^* with $\Xi^* = \Xi$ and $r^*(t_0^*) \neq r(t_0)$ satisfies

$$\begin{aligned} X_1^*(t^*) &= aX_1(t), & X_2^*(t^*) &= X_2(t), & X_3^*(t^*) &= a^{-1/2}X_3(t), & X_4^*(t^*) &= a^{-1/2}X_4(t) \\ \Lambda_1^*(t^*) &= a^{-3/2}\Lambda_1(t), & \Lambda_2^*(t^*) &= \Lambda_2(t) = 0, & \Lambda_3^*(t^*) &= \Lambda_3(t), & \Lambda_4^*(t^*) &= \Lambda_4(t) \end{aligned}$$

with

$$t^* = bt \quad \text{and therefore} \quad T^*/T = b \equiv a^{3/2}$$

where $a = r^*(t_0^*)/r(t_0) = r^*(t_f^*)/r(t_f)$, $T = t_f - t_0$, and $T^* = t_f^* - t_0^*$.

Proof. Using as reference distance units $1 \text{ DU} = r(t_0)$ and $1 \text{ DU}^* = r^*(t_0^*)$ to nondimensionalize motion equations and to obtain the corresponding solution trajectories Ω and Ω^* the state and costate transformations render the systems of differential equations equivalent provided that

$$\tilde{\mu}_\odot \text{ TU}^2 / \text{DU}^3 = \tilde{\mu}_\odot^* \text{ TU}^{*2} / \text{DU}^{*3} \quad \square$$

Remark. For solution trajectories that are not readily obtained with Theorem 1 and Theorem 2, for example, $\Xi^* \neq \Xi$ and $r_0^* \neq r_0$, Theorem 2 can be used to reduce the two-parameter continuation problem to a one-parameter continuation problem as follows:

1. Compute $^*\Omega$ with $^*\Xi = \Xi$, $^*r_0 = r_0^*$ (or $^*r_f = r_f^*$), using Theorem 2
2. Use homotopy to calculate Ω^* with $r_0^* = ^*r_0$ (or $r_f^* = ^*r_f$) fixed

Also note the similarity between Kepler's Third Law and the equation in Theorem 2 describing the relationship between minimum transfer times and corresponding initial (or equivalently final) radial distances.

Figure 5.1 shows three solar sail spacecraft transfer trajectories that are connected by system symmetries discussed in Theorem 1 and Theorem 2. The figure on the left illustrates minimum-time transfers in the xy -plane, the bold bars indicate the orientation of the sail. Note that the symmetry is also reflected in the reflexion symmetry of the control angle histories in the figure on the right-hand side.

Electric spacecraft

For electric propulsion spacecraft the differential equation for the mass flow (e.g. $\dot{m} = -c$) prohibits analogous symmetry transformations. The time derivative generates a

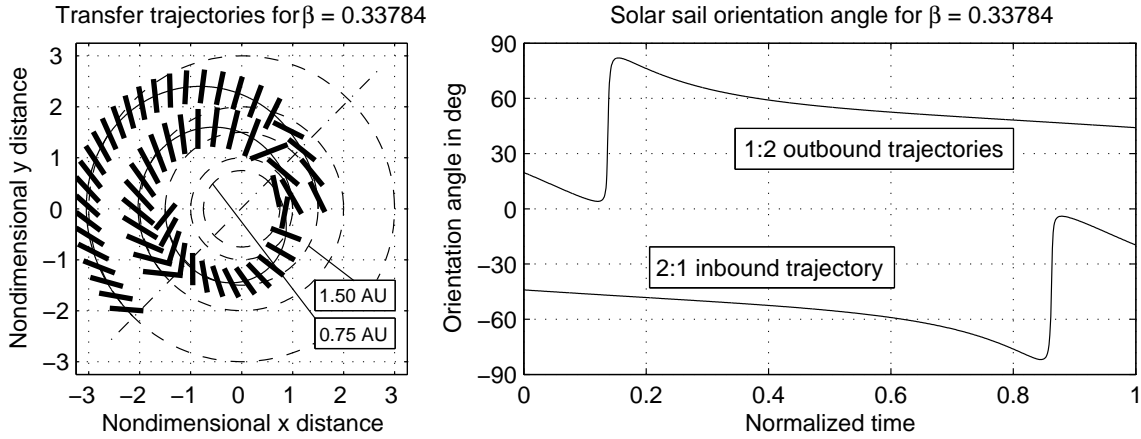


Figure 5.1: System symmetry shown with three transfer trajectories for $\beta = 0.33784$.

coefficient that multiplies the time derivative in the transformed coordinate. For example, $\dot{m} \equiv (d/dt)m = -c \neq -c^* = (d/dt^*)TU^*m^*$, in general, since TU^* can not be chosen arbitrarily. Invariance of the mass flow equation can be achieved by adjusting the mass flow $c \mapsto c^*$ as part of the symmetry transformation. We note, however, that by allowing the mass flow to change as part of the transformation the requirements for performing symmetry transformations are no longer satisfied. The requirements state that invariance of the set of differential equations be achieved by a proper transformation of independent and dependent variables **only**, which – obviously – does not include transformation of system parameters.

With a similar argument we can show that it is not possible to compute an equivalent return trajectory by using the analogous of Theorem 2 for electric spacecraft. Note that with the transformation of the time variable $t^* = T - t$ the mass flow equation changes its sign, that is, $(d/dt)m = -c \mapsto -(d/dt^*)m^* = -c^*$. Both c and c^* denote mass flow rates, which by our definition are positive constants. As a direct result (and unlike for solar sail spacecraft) the minimum transfer time for an Earth-to-Mars transfer can not be equal to the minimum transfer time for a Mars-to-Earth transfer for electric spacecraft.

The algebraic complexity further increases in the case of the motion equations for solar-electric spacecraft model. No symmetry transformations could be identified to this date.

Remark. The process of identifying symmetry transformations for general, non-linear, and coupled differential equations is non-trivial. Imposing boundary conditions on the states and costates to formulate an appropriate optimal control problem adds another level of complexity since the boundary conditions too have to satisfy transformation conditions.

To the best of our knowledge this work presents **the** first attempt to investigate the trajectory optimization problem via symmetry methods. We have shown in this section that system symmetries can be used effectively to solve for optimal control solutions provided, of course, that a) symmetries are present and b) corresponding symmetry transformations can be identified. Especially for higher-dimensional and more complex system descriptions prospects of success of finding symmetry groups of transformations are reasonably unlikely.

5.1.5 Results and propulsion system performance comparison

In this section we first validate the optimization algorithm with some well-documented results in the literature and subsequently present optimal control solutions.

Optimization algorithm validation

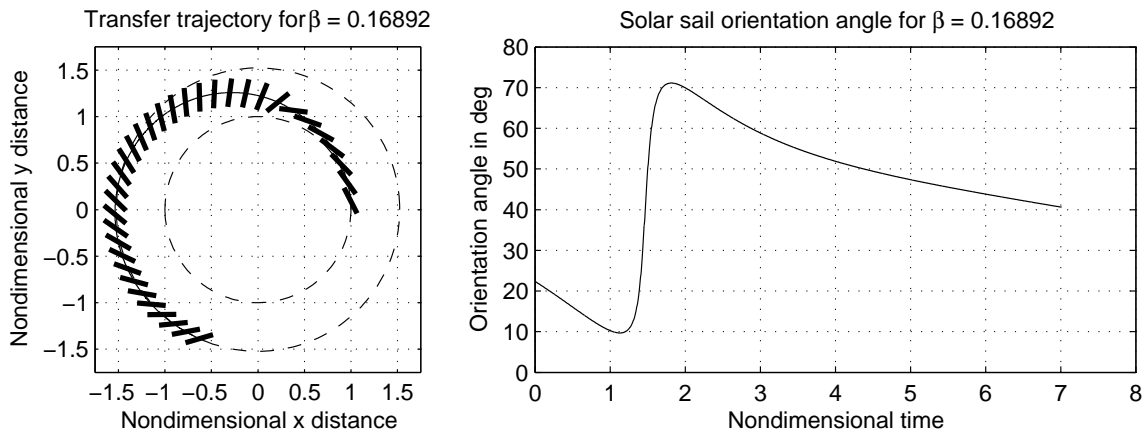
We employ solar sail spacecraft transfer trajectories to test and validate the performance of the optimization algorithm. Results obtained for Earth-to-Mars \mathcal{P}_1 transfers are in excellent agreement with data published by Wood et al.¹⁰³ Table 5.1 shows transfer times and initial and final costates for two different characteristic accelerations. We obtained high-accuracy results with $\|\boldsymbol{\psi}(\mathbf{x}(t_f), t_f)\| < 10^{-14}$, which result in slightly improved transfer times in the order of 10 to 15 hours compared to reported results in Wood et al.¹⁰³ Note that the nondimensional characteristic accelerations of $\beta = 0.16892$ and $\beta = 0.33784$ correspond to nominal values of $\tilde{\beta} = 1 \text{ mm/s}^2$ and $\tilde{\beta} = 2 \text{ mm/s}^2$. The minimum transfer times correspond to 323.87 and 407.62 days, respectively (1 TU = $365.25/(2\pi)$ days = 58.1313 days). The transfer trajectories and corresponding control angle histories are illustrated in Figure 5.2 and Figure 5.3. The plots on the left-hand side show transfer trajectories and sail orientations in the xy -plane; the time histories of the sail orientation angles are shown in plots on the right-hand side.

Systems performance comparison

Figures 5.4 and 5.5 show minimum-time orbit transfer trajectories between Earth and Mars for a nuclear-electric spacecraft with $\tau_0 = 0.16892$ and $\kappa = 0.50604$ which corresponds to an initial specific thrust of $\tilde{\tau}_0 = 1 \text{ mm/s}^2$ and a specific impulse of $I_{sp} = 6000 \text{ s}$. Comparing the control angle histories for both transfers it seems that the two scenar-

Table 5.1: Minimum transfer times and corresponding costates for Earth-to-Mars transfers.

| Analysis Author | Characteristic acceleration β | Transfer time T | Initial costates $\lambda(0)$ | Final costates $\lambda(T)$ |
|---------------------------------|---|---|--|--|
| Wood, et al. ¹⁰³ | $\left\{ \begin{array}{l} 0.16892 \\ 0.33784 \end{array} \right.$ | $\left\{ \begin{array}{l} 7.02232 \\ 5.57911 \end{array} \right.$ | $\begin{pmatrix} -7.40581 \\ -4.22855 \\ -7.91115 \end{pmatrix}$ | $\begin{pmatrix} -21.5481 \\ + 8.5025 \\ -46.6174 \end{pmatrix}$ |
| | | | $\begin{pmatrix} -3.68044 \\ -2.59597 \\ -2.56421 \end{pmatrix}$ | $\begin{pmatrix} -14.9271 \\ +10.1662 \\ -29.6344 \end{pmatrix}$ |
| Kim | $\left\{ \begin{array}{l} 0.16892 \\ 0.33784 \end{array} \right.$ | $\left\{ \begin{array}{l} 7.01204 \\ 5.57134 \end{array} \right.$ | $\begin{pmatrix} -7.41099 \\ -4.23234 \\ -7.90591 \end{pmatrix}$ | $\begin{pmatrix} -21.5482 \\ + 8.5063 \\ -46.5737 \end{pmatrix}$ |
| | | | $\begin{pmatrix} -3.68301 \\ -2.59741 \\ -2.56208 \end{pmatrix}$ | $\begin{pmatrix} -14.9274 \\ +10.1619 \\ -29.6045 \end{pmatrix}$ |
| Powers, et al. ^{76,77} | 0.33784 | 5.57 | – | – |

**Figure 5.2:** Transfer trajectory and solar sail orientation angle history for an Earth-to-Mars transfer with $\beta = 0.16892$.

ios are connected by a symmetry transformation; transfer times are close, however, not identical ($T^{\min} = 3.050$ (Mars-to-Earth) compared to $T^{\min} = 3.041$ (Earth-to-Mars))! As pointed out in Section 5.1.4 the non-zero mass flow is responsible for symmetry breaking.

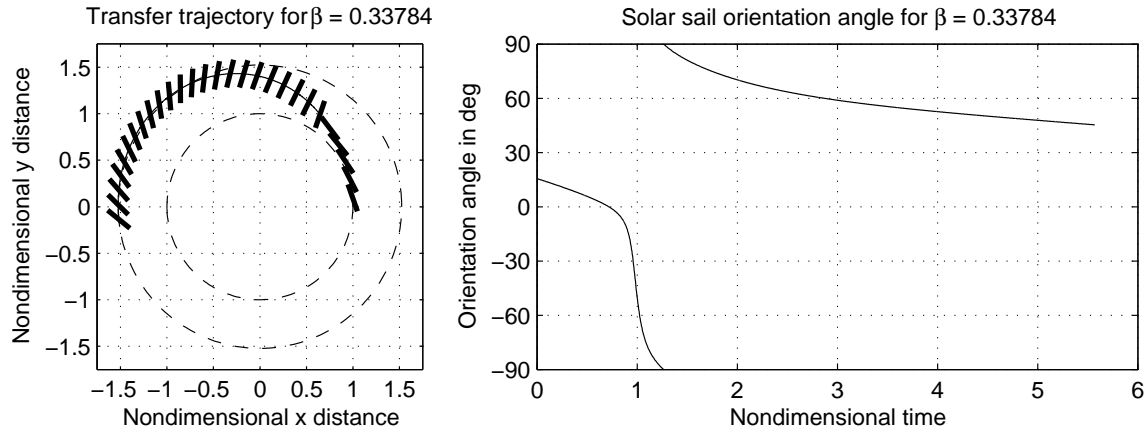


Figure 5.3: Transfer trajectory and solar sail orientation angle history for an Earth-to-Mars transfer with $\beta = 0.33784$.

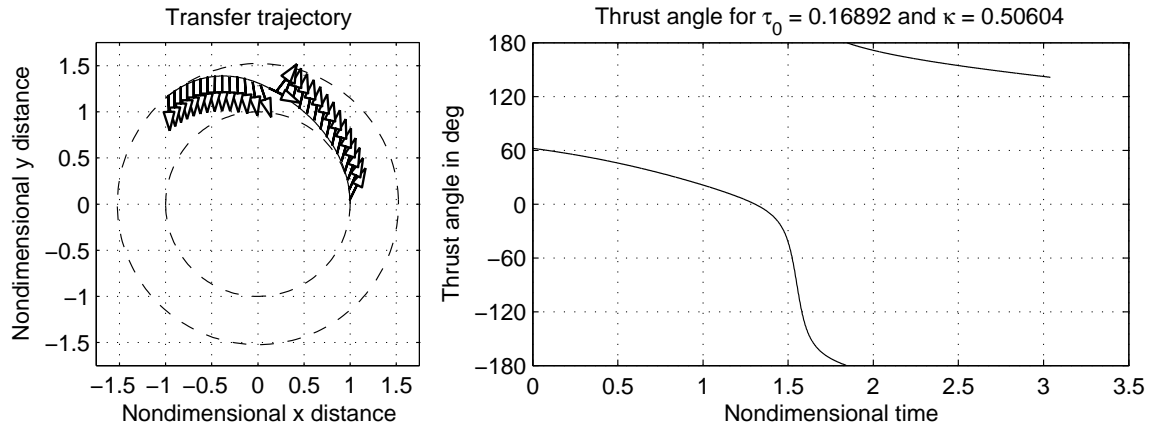


Figure 5.4: Transfer trajectory and thrust angle history for an Earth-to-Mars transfer with $\tau_0 = 0.16892$ and $\kappa = 0.50604$.

Figure 5.6 shows orbit transfer time as a function of final orbit radius comparing solar sail and nuclear-electric spacecraft and for an initial orbit radius is 1 AU. Curves 1,2, and 3 (solid-dotted lines) correspond to solar sail spacecraft with increasing characteristic acceleration; curve pairs 4 and 5 (solid lines) correspond to nuclear-electric spacecraft with initial specific thrust of $\tilde{\tau}_0 = 0.5 \text{ mm/s}^2$ and $\tilde{\tau}_0 = 1.0 \text{ mm/s}^2$ and specific impulse of $I_{sp} = 3000 \text{ s}$ and $I_{sp} = 6000 \text{ s}$. The figure shows that electric propulsion systems in general outperform solar sail spacecraft for outbound trajectories $r(t_f) > r(t_0)$ provided that there are no constraints on propulsion system mass (fuel). For inbound transfers we notice an increased effectiveness of solar sail spacecraft due to the increasing solar

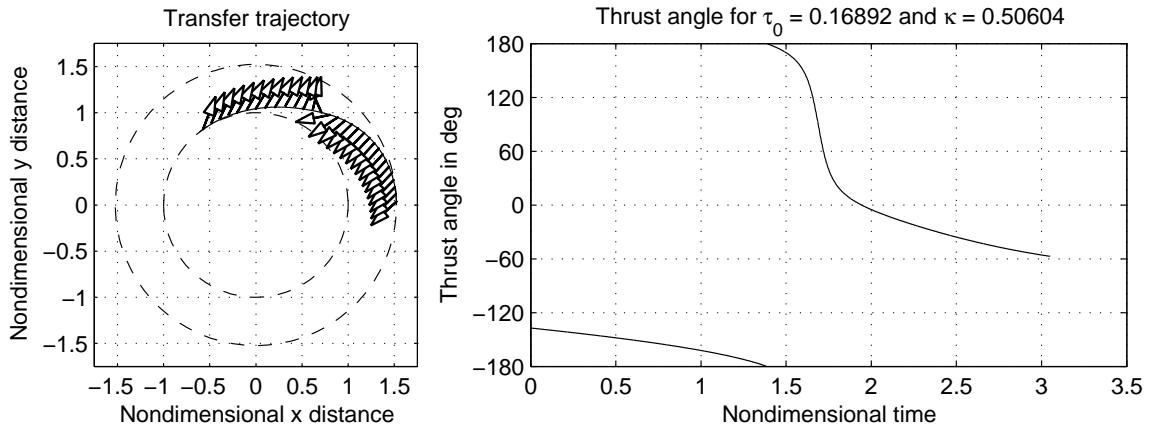


Figure 5.5: Transfer trajectory and thrust angle history for an Mars-to-Earth transfer with $\tau_0 = 0.16892$ and $\kappa = 0.50604$.

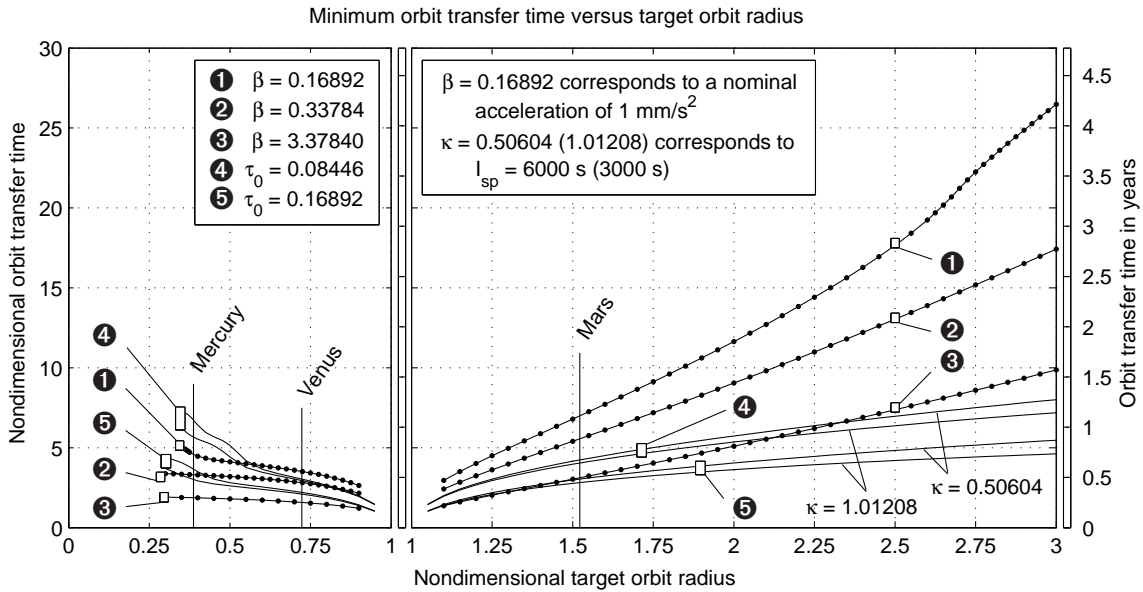


Figure 5.6: Transfer time as a function of target orbit radius for solar sail spacecraft (solid-dotted lines) and nuclear-electric propulsion spacecraft (solid lines). The initial orbit radius is 1 AU.

radiation pressure.

Minimum-time Earth-Mars-Earth double orbit transfer trajectories for solar sail spacecraft and nuclear-electric spacecraft are illustrated in Figure 5.7 and Figure 5.8. Because of system symmetry the overall transfer time for the solar sail spacecraft is simply twice

the transfer time of the corresponding \mathcal{P}_1 solution, that is, $T_{\mathcal{P}_2} = 2T_{\mathcal{P}_1} = 11.142$. This particular symmetry is also reflected in the mirror-symmetry of the solar sail orientation angle history. Note that the second half of the control angle history ($t \in [5.571, 11.142]$) is obtained by simply reflecting the first half of the control angle history ($t \in [0, 5.571]$) once about the x -axis and once about the y -axis. In comparison, Figure 5.8 clearly illustrates the lack of the corresponding symmetry transformation for the electric-spacecraft. In addition, the outbound leg of the \mathcal{P}_2 transfer takes approximately 45% longer than the inbound leg which is, of course, due to the increased thrust acceleration as a result of decreasing spacecraft mass.

Multiple solutions to minimum-time transfer problem are possible. Figure 5.9 shows two globally minimal Earth-Mars \mathcal{P}_3 solutions for an initial angular separation between Mars and Earth of $\Delta\Theta(t_0) = 1.117$ rad and a characteristic acceleration of $\beta = 0.135136$. For the two significantly different trajectories, we refer to the spacecraft as being in either “sleep” or “catch-up” mode. Sleep-mode solutions are characterized by a dramatic initial increase of the radial distance of the spacecraft reducing its angular rate. Midway through the transfer the angular rate is further decreased by reducing the sail orientation angle, gravity becomes dominant, and the spacecraft naturally falls back into the target orbit for rendezvous. Comparing sleep and catch-up type trajectories, the latter are more dynamically “active”. As illustrated in Figure 5.9 the control angle history for the sleep mode trajectory shows a distinctively more moderate functional behavior. Additionally, catch-up mode trajectories typically include one or more solar gravity/solar radiation assists. The tangential velocity v_θ is generally higher for catch-up mode than for corresponding sleep mode trajectories. Not surprisingly, once close to the object planet (Earth) the spacecraft in catch-up mode approaches its target from “behind”. In sleep mode the spacecraft slows down appropriately to be approached by its target.

Obviously, the two trajectories in Figure 5.9 are members of two fundamentally different solution branches. For fixed initial angular separation $\Delta\Theta(t_0)$ of the planets, there exist in general an infinite number of locally optimal \mathcal{P}_3 solutions but only one or two globally optimal solution trajectories as illustrated in Figure 5.10. Varying $\Delta\Theta(t_0)$, the minimum-time \mathcal{P}_3 trajectory to transfer between arbitrary points on the initial and target orbits coincides with the corresponding \mathcal{P}_1 solution; that is, $T_{\mathcal{P}_2}^{\min} = T_{\mathcal{P}_1}$. In Figure 5.10 the corresponding \mathcal{P}_1 -type solution is located at $T_{\mathcal{P}_3}^{\min} = 7.01204$ and $\Delta\Theta(t_0) = 2.67402$ rad with $\beta = 0.16892$ according to Table 5.1. Starting at the \mathcal{P}_1 -type solution, the \mathcal{P}_3 solution family consists of two solution branches: for decreasing $\Delta\Theta(t_0)$ we find catch-up type solutions, whereas for increasing $\Delta\Theta(t_0)$ sleep mode turns out to be more time-efficient. The two branches represent globally optimal solutions for $T_{\mathcal{P}_3} \leq T_{\mathcal{P}_3}^{\max} = 12.59186$, where the branches intersect (first crossover = Darboux point) and the global optimum switches

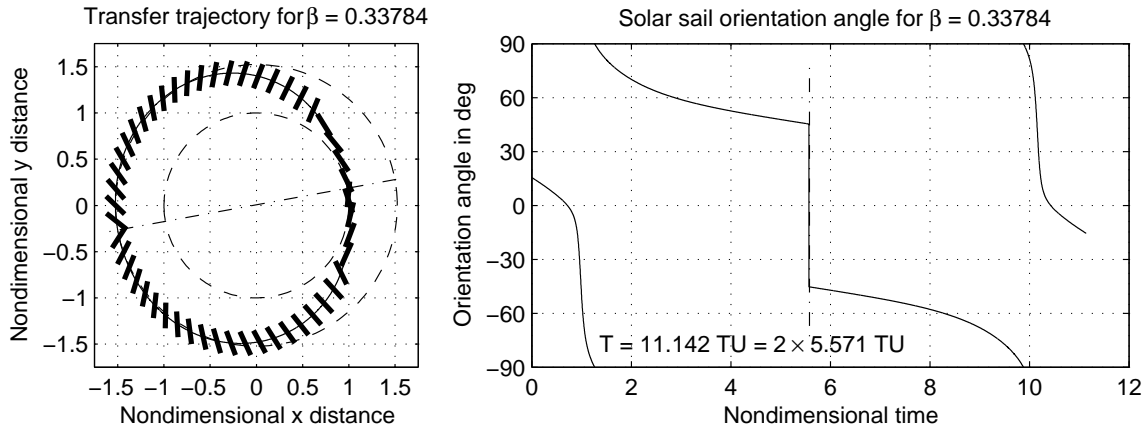


Figure 5.7: Minimum-time Earth-Mars-Earth double orbit transfer trajectory and solar sail orientation angle history for $\beta = 0.33784$.

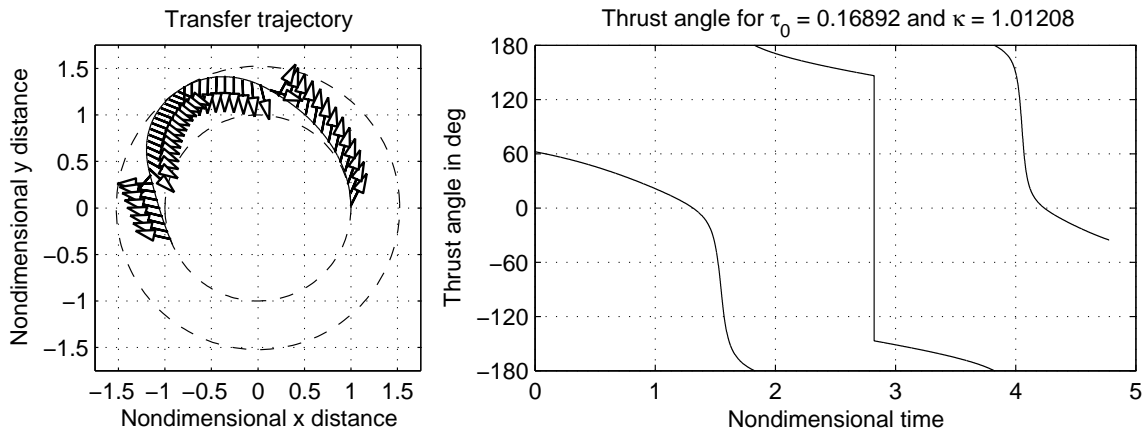


Figure 5.8: Minimum-time Earth-Mars-Earth double orbit transfer trajectory and thrust angle history for $\tau = 0.16892$ and $\kappa = 1.01208$.

from sleep- to catch-up-type solution trajectories, and vice versa. Note that the Darboux point marks solution trajectories for pessimal $\Delta\Theta(t_0)$. A further increase or decrease in $\Delta\Theta(t_0)$ yields locally optimal solutions, with faster, globally optimal solutions readily apparent. Tracking locally optimal solution branches we find additional crossover points. Figure 5.11 shows solution trajectories for a solar sail spacecraft with $\beta = 0.33784$ at the second crossover point.

The connection between the two solution families introduced with Figure 5.10 is illustrated in Figure 5.12. The middle plot shows the optimal \mathcal{P}_3 transfer option (bold dashed

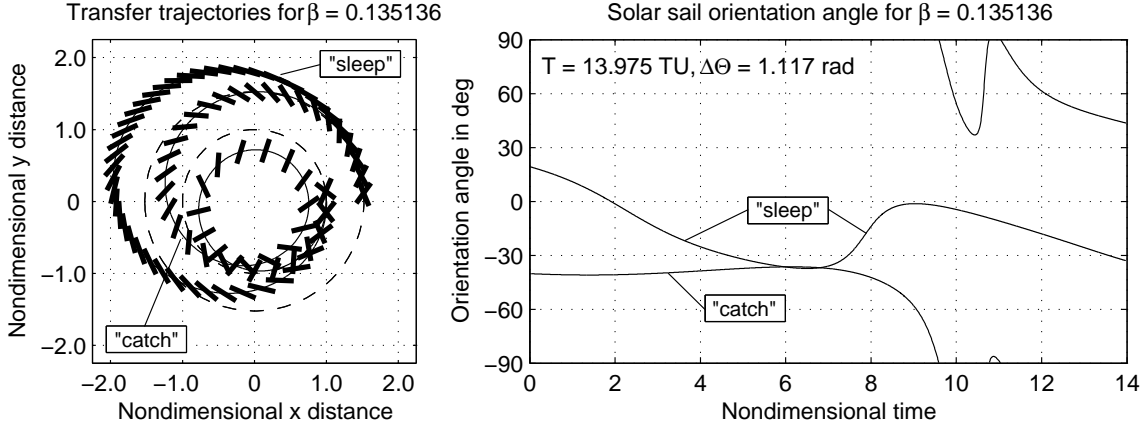


Figure 5.9: Minimum-time Mars-to-Earth rendezvous trajectories at first crossover point for $\beta = 0.135136$.

line) that corresponds to the \mathcal{P}_1 solution trajectory. For decreasing values of initial angular separation between Mars and Earth catch-type transfers are more time-efficient. The plot on the left-hand side of Figure 5.12 shows catch-type transfer trajectories for several initial Mars-Earth constellations. Note that the initial segments of all trajectories are similar to the optimal \mathcal{P}_3 transfer (bold dashed line in middle plot). The shape of the second trajectory segment depends on $\Delta\Theta(t_0)$, the initial angular separation between Mars and Earth. For small deviations of $\Delta\Theta(t_0)$ from $\Delta\Theta^{\text{opt}}(t_0)$ the spacecraft performs a relatively short swing-by maneuver about the Sun. As $\Delta\Theta(t_0)$ decreases, transfer time increases and the approaches of the spacecraft with Sun become closer; the rendezvous location of spacecraft and Earth moves anti-clockwise. On the other hand, for increasing values of $\Delta\Theta(t_0)$, the spacecraft is initially “too far ahead” of Earth to perform an optimal \mathcal{P}_3 transfer (bold dashed line). The transfer trajectory solutions follow the sleep-mode branch. The right-hand side plot in Figure 5.12 shows some sleep-mode solutions for different $\Delta\Theta(t_0)$. For increasing values in initial angular separation between Mars and Earth, the spacecraft moves further out into space allowing the spacecraft to reduce its angular velocity appropriately for a rendezvous with Earth. As expected, transfer time increases for increasing values of $\Delta\Theta(t_0)$.

Figures 5.13 and 5.14 illustrate minimum transfer time as a function of initial angular separation $\Delta\Theta(t_0)$ for different solar sail spacecraft and nuclear electric spacecraft for Earth-to-Mars and Mars-to-Earth \mathcal{P}_3 transfers. Unlike for \mathcal{P}_1 solutions, symmetries of the \mathcal{P}_3 family are less distinct. Nevertheless, minimum $T_{\mathcal{P}_3}^{\text{min}}$ and maximum $T_{\mathcal{P}_3}^{\text{max}}$ transfer times agree for both Earth-to-Mars and Mars-to-Earth \mathcal{P}_3 solution families for solar sail spacecraft. Because of non-zero mass flow and the resulting symmetry breaking transfer

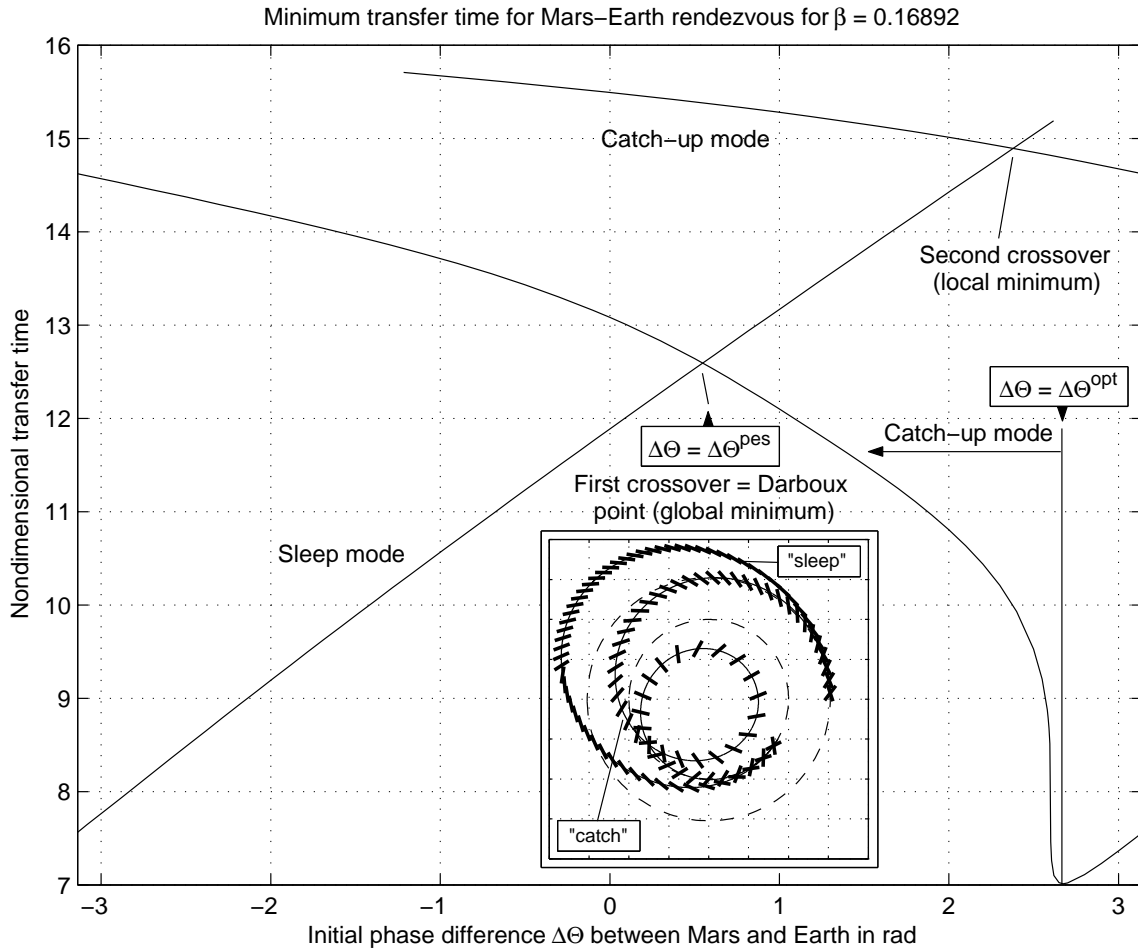


Figure 5.10: Minimum transfer time for Mars-to-Earth rendezvous for $\beta = 0.16892$.

times for Earth-to-Mars and Mars-to-Earth trajectories do not agree in the case of electric spacecraft.

Comparing the performance of electric spacecraft we find that for comparable thrust characteristics nuclear-electric spacecraft outperform solar-electric spacecraft, especially for sleep-mode transfer trajectories. Figure 5.15 shows spacecraft with nuclear propulsion systems with $\tau_0 = 0.16892$ and $\tau_0 = 0.08846$ and for thrust efficiency parameters of $\kappa = 0.50604$ and $\kappa = 1.10208$. The solar-electric spacecraft is equipped with a 3 kW (reference) power source and is comparable to the nuclear spacecraft with $\tau_0 = 0.16892$ and $\kappa = 0.50604$. Note the performance improvement for the solar-electric system relative to the nuclear spacecraft for catch-type solution trajectories. For values of $\Delta\Theta(t_0) < -2$ transfer times are shorter for the solar-electric spacecraft which is due to the close en-

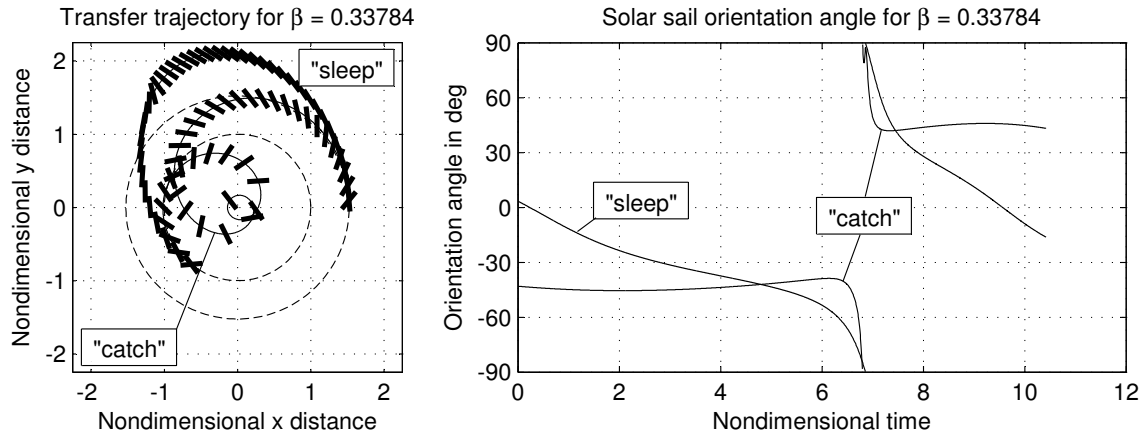


Figure 5.11: Minimum-time Mars-to-Earth rendezvous trajectories for second crossover point and for $\beta = 0.33784$.

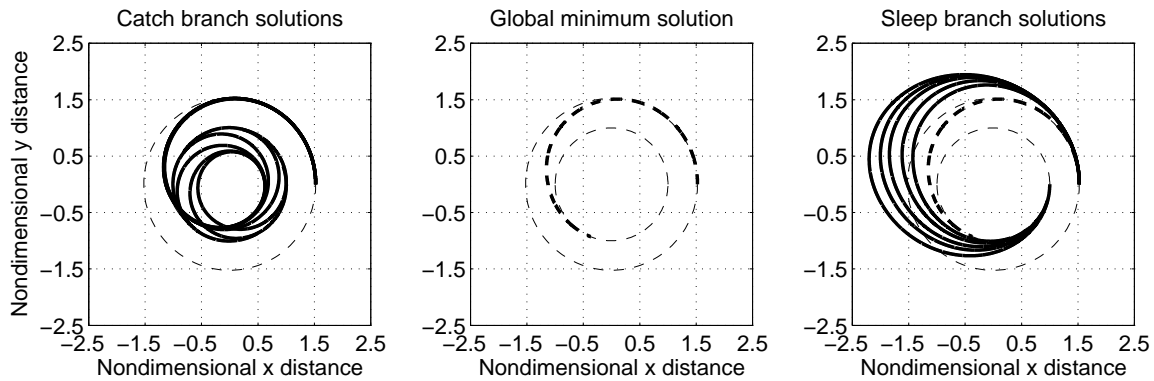


Figure 5.12: Trajectory geometry comparison for sleep-type and catch-type solution trajectories for minimum-time Mars-to-Earth rendezvous for a solar sail spacecraft.

counter of the spacecraft with the Sun during the gravity/solar radiation assist increasing the available electrical power $P(r)$ and therefore also the specific thrust.

5.2 Three-dimensional Analysis

In this section we focus on homotopy methods to solve the minimum-time optimal control problem. As pointed out in Section 3.2.4 homotopy methods present an effective technique to solve complex problems by first analyzing a related but simpler problem. In the following we demonstrate how to compute solution trajectories for solar sail spacecraft

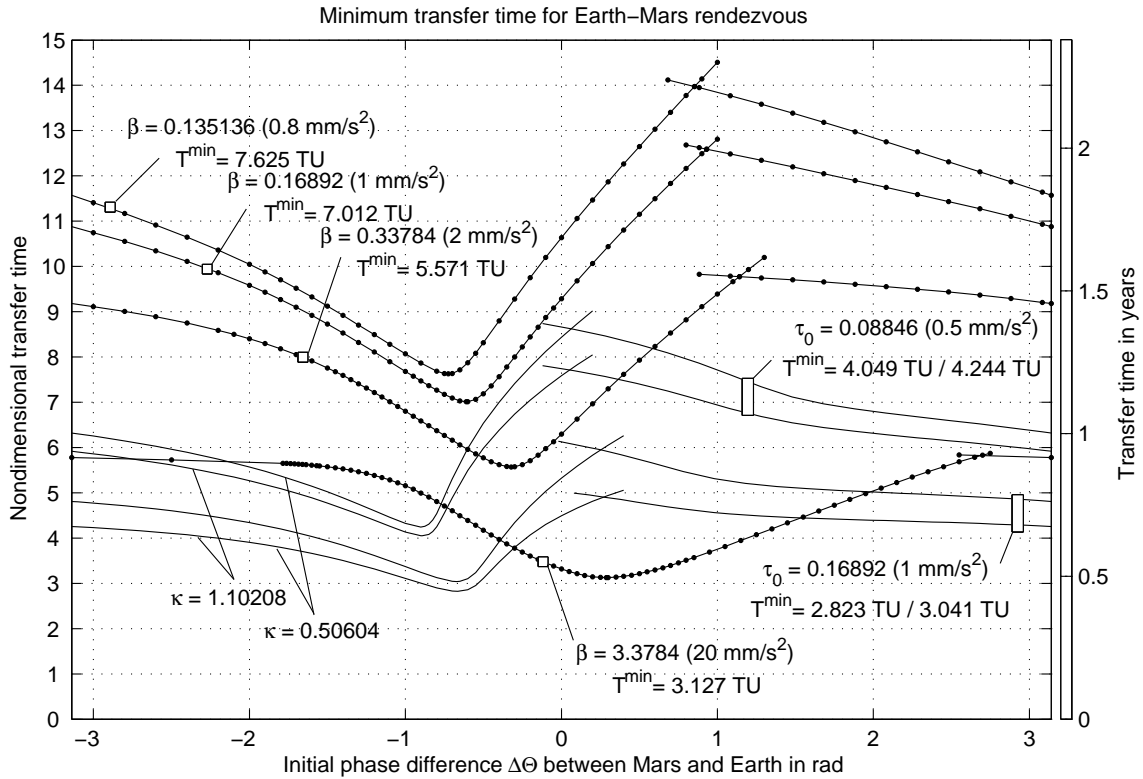


Figure 5.13: Minimum transfer time for Earth-to-Mars rendezvous comparing solar sail spacecraft (solid-dotted lines) and nuclear-electric spacecraft (solid lines).

using solutions for nuclear-electric spacecraft. In doing so the particular choices of coordinate system to describe the system dynamics prove to be essential. On one hand, the most “natural” way to describe solar sail spacecraft in three dimensions is to use a frame of reference based on spherical coordinates. On the other, cartesian coordinates are a logical choice to formulate the system dynamics of nuclear-electric spacecraft. Therefore, the approach we take to solve the minimum-time transfer problem for solar sail spacecraft can be outlined as follows:

- (1) Solve the minimum-time transfer problem for nuclear-electric spacecraft described with cartesian coordinates.
- (2) Transform the solution from cartesian coordinates to spherical coordinates.
- (3) Use homotopy and the solution of nuclear-electric spacecraft in spherical coordinates to compute corresponding solution trajectories for solar sail spacecraft in spherical coordinates.

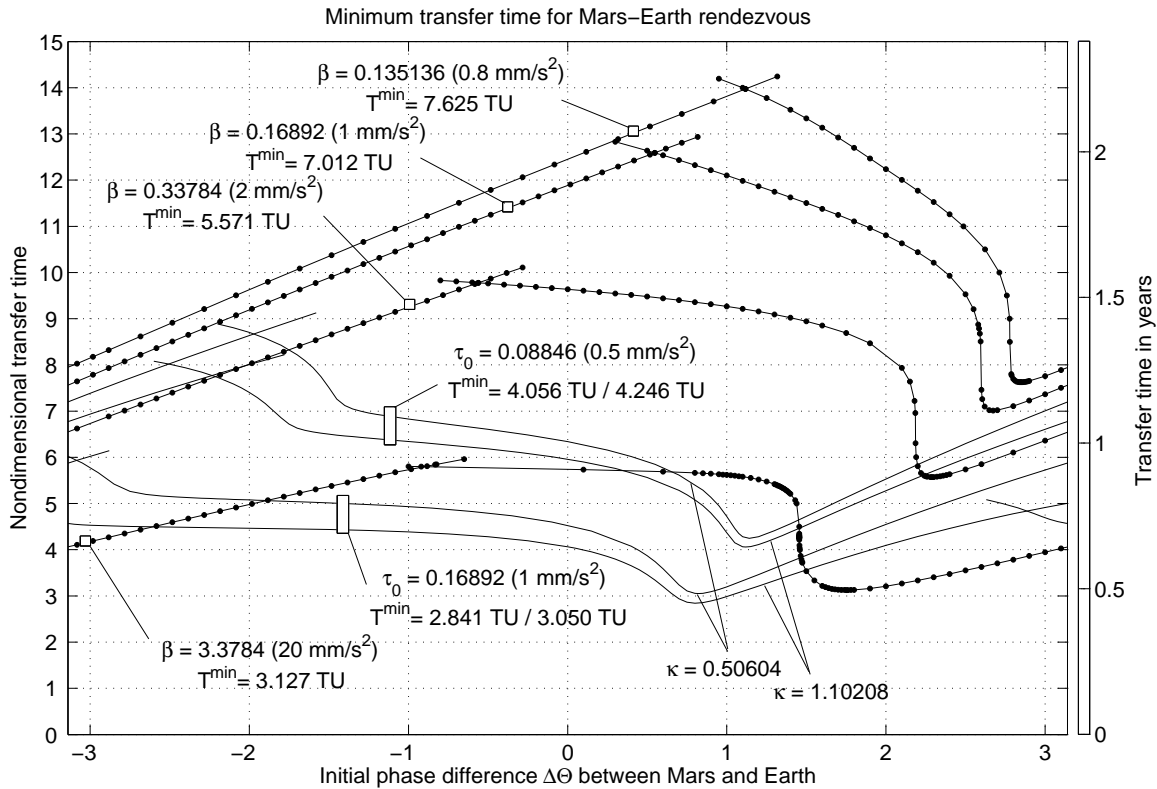


Figure 5.14: Minimum transfer time for Mars-to-Earth rendezvous comparing solar sail spacecraft (solid-dotted lines) and nuclear-electric spacecraft (solid lines).

In the following we formulate the optimal control problem for nuclear-electric spacecraft in cartesian and spherical coordinates and for solar sail spacecraft in spherical coordinates. In Section 5.2.4 we set up the homotopy problem and demonstrate the effectiveness of the approach with a specific example. In the final section we show that the two-dimensional trade studies discussed in Section 5.1 are in good agreement with results obtained for the three-dimensional analysis which serves as the justification to use results from the two-dimensional analysis to study the general physical nature of low-thrust minimum-time transfers.

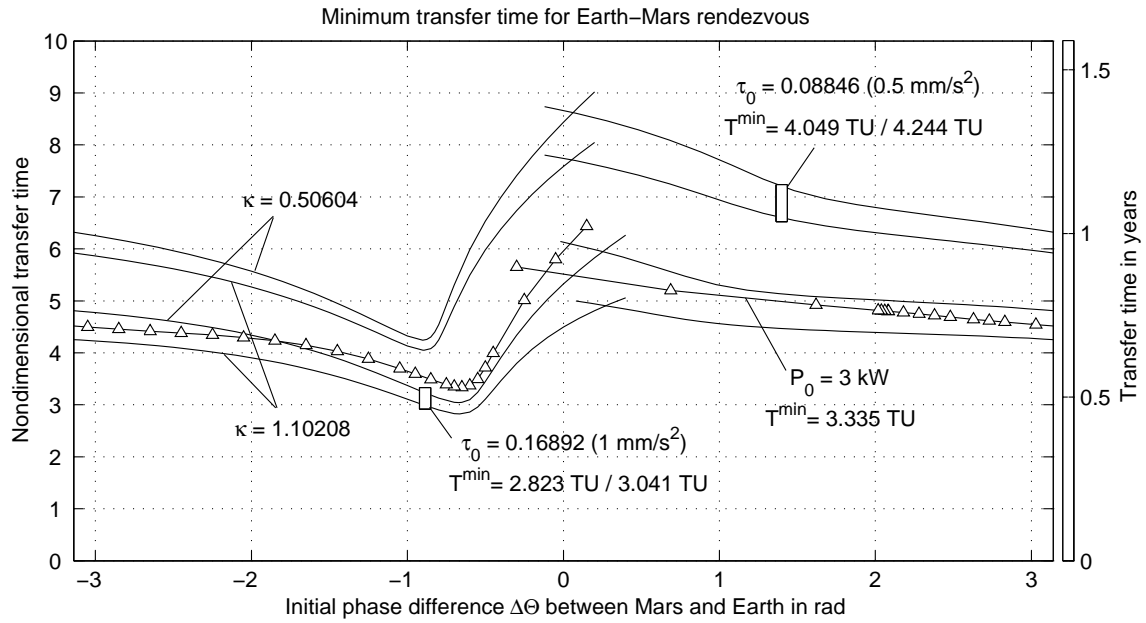


Figure 5.15: Minimum transfer time for Earth-to-Mars rendezvous comparing solar-electric spacecraft (upward-triangle solid lines) and nuclear-electric spacecraft (solid lines).

5.2.1 Nuclear-electric propulsion systems

As demonstrated in Section 5.1 we nondimensionalize motion equations using the algorithm outlined in Appendix B and derive necessary conditions for optimality. We derive optimality conditions for a nuclear-electric spacecraft first in cartesian coordinates and then using a spherical coordinates description.

NEP system in cartesian coordinates

Motion equations for spacecraft with electric propulsion systems can be written as

$$\ddot{x} = -\frac{\mu_{\odot}x}{r^3} + \frac{T}{m} \cos \alpha_z \cos \alpha_{xy} \quad (5.49)$$

$$\ddot{y} = -\frac{\mu_{\odot}y}{r^3} + \frac{T}{m} \cos \alpha_z \sin \alpha_{xy} \quad (5.50)$$

$$\ddot{z} = -\frac{\mu_{\odot}z}{r^3} + \frac{T}{m} \sin \alpha_z \quad (5.51)$$

$$\dot{m} = -c \quad (5.52)$$

As shown in Section 5.1.1 we replace the spacecraft mass by the specific thrust as the state variable to simplify subsequent analysis. The equations of motion can then be written as a first-order, nondimensional system

$$\dot{x} = v_x \quad (5.53)$$

$$\dot{y} = v_y \quad (5.54)$$

$$\dot{z} = v_z \quad (5.55)$$

$$\dot{v}_x = -\frac{x}{r^3} + \tau \cos \alpha_z \cos \alpha_{xy} \quad (5.56)$$

$$\dot{v}_y = -\frac{y}{r^3} + \tau \cos \alpha_z \sin \alpha_{xy} \quad (5.57)$$

$$\dot{v}_z = -\frac{z}{r^3} + \tau \sin \alpha_z \quad (5.58)$$

$$\dot{\tau} = \tau^2 \kappa \quad (5.59)$$

and the corresponding Hamiltonian results

$$\begin{aligned} \mathcal{H} = & \lambda_1 v_x + \lambda_2 v_y + \lambda_3 v_z + \lambda_7 \tau^2 \kappa + \lambda_4 \left(-\frac{x}{r^3} + \tau \cos \alpha_z \cos \alpha_{xy} \right) + \\ & \lambda_5 \left(-\frac{y}{r^3} + \tau \cos \alpha_z \sin \alpha_{xy} \right) + \lambda_6 \left(-\frac{z}{r^3} + \tau \sin \alpha_z \right) \end{aligned} \quad (5.60)$$

The corresponding costate equations are then obtained as $\dot{\boldsymbol{\lambda}} = -\partial \mathcal{H} / \partial \boldsymbol{x}$

$$\dot{\lambda}_1 = \lambda_4 (y^2 + z^2 - 2x^2) / r^5 - 3x(\lambda_5 y + \lambda_6 z) / r^5 \quad (5.61)$$

$$\dot{\lambda}_2 = \lambda_5 (x^2 + z^2 - 2y^2) / r^5 - 3y(\lambda_4 x + \lambda_6 z) / r^5 \quad (5.62)$$

$$\dot{\lambda}_3 = \lambda_6 (y^2 + x^2 - 2z^2) / r^5 - 3z(\lambda_4 x + \lambda_5 y) / r^5 \quad (5.63)$$

$$\dot{\lambda}_4 = -\lambda_1 \quad (5.64)$$

$$\dot{\lambda}_5 = -\lambda_2 \quad (5.65)$$

$$\dot{\lambda}_6 = -\lambda_3 \quad (5.66)$$

$$\dot{\lambda}_7 = -\lambda_4 \cos \alpha_z \cos \alpha_{xy} - \lambda_5 \cos \alpha_z \sin \alpha_{xy} - \lambda_6 \sin \alpha_z - 2\lambda_7 \tau \kappa \quad (5.67)$$

The first derivative of the Hamiltonian with respect to α_z results

$$\frac{\partial \mathcal{H}}{\partial \alpha_z} = 0 = -\lambda_4 \tau \sin \alpha_z \cos \alpha_{xy} - \lambda_5 \tau \sin \alpha_z \sin \alpha_{xy} + \lambda_6 \tau \cos \alpha_z \quad (5.68)$$

which simplifies to

$$\frac{\sin \alpha_z}{\cos \alpha_z} = \frac{\lambda_6}{\lambda_4 \cos \alpha_{xy} + \lambda_5 \sin \alpha_{xy}}, \quad \text{with } \alpha_z \in [-\pi/2, \pi/2] \quad (5.69)$$

Accordingly, the second-order derivative of the Hamiltonian with respect to α_z can be written as

$$\frac{\partial^2 \mathcal{H}}{\partial \alpha_z^2} = -\lambda_4 \tau \cos \alpha_z \cos \alpha_{xy} - \lambda_5 \tau \cos \alpha_z \sin \alpha_{xy} - \lambda_6 \tau \sin \alpha_z > 0 \quad (5.70)$$

or, equivalently

$$(\lambda_4 \cos \alpha_{xy} + \lambda_5 \sin \alpha_{xy}) \cos \alpha_z + \lambda_6 \sin \alpha_z < 0 \quad (5.71)$$

substituting for the costates using equation yields to independent constraints in the form

$$\frac{\lambda_6 \cos^2 \alpha_z}{\sin \alpha_z} + \lambda_6 \sin \alpha_z = \frac{\lambda_6}{\sin \alpha_z} < 0 \quad \rightarrow \quad \text{sign}(\lambda_6) = -\text{sign}(\sin \alpha_z) \quad (5.72)$$

and, similarly,

$$\frac{\lambda_4 \cos \alpha_{xy} + \lambda_5 \sin \alpha_{xy}}{\cos \alpha_z} < 0 \quad \rightarrow \quad \text{sign}(\lambda_4 \cos \alpha_{xy} + \lambda_5 \sin \alpha_{xy}) = -\text{sign}(\cos \alpha_z) \quad (5.73)$$

the corresponding control law for α_z then results

$$\alpha_z^* = \text{atan2} \left(\frac{-\lambda_6}{-(\lambda_4 \cos \alpha_{xy} + \lambda_5 \sin \alpha_{xy})} \right), \quad \text{with } \alpha_z^* \in [-\pi/2, \pi/2] \quad (5.74)$$

For the control angle α_{xy} the first-order derivative of the Hamiltonian results

$$\frac{\partial \mathcal{H}}{\partial \alpha_{xy}} = 0 = -\lambda_4 \tau \cos \alpha_z \sin \alpha_{xy} + \lambda_5 \tau \cos \alpha_z \cos \alpha_{xy} \quad \rightarrow \quad \frac{\sin \alpha_{xy}}{\cos \alpha_{xy}} = \frac{\lambda_5}{\lambda_4} \quad (5.75)$$

the corresponding second-order derivative is obtained as

$$\frac{\partial^2 \mathcal{H}}{\partial \alpha_{xy}^2} = -\lambda_4 \tau \cos \alpha_z \cos \alpha_{xy} - \lambda_5 \tau \cos \alpha_z \sin \alpha_{xy} > 0 \quad (5.76)$$

As we noted earlier $\alpha_z \in [-\pi/2, \pi/2] \rightarrow \cos \alpha_z > 0$. Using equation (5.75) two independent constraints for the control angle α_{xy} can be obtained as

$$\text{sign}(\lambda_5) = -\text{sign}(\sin \alpha_{xy}) \quad \text{and} \quad \text{sign}(\lambda_4) = -\text{sign}(\cos \alpha_{xy}) \quad (5.77)$$

therefore the correct control law for α_{xy} is obtained as

$$\alpha_{xy}^* = \text{atan2} \left(\frac{-\lambda_5}{-\lambda_4} \right), \quad \text{with } \alpha_{xy}^* \in [0, 2\pi) \quad (5.78)$$

Note that mixed second-order derivatives of the Hamiltonian add no additional information.

NEP system in spherical coordinates

Motion equations for spacecraft with electric propulsion systems can be written using spherical coordinates as

$$\ddot{r} = r\dot{\theta}^2 \cos^2 \phi + r\dot{\phi}^2 - \frac{\mu_{\odot}}{r^2} + \frac{T}{m} \cos \alpha_r \quad (5.79)$$

$$\ddot{\theta} = -\frac{2\dot{\theta}\dot{r}}{r} + 2\dot{\theta}\dot{\phi} \tan \phi + \frac{T}{m} \frac{\sin \alpha_r \sin \alpha_{\phi\theta}}{r \cos \phi} \quad (5.80)$$

$$\ddot{\phi} = -\frac{2\dot{\phi}\dot{r}}{r} - \dot{\theta}^2 \sin \phi \cos \phi + \frac{T}{mr} \sin \alpha_r \cos \alpha_{\phi\theta} \quad (5.81)$$

$$\dot{m} = -c \quad (5.82)$$

Again we replace the spacecraft mass m by the specific thrust τ as the new state variable; equations (5.79–5.82) can then be rewritten as a first-order, nondimensional system

$$\dot{r} = v_r \quad (5.83)$$

$$\dot{\theta} = v_{\theta} \quad (5.84)$$

$$\dot{\phi} = v_{\phi} \quad (5.85)$$

$$\dot{v}_r = rv_{\theta}^2 \cos^2 \phi + rv_{\phi}^2 - \frac{1}{r^2} + \tau \cos \alpha_r \quad (5.86)$$

$$\dot{v}_{\theta} = -\frac{2v_{\theta}v_r}{r} + 2v_{\theta}v_{\phi} \tan \phi + \tau \frac{\sin \alpha_r \sin \alpha_{\phi\theta}}{r \cos \phi} \quad (5.87)$$

$$\dot{v}_{\phi} = -\frac{2v_{\phi}v_r}{r} - v_{\theta}^2 \sin \phi \cos \phi + \frac{\tau}{r} \sin \alpha_r \cos \alpha_{\phi\theta} \quad (5.88)$$

$$\dot{\tau} = \tau^2 \kappa \quad (5.89)$$

and the corresponding Hamiltonian results

$$\begin{aligned} \mathcal{H} = & \lambda_1 v_r + \lambda_2 v_{\theta} + \lambda_3 v_{\phi} + \\ & \lambda_4 \left(rv_{\theta}^2 \cos^2 \phi + rv_{\phi}^2 - \frac{1}{r^2} + \tau \cos \alpha_r \right) + \\ & \lambda_5 \left(-\frac{2v_{\theta}v_r}{r} + 2v_{\theta}v_{\phi} \tan \phi + \tau \frac{\sin \alpha_r \sin \alpha_{\phi\theta}}{r \cos \phi} \right) + \\ & \lambda_6 \left(-\frac{2v_{\phi}v_r}{r} - v_{\theta}^2 \sin \phi \cos \phi + \frac{\tau}{r} \sin \alpha_r \cos \alpha_{\phi\theta} \right) + \lambda_7 \tau^2 \kappa \end{aligned} \quad (5.90)$$

The corresponding costate equations are then obtained as $\dot{\lambda} = -\partial\mathcal{H}/\partial\mathbf{x}$

$$\dot{\lambda}_1 = -\lambda_4 (v_\theta^2 \cos^2 \phi + v_\phi^2 + 2/r^3) + \lambda_5 \left(\frac{-2v_\theta v_r}{r^2} + \tau \frac{\sin \alpha_r \sin \alpha_{\phi\theta}}{r^2 \cos \phi} \right) + \quad (5.91)$$

$$\lambda_6 (-2v_\phi v_r/r^2 + \tau \sin \alpha_r \cos \alpha_{\phi\theta}/r^2)$$

$$\lambda_2 = \text{const.} \begin{cases} = 0 & \text{iff } \theta(t_f) = \text{free} \\ \neq 0 & \text{iff } \theta(t_f) = \theta_f \end{cases} \quad (5.92)$$

$$\dot{\lambda}_3 = \lambda_4 r v_\theta^2 \sin(2\phi) - \lambda_5 \left(\frac{2v_\theta v_\phi}{\cos^2 \phi} + \tau \frac{\sin \alpha_r \sin \alpha_{\phi\theta} \sin \phi}{r \cos^2 \phi} \right) + \lambda_6 v_\theta^2 \cos(2\phi) \quad (5.93)$$

$$\dot{\lambda}_4 = -\lambda_1 + 2\lambda_5 v_\theta/r + 2\lambda_6 v_\phi/r \quad (5.94)$$

$$\dot{\lambda}_5 = -\lambda_2 - 2\lambda_4 r v_\theta \cos^2 \phi + 2\lambda_5 (v_r/r - v_\phi \tan \phi) + \lambda_6 v_\theta \sin(2\phi) \quad (5.95)$$

$$\dot{\lambda}_6 = -\lambda_3 - 2\lambda_4 r v_\phi - 2\lambda_5 v_\theta \tan \phi + 2\lambda_6 v_r/r \quad (5.96)$$

$$\dot{\lambda}_7 = -\lambda_4 \cos \alpha_r - \lambda_5 \frac{\sin \alpha_r \sin \alpha_{\phi\theta}}{r \cos \phi} - \lambda_6 \sin \alpha_r \cos \alpha_{\phi\theta}/r - 2\lambda_7 \tau \kappa \quad (5.97)$$

Pontryagin's necessary conditions yield

$$\frac{\partial\mathcal{H}}{\partial\alpha_{\phi\theta}} = 0 = \lambda_5 \frac{\tau \sin \alpha_r \cos \alpha_{\phi\theta}}{r \cos \phi} - \lambda_6 \frac{\tau}{r} \sin \alpha_r \sin \alpha_{\phi\theta} \rightarrow \frac{\sin \alpha_{\phi\theta}}{\cos \alpha_{\phi\theta}} = \frac{\lambda_5}{\lambda_6 \cos \phi} \quad (5.98)$$

which can be used to deduce directly the control law for the control angle $\alpha_{\phi\theta}$. The second derivative of the Hamiltonian with respect to the clock angle yields

$$\frac{\partial^2\mathcal{H}}{\partial\alpha_{\phi\theta}^2} = -\lambda_5 \frac{\tau \sin \alpha_r \sin \alpha_{\phi\theta}}{r \cos \phi} - \lambda_6 \frac{\tau}{r} \sin \alpha_r \cos \alpha_{\phi\theta} > 0 \quad (5.99)$$

By construction, the cone angle $\alpha_r \geq 0$, that is, $\alpha_r \in [0, \pi]$, and therefore $\sin \alpha_r \geq 0$, which simplifies condition (5.99) to

$$\lambda_5 \frac{\sin \alpha_{\phi\theta}}{\cos \phi} + \lambda_6 \cos \alpha_{\phi\theta} < 0 \quad (5.100)$$

Substituting for λ_5 and λ_6 in condition (5.100) using equation (5.98) yields two independent constraints on the clock angle:

$$\lambda_5 \frac{\sin \alpha_{\phi\theta}}{\cos \phi} + \lambda_5 \frac{\cos^2 \alpha_{\phi\theta}}{\sin \alpha_{\phi\theta} \cos \phi} = \frac{\lambda_5}{\sin \alpha_{\phi\theta} \cos \phi} < 0 \rightarrow \text{sign}(\lambda_5) = -\text{sign}(\sin \alpha_{\phi\theta}) \quad (5.101)$$

since $\phi \in [-\pi/2, \pi/2]$, and accordingly

$$\frac{\lambda_6}{\cos \alpha_{\phi\theta}} < 0 \rightarrow \text{sign}(\lambda_6) = -\text{sign}(\cos \alpha_{\phi\theta}) \quad (5.102)$$

The correct control law for the clock angle is then obtained from equation (5.98) as

$$\alpha_{\phi\theta}^* = \text{atan2}\left(\frac{-\lambda_5}{-\lambda_6 \cos \phi}\right), \quad \text{with } \alpha_{\phi\theta}^* \in [0, 2\pi) \quad (5.103)$$

The first derivative of the Hamiltonian with respect to the cone angle α_r results

$$\frac{\partial \mathcal{H}}{\partial \alpha_r} = 0 = -\lambda_4 \tau \sin \alpha_r + \lambda_5 \frac{\tau \cos \alpha_r \sin \alpha_{\phi\theta}}{r \cos \phi} + \lambda_6 \frac{\tau}{r} \cos \alpha_r \cos \alpha_{\phi\theta} \quad (5.104)$$

and therefore

$$\frac{\sin \alpha_r}{\cos \alpha_r} = \frac{\lambda_5 \sin \alpha_{\phi\theta} + \lambda_6 r \cos \alpha_{\phi\theta} \cos \phi}{\lambda_4 r \cos \phi} \quad (5.105)$$

which can be used to deduce directly the control law for the control angle $\alpha_{\phi\theta}$. To remove quadrant ambiguities we obtain information from the second derivative of the Hamiltonian with respect to the clock angle

$$\frac{\partial^2 \mathcal{H}}{\partial \alpha_r^2} = -\lambda_4 \tau \cos \alpha_r - \lambda_5 \frac{\tau \sin \alpha_r \sin \alpha_{\phi\theta}}{r \cos \phi} - \lambda_6 \frac{\tau}{r} \sin \alpha_r \cos \alpha_{\phi\theta} > 0 \quad (5.106)$$

With the help of equation (5.105) we can deduce two independent constraints

$$\sin \alpha_r > 0 \Leftrightarrow \alpha_r \in [0, \pi] \quad \text{and} \quad \text{sign}(\lambda_4) = -\text{sign}(\cos \alpha_r) \quad (5.107)$$

Note that with conditions (5.100) the numerator on the right-hand side in equation (5.105) is negative and so the correct control law for the cone angle yields

$$\alpha_r^* = \text{atan}\left(\frac{\lambda_5 \sin \alpha_{\phi\theta} + \lambda_6 \cos \phi \cos \alpha_{\phi\theta}}{\lambda_4 r \cos \phi}\right), \quad \text{with } \alpha_r^* \in [0, \pi] \quad (5.108)$$

For completeness we note that mixed second-order derivatives of the Hamiltonian with respect to the control angles $\partial^2 \mathcal{H} / (\partial \alpha_r \partial \alpha_{\phi\theta}) = 0$ and therefore do not yield any additional information.

5.2.2 Solar sail spacecraft

Non-dimensional motion equations for solar sail spacecraft can be written as

$$\dot{r} = v_r \quad (5.109)$$

$$\dot{\theta} = v_\theta \quad (5.110)$$

$$\dot{\phi} = v_\phi \quad (5.111)$$

$$\dot{v}_r = r v_\theta^2 \cos^2 \phi + r v_\phi^2 - \frac{1}{r^2} + \frac{\beta}{r^2} \cos^3 \alpha_r \quad (5.112)$$

$$\dot{v}_\theta = -\frac{2v_\theta v_r}{r} + 2v_\theta v_\phi \tan \phi + \frac{\beta \cos^2 \alpha_r \sin \alpha_r \sin \alpha_{\phi\theta}}{r^3 \cos \phi} \quad (5.113)$$

$$\dot{v}_\phi = -\frac{2v_\phi v_r}{r} - v_\theta^2 \sin \phi \cos \phi + \frac{\beta}{r^3} \cos^2 \alpha_r \sin \alpha_r \cos \alpha_{\phi\theta} \quad (5.114)$$

and the corresponding Hamiltonian results

$$\begin{aligned}
\mathcal{H} &= \lambda_1 v_r + \lambda_2 v_\theta + \lambda_3 v_\phi + \\
&\lambda_4 \left(r v_\theta^2 \cos^2 \phi + r v_\phi^2 - \frac{1}{r^2} + \frac{\beta}{r^2} \cos^3 \alpha_r \right) + \\
&\lambda_5 \left(-\frac{2v_\theta v_r}{r} + 2v_\theta v_\phi \tan \phi + \frac{\beta \cos^2 \alpha_r \sin \alpha_r \sin \alpha_{\phi\theta}}{r^3 \cos \phi} \right) + \\
&\lambda_6 \left(-\frac{2v_\phi v_r}{r} - v_\theta^2 \sin \phi \cos \phi + \frac{\beta}{r^3} \cos^2 \alpha_r \sin \alpha_r \cos \alpha_{\phi\theta} \right)
\end{aligned} \tag{5.115}$$

Then the costate equations result

$$\begin{aligned}
\dot{\lambda}_1 &= -\lambda_4 (v_\theta^2 \cos^2 \phi + v_\phi^2 + 2/r^3 - 2\beta \cos^3 \alpha_r / r^3) + \\
&\lambda_5 \left(\frac{-2v_\theta v_r}{r^2} + \frac{3\beta \cos^2 \alpha_r \sin \alpha_r \sin \alpha_{\phi\theta}}{r^4 \cos \phi} \right) + \\
&\lambda_6 \left(\frac{-2v_\phi v_r}{r^2} + \frac{3\beta}{r^4} \cos^2 \alpha_r \sin \alpha_r \cos \alpha_{\phi\theta} \right)
\end{aligned} \tag{5.116}$$

$$\lambda_2 = \text{const.} \begin{cases} = 0 & \text{iff } \theta(t_f) = \text{free} \\ \neq 0 & \text{iff } \theta(t_f) = \theta_f \end{cases} \tag{5.117}$$

$$\dot{\lambda}_3 = \lambda_4 r v_\theta^2 \sin(2\phi) - \lambda_5 \left(\frac{2v_\theta v_\phi}{\cos^2 \phi} + \frac{\beta \cos^2 \alpha_r \sin \alpha_r \sin \alpha_{\phi\theta} \sin \phi}{r^3 r \cos^2 \phi} \right) + \lambda_6 v_\theta^2 \cos(2\phi) \tag{5.118}$$

$$\dot{\lambda}_4 = -\lambda_1 + 2\lambda_5 v_\theta / r + 2\lambda_6 v_\phi / r \tag{5.119}$$

$$\dot{\lambda}_5 = -\lambda_2 - 2\lambda_4 r v_\theta \cos^2 \phi + 2\lambda_5 (v_r / r - v_\phi \tan \phi) + \lambda_6 v_\theta \sin(2\phi) \tag{5.120}$$

$$\dot{\lambda}_6 = -\lambda_3 - 2\lambda_4 r v_\phi - 2\lambda_5 v_\theta \tan \phi + 2\lambda_6 v_r / r \tag{5.121}$$

Let us first derive the control law for the clock angle $\alpha_{\phi\theta}$. The first derivative of the Hamiltonian with respect to the clock angle results

$$\frac{\partial \mathcal{H}}{\partial \alpha_{\phi\theta}} = \lambda_5 \frac{\beta \cos^2 \alpha_r \sin \alpha_r \cos \alpha_{\phi\theta}}{r^3 \cos \phi} - \lambda_6 \frac{\beta}{r^3} \cos^2 \alpha_r \sin \alpha_r \sin \alpha_{\phi\theta} = 0 \tag{5.122}$$

and therefore

$$\frac{\sin \alpha_{\phi\theta}}{\cos \alpha_{\phi\theta}} = \frac{\lambda_5}{\lambda_6 \cos \phi} \tag{5.123}$$

which can be used to deduce directly the control law for the control angle $\alpha_{\phi\theta}$. To remove quadrant ambiguities we use the second derivative of the Hamiltonian with respect to the clock angle. Since $\phi \in [-\pi/2, \pi/2]$ the corresponding conditions yield

$$\text{sign}(\lambda_6) = -\text{sign}(\cos \alpha_{\phi\theta}) \quad \text{and} \quad \text{sign}(\lambda_5) = -\text{sign}(\sin \alpha_{\phi\theta}) \tag{5.124}$$

Therefore the correct control law for the clock angle can be written as

$$\alpha_{\phi\theta}^* = \text{atan2} \left(\frac{-\lambda_5}{-\lambda_6 \cos \phi} \right), \quad \text{with} \quad \alpha_{\phi\theta}^* \in [0, 2\pi] \quad (5.125)$$

A similar analysis yields the control law for the cone angle. It is straightforward to show that the first derivative of \mathcal{H} with respect to α_r results

$$\begin{aligned} \frac{\partial \mathcal{H}}{\partial \alpha_r} = & -3\lambda_4 \frac{\beta}{r^2} \cos^2 \alpha_r \sin \alpha_r + \\ & \left(\lambda_5 \frac{\sin \alpha_{\phi\theta}}{\cos \phi} + \lambda_6 \cos \alpha_{\phi\theta} \right) \frac{\beta}{r^3} (\cos^3 \alpha_r - 2 \cos \alpha_r \sin^2 \alpha_r) \end{aligned} \quad (5.126)$$

By dividing through the common factor $\beta \cos^3 \alpha_r / r^2$ in equation (5.126) we end up with a quadratic equation in $\tan \alpha_r$ which yields

$$\tan \alpha_r^* = -a \pm \sqrt{a^2 + 1/2}, \quad \text{where} \quad a = \frac{(3/4)\lambda_4 r \cos \phi}{\lambda_5 \sin \alpha_{\phi\theta} + \lambda_6 \cos \alpha_{\phi\theta} \cos \phi} \quad (5.127)$$

Rather than using the second-order derivative of the Hamiltonian to choose the correct sign (\pm) for the control law, we give physical and geometrical arguments to obtain the correct control law. Note that irrespective of the sign of a , the plus sign in equation (5.127) causes $\tan \alpha_r > 0$ whereas with the minus sign, $\tan \alpha_r < 0$. Since the cone angle is by definition positive ($\alpha_r > 0$) it follows that $\alpha_r \in [0, \pi]$ such that the solar sail normal vector is uniquely determined with $\alpha_{\phi\theta} \in [0, 2\pi]$. Therefore, choosing the sign in equation (5.127) is tantamount to choosing between the first and second quadrant for the cone angle. From equation (5.112) we see that $\dot{v}_r(\alpha_r) \propto \cos^3 \alpha_r \rightarrow \text{sign}(\dot{v}_r(\alpha_r)) = \text{sign}(\cos \alpha_r)$. For the case where $\alpha_r = \pi$, $\dot{v}_r(\alpha_r) < 0$ which clearly violates Newton's 2nd law.¹⁰ As a result, $\alpha_r \in [0, \pi/2]$ and the corresponding control law is obtained as

$$\alpha_r^* = \text{atan} \left(-a + \sqrt{a^2 + 1/2} \right), \quad \text{with} \quad \alpha_r^* \in [0, \pi/2] \quad (5.128)$$

and where

$$a = \frac{(3/4)\lambda_4 r \cos \phi}{\lambda_5 \sin \alpha_{\phi\theta} + \lambda_6 \cos \alpha_{\phi\theta} \cos \phi} \quad (5.129)$$

Having derived the motion equations for nuclear-electric and solar sail spacecraft we now proceed to discussing coordinate transformations of optimal control solution trajectories.

¹⁰ Mutationem motus proportionalem esse vi motrici impressae, et fieri secundum lineam rectam qua vis illa imprimitur⁶⁶ – The alteration of motion is ever proportional to the motive force impressed; and is made in the direction of the right line in which that force is impressed.

5.2.3 Coordinate transformation of solution trajectories

Minimum-time solutions for nuclear-electric spacecraft in cartesian coordinates are readily obtained using the optimization algorithm introduced in Chapter 3. In order to be able to formulate the homotopy problem to solve for solutions for solar sail spacecraft we need a solution trajectory for nuclear-electric spacecraft in spherical coordinates. In the following we briefly outline how to use information of the available transfer trajectory in one coordinate system to obtain a reduced-order optimization problem in the desired coordinate system.

First note that the relationship between the control angles vectors in cartesian and spherical coordinates is given by (see Figure 4.2)

$$\mathbf{u}_{\text{spher}} = \mathbf{C}_2(-\phi)\mathbf{C}_3(\theta)\mathbf{u}_{\text{cart}} \quad (5.130)$$

where

$$\mathbf{u}_{\text{spher}} = \begin{pmatrix} \cos \alpha_r \\ \sin \alpha_r \sin \alpha_{\phi\theta} \\ \sin \alpha_r \cos \alpha_{\phi\theta} \end{pmatrix} \quad \text{and} \quad \mathbf{u}_{\text{cart}} = \begin{pmatrix} \cos \alpha_z \cos \alpha_{xy} \\ \cos \alpha_z \sin \alpha_{xy} \\ \sin \alpha_z \end{pmatrix} \quad (5.131)$$

and where \mathbf{C}_i is the single-rotation matrix about the i th axis. For a given set of initial conditions for the trajectory described in cartesian coordinates we can therefore compute the corresponding initial control angles $\alpha_r(t_0)$ and $\alpha_{\phi\theta}(t_0)$ using equations (5.130,5.131). We can then use the expressions for the optimal control angles in equations (5.103,5.108) to calculate initial conditions for two costates and by doing so reduce the dimensionality of the resulting optimization problem. For the subsequent analysis we use boundary conditions and corresponding sets of initial control angles in cartesian and spherical coordinates for a typical Earth-to-Mars minimum-time transfer as listed in Table 5.2.

For the sake of convenience we restate the optimal control laws for the clock and the cone angles. The optimal clock angle yields

$$\alpha_{\phi\theta}^* = \text{atan2} \left(\frac{-\lambda_5}{-\lambda_6 \cos \phi} \right), \quad \text{with} \quad \alpha_{\phi\theta}^* \in [0, 2\pi) \quad (5.132)$$

The optimal control law for the cone angle results in

$$\alpha_r^* = \text{atan} \left(\frac{\lambda_5 \sin \alpha_{\phi\theta} + \lambda_6 \cos \phi \cos \alpha_{\phi\theta}}{\lambda_4 r \cos \phi} \right), \quad \text{with} \quad \alpha_r^* \in [0, \pi] \quad (5.133)$$

We first note that for the data set given in Table 5.2 $\cos \phi(t_0) > 0$. Therefore $\lambda_5(t_0) < 0$ and $\lambda_6(t_0) > 0$ in control law (5.103) to obtain an initial control angle $\alpha_{\phi\theta}^*(t_0)$ located in

Table 5.2: Partial transformation of initial condition of costate vector using control angles.

| $\mathbf{x}_{\text{cart}}(t_0)$ | $\mathbf{x}_{\text{cart}}(t_f)$ | $\boldsymbol{\lambda}_{\text{cart}}(t_0)$ | $\mathbf{u}_{\text{cart}}^*(t_0) =$ $(\alpha_z^*, \alpha_{xy}^*)^\top$ | $\mathbf{u}_{\text{spher}}^*(t_0) =$ $(\alpha_r^*, \alpha_{\phi\theta}^*)^\top$ | $\boldsymbol{\lambda}_{\text{spher}}(t_0)$ |
|--|--|--|---|--|--|
| $\begin{pmatrix} +1.0000 \\ +0.0167 \\ +0.0000 \\ -0.1965 \\ +1.7967 \\ +1.7534 \end{pmatrix}$ | $\begin{pmatrix} +0.8069 \\ -1.2554 \\ -0.0461 \\ +0.6514 \\ +0.5086 \\ -0.0053 \end{pmatrix}$ | $\begin{pmatrix} -1.0000 \\ -0.4401 \\ +0.9031 \\ +0.0206 \\ +0.1000 \\ +0.0494 \end{pmatrix}$ | $\begin{pmatrix} -0.0491 \\ -1.6704 \end{pmatrix}$ | $\begin{pmatrix} +1.2594 \\ +1.6224 \end{pmatrix}$ | $\begin{pmatrix} -1.0000 \\ -0.3186 \\ +0.0136 \\ -0.1961 \\ -0.6103 \\ +0.0315 \end{pmatrix}$ |

the second quadrant. Also note that $\sin \alpha_{\phi\theta}^*(t_0) > 0$ and $\cos \alpha_{\phi\theta}^*(t_0) < 0$ which renders the numerator in equation (5.108) to be negative. As a result we need the denominator to be negative to obtain an angle in the first quadrant; thus $\lambda_4(t_0) < 0$. With scaling freedom we can therefore choose $\lambda_5(t_0) = -1$ and use equation (5.103) to compute $\lambda_6(t_0)$. The costate $\lambda_4(t_0)$ is then readily available using equation (5.108). Note that we have normalized the resulting costate vector $\boldsymbol{\lambda}_{\text{spher}}(t_0)$ to match the normalization used for the corresponding costate vector in cartesian coordinates $\boldsymbol{\lambda}_{\text{cart}}(t_0)$.

We note that the reduction in dimensionality of the optimization problem significantly simplifies the solution finding process. Nevertheless, a more in-depth study of transformation theory would be worthwhile and could potentially result in a theory for the algebraic transformation of the entire costate vector.

5.2.4 Defining a homotopy problem

In the previous section we demonstrated how to compute solution trajectories for a nuclear-electric spacecraft in spherical coordinates using the corresponding solution in cartesian coordinates. We can now use this solution to define a homotopy problem and solve for minimum-time trajectories for a solar sail spacecraft.

For the sake of discussion we introduce some notation to distinguish between different sets of motion equations. Let

$$\dot{\mathbf{x}} = \mathbf{f}_\gamma(\mathbf{x}, t), \quad \Psi_\gamma(\mathbf{x}(t_0), \mathbf{x}(t_f), t_0, t_f) = \mathbf{0} \quad (5.134)$$

where

$$\mathbf{x} = \begin{pmatrix} \mathbf{x} \\ \boldsymbol{\lambda} \end{pmatrix}, \quad \text{and} \quad \mathbf{f}_\gamma(\mathbf{x}, t) = \begin{pmatrix} \mathbf{f}_\gamma(\mathbf{x}, \boldsymbol{\lambda}, \mathbf{u}_\gamma^*, t) \\ \mathbf{g}_\gamma(\mathbf{x}, \boldsymbol{\lambda}, \mathbf{u}_\gamma^*, t) \end{pmatrix} \quad (5.135)$$

define the state and costate differential equations of a solar sail spacecraft and let

$$\Psi_\gamma(\mathbf{x}(t_0), t_0, t_f) = \Psi_\gamma(\mathbf{x}(t_0), \mathbf{x}(t_f), t_0, t_f) \quad (5.136)$$

describe the given boundary conditions. Similarly, we use the subscript τ to denote a nuclear-electric spacecraft system model, that is:

$$\dot{\mathbf{x}} = \mathbf{f}_\tau(\mathbf{x}, t), \quad \Psi_\tau(\mathbf{x}(t_0), \mathbf{x}(t_f), t_0, t_f) = \mathbf{0} \quad (5.137)$$

An appropriate homotopy problem is then defined by setting

$$\mathbf{h}(\mathbf{x}, \sigma, t) \triangleq \dot{\mathbf{x}}_h = \mathbf{f}_\tau(\mathbf{x}, t) + \sigma(\mathbf{f}_\gamma(\mathbf{x}, t) - \mathbf{f}_\tau(\mathbf{x}, t)), \quad \Psi_h = \Psi_\tau \equiv \Psi_\gamma \quad (5.138)$$

Note that by setting $\sigma = 0$ the homotopy problem degenerates to the problem with the known solution, whereas for $\sigma = 1$ the homotopy problem reduces to the problem with the desired solution. Also note that the boundary conditions are fixed.

Figure 5.16 shows the result of a homotopy problem computing a minimum-time trajectory for a solar sail spacecraft by using the corresponding solution trajectory of a nuclear-electric spacecraft. Figure 5.17 illustrates the development of the continuation parameter as a function of iteration step for the homotopy problem shown in Figure 5.16. We employed a variable step size algorithm for the continuation parameter that generates a near-optimal sequence of σ_i with guaranteed, rapid convergence. For the homotopy problem shown in Figure 5.16 the algorithm converged within 25 iteration steps with typically less than four iterations necessary to solve the individual homotopy sub-problems for each σ_i .

5.2.5 Results and propulsion system performance comparison

We employ classical orbital elements on the user side of the optimization code to define boundary conditions. Appropriate mappings (Appendix C) transform the boundary conditions into a cartesian (spherical) coordinate description to integrate motion equations.

Figure 5.18 shows a sequence of three-dimensional minimum-time Earth-to-Mars rendezvous for a nuclear-electric spacecraft with $\kappa = 0.50604$ and initial thrust of $\tau_0 = 0.16892$ using J2000 data and varying initial true anomaly offsets of Mars $\Delta\Theta_m$ as measured from the J2000 reference location. Note that we use a different scale for the z -axes

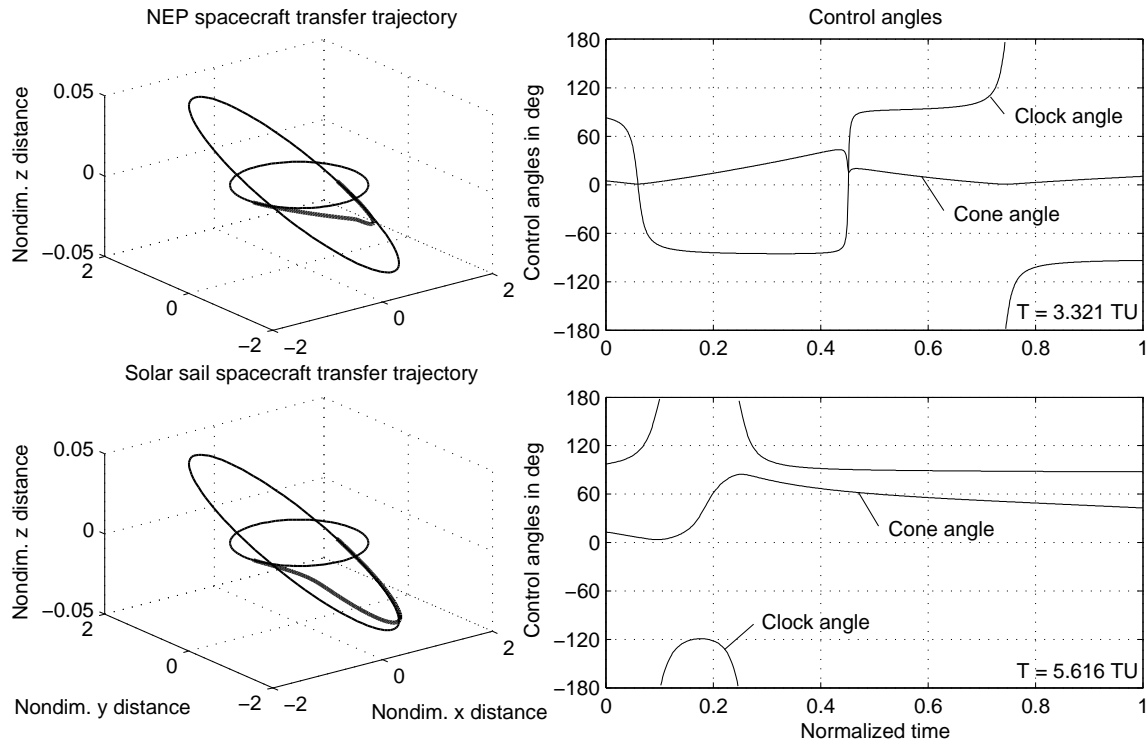


Figure 5.16: Earth-to-Mars transfer trajectory and control angle histories for a solar sail spacecraft obtained from the corresponding transfer solution of a nuclear-electric spacecraft and using homotopy.

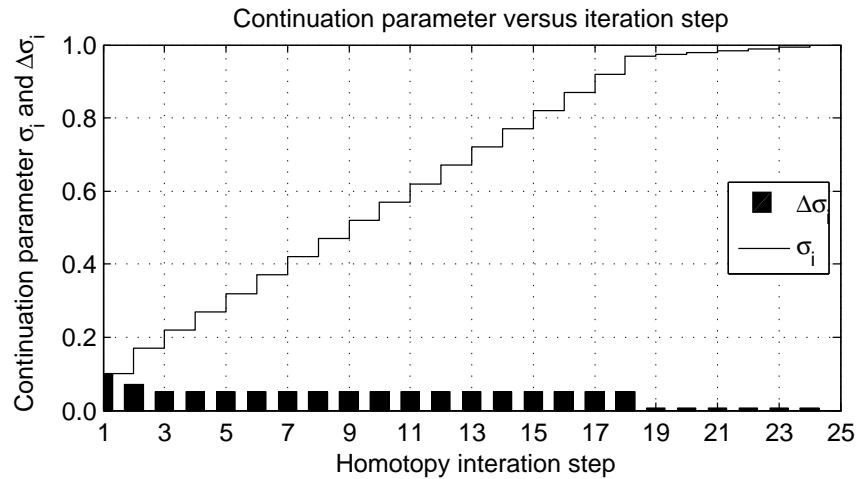


Figure 5.17: Continuation parameter σ_i and continuation parameter step size $\Delta\sigma_i$ as a function of homotopy iteration step for the homotopy problem illustrated in Figure 5.16.

to better visualize the geometry of transfers. Analogous to transfers in two dimensions we identify catch-mode and sleep-mode solution trajectories. Minimum transfer time as a function of initial true anomaly offset of Mars $\Delta\Theta_m$ as measured from the J2000 reference location is illustrated in Figure 5.19 for $\kappa = 0.50604$ and for $\tau_0 = 0.16892$ and $\tau_0 = 0.33784$, respectively. Similar to the trade studies discussed in Section 5.1.5 we identify the two solution branches that correspond to catch-mode and sleep-mode solution trajectories. The figure also shows that the two-dimensional analysis for coplanar, circular planetary orbits compares well to the general three-dimensional analysis. In fact, the solid line representing 2D minimum-time transfers lies “close” to the corresponding curve (downward-triangle solid line) for a wide range of initial true anomaly differences. Therefore, trade studies presented in Section 5.1.5 can indeed be used to analyze the general minimum-time transfer problem, at least for “small” values in eccentricity and inclination of initial and target planet orbits (as is the case, for example, for Earth and Mars orbits).

5.3 Summary

In this chapter we have analyzed the minimum-time transfer problem of low-thrust spacecraft in two and three dimensions. We have demonstrated how to implement symmetry and homotopy methods to efficiently generate optimal control solutions. In the following chapter we discuss various extensions to the system models used in this chapter by employing a rigid-body representation for the spacecraft.

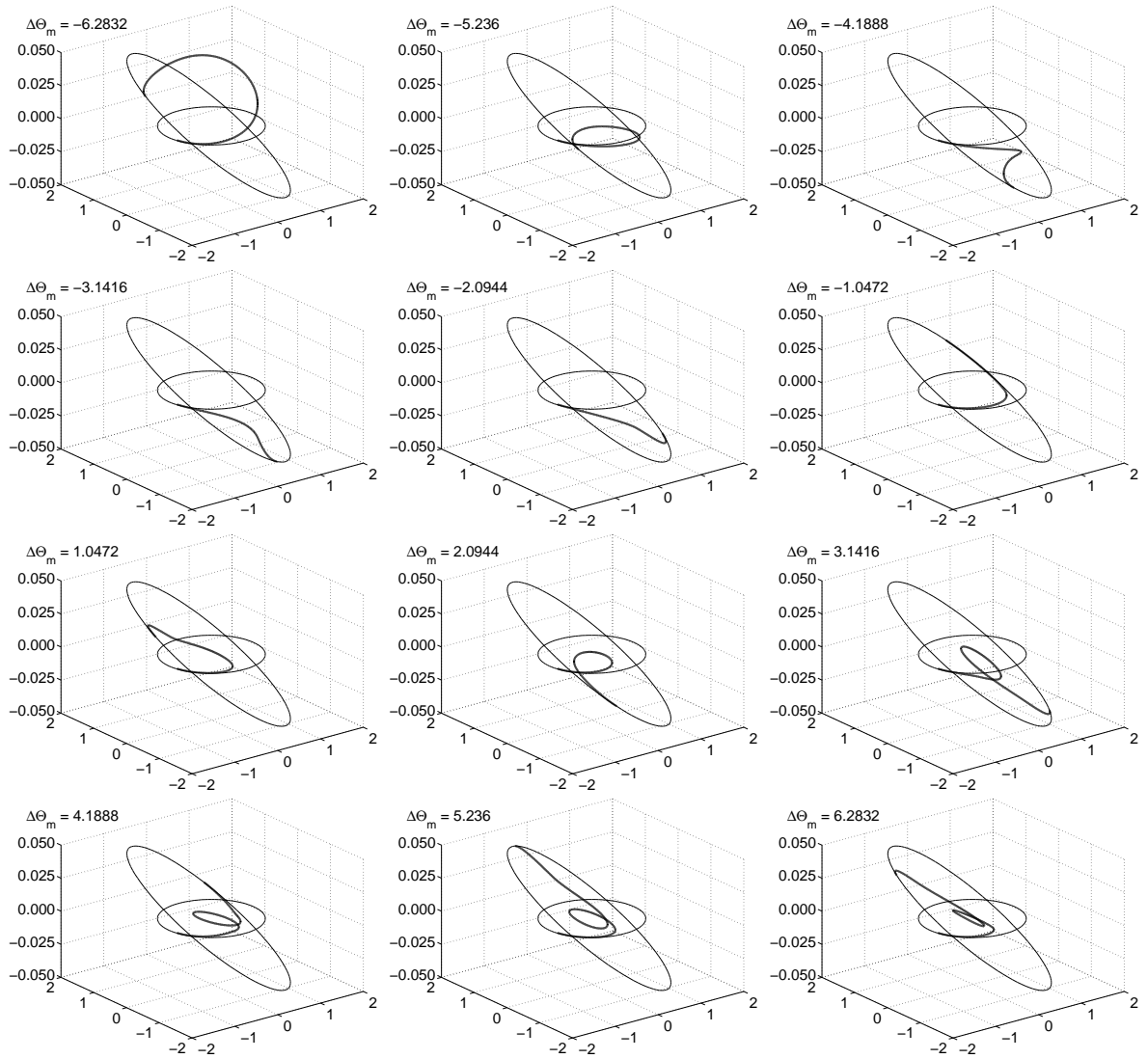


Figure 5.18: 3D Minimum-time Earth-to-Mars rendezvous for $\kappa = 0.50604$ and initial thrust of $\tau_0 = 0.16892$ for varying initial Earth-Mars constellations.

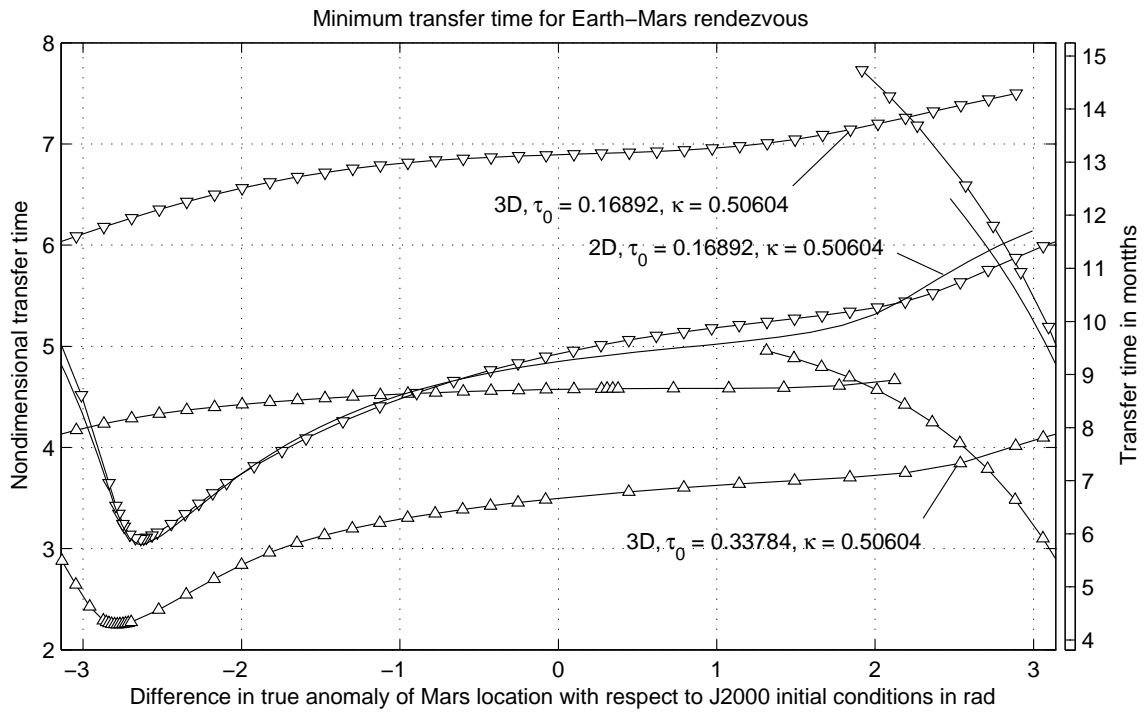


Figure 5.19: Minimum transfer time for 3D Earth-to-Mars rendezvous for $\kappa = 0.50604$ and initial thrust of $\tau_0 = 0.16892$ (downward triangle solid lines) and $\tau_0 = 0.33784$ (upward triangle solid lines). The solid line corresponds to planar transfers for $\tau_0 = 0.16892, \kappa = 0.50604$.

Work in Progress and Future Challenges

This chapter documents current research efforts and lays out the framework for future work in the field of low-thrust minimum-time trajectory optimization. In Chapter 5 we have discussed optimal control problems based on the Two-Body system of Sun and spacecraft and modeling both bodies as point masses. The first part of this chapter is devoted to analyzing the minimum-time transfer problem using a more complex system description by taking into account the attitude dynamics of the spacecraft. We discuss spacecraft design aspects of both solar sail and nuclear-electric spacecraft in Section 6.2 and derive optimality conditions for both system models in Section 6.4 and Section 6.5, respectively. We show exemplary simulation results for both spacecraft systems and briefly outline potential directions for future work.

6.1 Integrating Satellite Attitude Dynamics

In Chapter 5 we analyzed optimal control problems modeling the Sun and spacecraft as point masses. Considering the distance scales involved for interplanetary transfers the point mass assumption is well-justified. Nevertheless, from an engineering perspective the following questions are of interest:

- (1) What are feasible approaches to practically control the attitude of solar sail spacecraft?

- (2) Of all feasible approaches what is the best way to implement a control system that could potentially achieve control angle profiles similar to those obtained via optimal control analysis in Chapter 5?
- (3) Is thrust vectoring a feasible approach to perform interplanetary minimum-time transfers for continuous low-thrust electric spacecraft?

Answering these questions requires the analyses of more complex system models employing, for example, rigid-body representations for spacecraft. In this section we introduce several spacecraft design and control concepts for solar sail and electric spacecraft and discuss implications on optimal control analysis.

6.2 Control system design considerations

One of the most important aspects of formulating an optimal control problem is choosing a particular set of control variables. An imprudent decision in that respect can lead overly complicated and even ill-posed problem statements.

For electric spacecraft thrust vectoring presents a feasible control strategy that offers significant operational and analytical benefits over other control concepts. First, only a single thruster is required (in theory at least) for both attitude and orbital control reducing the system complexity to a minimum. Second, assuming constant, continuous thrust the thrust vector angle is the effective control variable of the system. With this particular choice of control variable one avoids a bang-type control structure and all its complications, e.g. controllability issues. On the other hand other control strategies might provide more control authority and could potentially reduce overall propellant usage. Nevertheless, we employ the thrust vectoring control concept to analyze the coupled attitude-orbital dynamics optimization problem of electric spacecraft.

Figure 6.1 illustrates several feasible control system designs for solar sail spacecraft. Probably the most straightforward way to control the attitude of the spacecraft is to apply a control torque g_u about the center of mass \bullet . Applying a control force \mathbf{f}_u instead slightly complicates the analysis since the force appears in the orbital equations, as well. However, note that in both cases the control variable appears linearly in the motion equations, which leads to bang-type control laws which in turn could potentially render the system uncontrollable for a plain minimum-time control problem. Using a combination of control force and torque or the implementation of symmetrically placed control vanes at the solar sail tips with control force \mathbf{f}_1 and \mathbf{f}_2 are possible ways to resolve

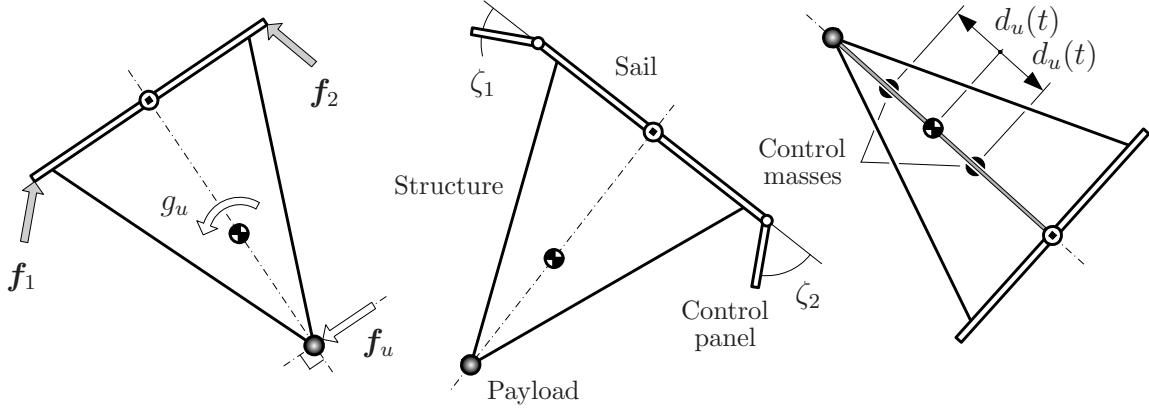


Figure 6.1: Spacecraft control system design comparison.

uncontrollability issues. One way to avoid the use of thrusters is to take advantage of the solar radiation pressure via control panels and choosing as the control variables the panel deflection angles ζ_1 and ζ_2 . The major drawback of this design probably concerns the structural integrity of the spacecraft. Furthermore, the achievable control torques are not only rather small but are also a function of the distance of the spacecraft from the Sun. An elegant approach to control the attitude of the spacecraft considers control masses which are displaced symmetrically from the center of mass by a distance $d_u(t)$. Note that the moments of inertia $I_1(d_u(t)) = I_2(d_u(t))$ are functions of the control mass displacement and the gravity gradient torque is $g_G \propto (I_1(d_u(t)) - I_3)$. Therefore, to be efficiently controllable the spacecraft would have to be designed about an inertially symmetric operating point d^{ref} such that an increase (decrease) of $d_u(t)$ results a negative (positive) torque g_G for a corresponding fixed orientation angle. Similar to the control panel concept the control mass approach suffers from a strongly varying control effectiveness ($\propto 1/r^3$). Also the structural maturity of the design is a major concern not to mention the increased spacecraft mass.

6.3 System models and motion equations

We consider a symmetric spacecraft system as illustrated in Figure 6.2. For solar sail spacecraft the payload is modelled as a point mass m_p connected rigidly to a perfectly flat and reflective square sail of mass m_s and surface area A . We define the body-fixed reference frame $\{\mathbf{b}_x, \mathbf{b}_y\}$ with the \mathbf{b}_x axis identifying the system symmetry axis and passing through the spacecraft system barycenter \bullet and the center of pressure \odot of

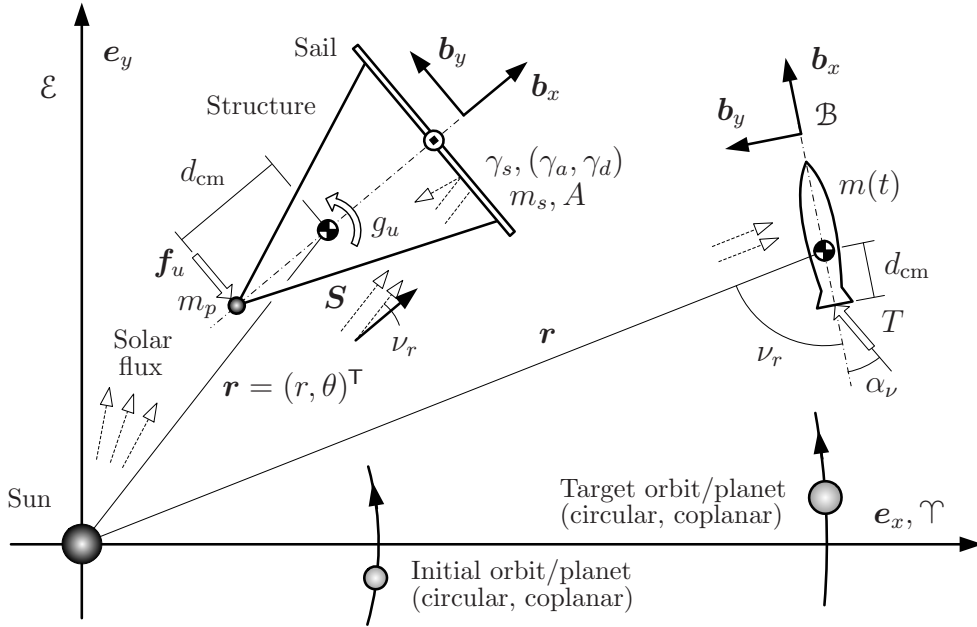


Figure 6.2: Interplanetary missions using solar sail spacecraft.

the solar sail. The distance between center of mass and center of pressure is d_s . The sail orientation angle ν_r is defined as the angle between the sail normal ($= \mathbf{b}_x$) and the solar flux direction \mathbf{S} . A positive angle rotates the \mathbf{b}_x anti-clockwise into \mathbf{S} . The sail orientation angle is controlled via a control force \mathbf{f}_u – or equivalently – the corresponding control torque g_u . For convenience, we define \mathbf{S}_\perp as the unit vector orthogonal to \mathbf{S} such that \mathbf{S}_\perp and \mathbf{b}_y are aligned for $\nu_r = 0$. The environmental forces and torques acting on the spacecraft system are due to the gravitational field and the solar radiation of the Sun. Electric spacecraft are controlled via thrust vectoring with a constant thrust force T and variable thrust vector control angle α_ν . Note that by appropriately changing α_ν both the spacecraft orientation angle ν_r and the spacecraft position $\mathbf{r} = (r, \theta)^T$ can be controlled.

Both system models are described using polar coordinates. The initial and target spacecraft trajectories are modelled as heliocentric, circular, and coplanar orbits. We define the generalized coordinate vector as $\mathbf{r} \triangleq (r, \theta, \nu_r)^T$ and the corresponding velocity vector as $\mathbf{v} \triangleq (v_r, v_\theta, \omega)^T$ where $v_r = \dot{r}$ and $v_\theta = r\dot{\theta}$. The angular rate of the spacecraft is defined as $\omega \triangleq \dot{\nu}_r$.

The motion equations for a solar sail spacecraft are then readily obtained by using the

equations of motion presented in Section 5.1.3 and attaching a set of differential equations describing the attitude dynamics of the system. In other words, let

$$\tilde{\nu}'_r = \tilde{\omega} \quad (6.1)$$

$$\tilde{\omega}' = [-3\tilde{\mu}_\odot(\tilde{I}_1 - \tilde{I}_3) \cos \tilde{\nu}_r \sin \tilde{\nu}_r / \tilde{r}^3 + \tilde{g}_\gamma + \tilde{g}_u] / \tilde{I}_2 \quad (6.2)$$

where the moments of inertia \tilde{I}_i are given by

$$\tilde{I}_1 = \tilde{I}_2 = \tilde{m}_s \tilde{A} / 12 + \tilde{m}_s \tilde{d}_s^2 + \tilde{m}_p \tilde{d}_{\text{cm}}^2 \quad \text{and} \quad \tilde{I}_3 = \tilde{m}_s \tilde{A} / 6 \quad (6.3)$$

with an overall spacecraft mass of $\tilde{m} = \tilde{m}_s + \tilde{m}_p$. The first term on the right-hand side of equation (6.2) is the gravity gradient torque as derived in Hughes and McInnes³⁸. The second and third terms in equation (6.2) account for the solar radiation torque and the control torque. By following the procedure outlined in Appendix B we end up with a set of nondimensional motion equations in the form

$$\dot{r} = v_r \quad (6.4)$$

$$\dot{\theta} = v_\theta / r \quad (6.5)$$

$$\dot{v}_r = v_\theta^2 / r - 1 / r^2 + \beta \cos^3 \nu_r / r^2 \quad (6.6)$$

$$\dot{v}_\theta = -v_r v_\theta / r + \beta \sin \nu_r \cos^2 \nu_r / r^2 \quad (6.7)$$

$$\dot{\nu}_r = \omega \quad (6.8)$$

$$\dot{\omega} = \zeta \cos \nu_r \sin \nu_r / r^3 + g_u \quad (6.9)$$

where ζ is the gravity gradient form factor and $\tilde{\zeta} = -3\tilde{\mu}_\odot(\tilde{I}_1 - \tilde{I}_3) / \tilde{I}_2$. Also note that for a perfectly reflective solar sail $\gamma_s = 1$ and therefore $g_\gamma = 0$.

The motion equations for a nuclear-electric spacecraft can be derived in a similar manner using the analysis from Section 5.1.1. However, we assume that unlike for solar sail spacecraft the dimensions of the electric spacecraft are truly “small”. As a result we neglect the influence of the gravity gradient torque g_G . The nondimensional motion equations for the spacecraft then result in

$$\dot{r} = v_r \quad (6.10)$$

$$\dot{\theta} = v_\theta / r \quad (6.11)$$

$$\dot{v}_r = v_\theta^2 / r - 1 / r^2 + \tau \cos(\nu_r + \alpha_\nu) \quad (6.12)$$

$$\dot{v}_\theta = -v_r v_\theta / r + \tau \sin(\nu_r + \alpha_\nu) \quad (6.13)$$

$$\dot{\tau} = \tau^2 \kappa \quad (6.14)$$

$$\dot{\nu}_r = \omega \quad (6.15)$$

$$\dot{\omega} = -\varphi \sin \alpha_\nu \quad (6.16)$$

In equation (6.16) we have introduced the specific thrust vector torque $\varphi = d_{\text{cm}}T/I_{\bullet}$ with I_{\bullet} denoting the moment of inertia about the spacecraft center of mass. Note that for both system models the angle θ is an ignorable coordinate and can therefore be eliminated from the analysis. The normalized boundary conditions describing the orbital dynamics for solar sail spacecraft (6.4–6.7) and nuclear-electric spacecraft (6.10–6.13) are

$$r(t_0) = 1 \quad \theta(t_0) = \text{free} \quad v_r(t_0) = 0 \quad v_{\theta}(t_0) = 1 \quad (6.17)$$

$$r(t_f) = r_f \quad \theta(t_f) = \text{free} \quad v_r(t_f) = 0 \quad v_{\theta}(t_f) = 1/\sqrt{r_f} \quad (6.18)$$

Boundary conditions for the differential equations defining the attitude dynamics result in

$$\begin{array}{l} \nu_r(t_0) = \pi/2 \quad \omega(t_0) = 0 \\ \nu_r(t_f) = \pi/2 \quad \omega(t_f) = 0 \end{array} \quad \text{or} \quad \begin{array}{l} \nu_r(t_0) = \nu_0^{\text{opt}} \quad \omega(t_0) = 0 \\ \nu_r(t_f) = \nu_f^{\text{opt}} / \text{free} \quad \omega(t_f) = 0 / \text{free} \end{array} \quad (6.19)$$

Additionally we have boundary conditions on the initial and final specific thrust τ for nuclear-electric spacecraft

$$\tau(t_0) = \tau_0 \quad \text{and} \quad \tau(t_f) = \text{free} \quad (6.20)$$

The first set of boundary conditions in equation (6.19) seems to be a natural way to set up the optimal control problem for a transfer between coplanar circular orbits. However, a different set of boundary conditions might provide more valuable information when comparing the transfer characteristics of the spacecraft for the two cases when attitude dynamics is taken into account and when only the orbital problem is considered. That is, using the optimal initial and terminal control angles ν_0^{opt} and ν_f^{opt} as obtained from the orbital control problem offers a fair approach to determine the effect of the attitude dynamics on, for example, the minimum transfer time. Alternatively, it might prove advantageous not to prescribe the final orientation angle and/or angular velocity. A matter of common knowledge, complex performance indices significantly complicate the numerical analysis and therefore we choose as the constraint at $t = t_f$

$$\boldsymbol{\psi}(\mathbf{x}(t_f), t_f) = (r(t_f) - r_f, v_r(t_f), v_{\theta}(t_f) - 1/\sqrt{r_f})^{\text{T}} = \mathbf{0} \quad (6.21)$$

and allow $\nu_r(t_f)$ and $\omega(t_f)$ to vary freely. In the next section we formulate the optimal control problem for solar sail and nuclear-electric spacecraft.

6.4 Optimal control analysis for solar sail spacecraft

In the following we present the optimality conditions for a system model assuming a rigid body representation for the solar sail spacecraft. To simplify the numerical analysis

a control torque g_u rather than a control force \mathbf{f}_u is chosen as the control input. As pointed out previously we are only interested in the case where $\gamma_s = 1$, that is, the perfectly reflective solar sail.

6.4.1 Spacecraft design parameters

The control performance of solar sail spacecraft depends critically on the specific design parameters. An important design criteria and also the most common performance metric is the characteristic acceleration $\tilde{\beta}$. To simplify the design process for our analysis we adopt the *one-third* rule as used in McInnes⁶¹ allocating one-third of the total system mass to the payload. We further assume that the remaining two-thirds of the spacecraft mass (solar sail, sail structures, deployment mechanism) are evenly distributed over the sail surface. With these assumptions the characteristic acceleration yields

$$\tilde{\beta} = \frac{2\tilde{A}\tilde{\rho}\gamma}{\tilde{m}} = \frac{2\tilde{\rho}\gamma}{3\tilde{\rho}} \quad \text{or, given } \tilde{\beta} : \quad \tilde{\rho} = \frac{2\tilde{\rho}\gamma}{3\tilde{\beta}} \quad (6.22)$$

where $\tilde{\rho}$ is the mass density of the solar sail. For a payload mass of $\tilde{m}_p = 50$ kg ($\tilde{m} = 3\tilde{m}_p = 150$ kg) and for typical characteristic accelerations of $\tilde{\beta} = 1$ mm/s² and 2 mm/s² the required sail mass densities result $\tilde{\rho} = 3.042$ g/m² and 1.5241 g/m² which is technically feasible according to McInnes.⁶¹ Table 6.1 summarizes the spacecraft design parameters for a 150 kg spacecraft and a square solar sail with surface area $\tilde{A} = \tilde{a}^2$.

The design parameter ς in equation (6.9) controls the geometry of the spacecraft system and therefore the sign of the gravity gradient torque for a fixed orientation angle. With the one-third/two-thirds mass allocation between the payload and the solar sail and denoting d as the payload-sail distance the dimensions of the spacecraft result $\tilde{d}_s = \tilde{d}/3$, $\tilde{d}_{\text{cm}} = 2\tilde{d}/3$, the moments of inertia become

$$\tilde{I}_1 = \tilde{I}_2 = 2\tilde{m}\tilde{A}/36 + 2\tilde{m}\tilde{d}^2/27 + 4\tilde{m}\tilde{d}^2/27 = \tilde{m}\tilde{A}/18 + 2\tilde{m}\tilde{d}^2/9, \quad \tilde{I}_3 = \tilde{m}_s\tilde{A}/9 \quad (6.23)$$

which yields for ς

$$\varsigma = -3 \frac{\tilde{I}_1 - \tilde{I}_3}{\tilde{I}_2} = -3 \frac{4\tilde{d}^2 - \tilde{A}}{4\tilde{d}^2 + \tilde{A}}, \quad \varsigma \in (\varsigma^{\min}, \varsigma^{\max}] = (-3, +3] \quad (6.24)$$

For $\varsigma < 0$ the symmetry axis is the minor axis and the gravity gradient torque is stabilizing for attitudes with $\nu_r = n\pi$, $n \in \mathbb{Z}$. The case of $\varsigma = 0$ corresponds to inertially symmetric spacecraft where $\tilde{I}_i = \tilde{I}$, $i = 1, 2, 3$; the gravity gradient torque is equal to zero. To

Table 6.1: Spacecraft design parameters for a 50 kg payload and a square solar sail.

| $\tilde{\beta}$ in mm/s ² | β nondimensional | $\tilde{\rho}$ in g/m ² | \tilde{A} in m ² | \tilde{a} in m |
|--------------------------------------|------------------------|------------------------------------|-------------------------------|------------------|
| 1.00000 | 0.16892 | 3.04200 | 16,436.5 | 128.205 |
| 2.00000 | 0.33784 | 1.52100 | 32,873.1 | 181.309 |

take into account the effect of the gravity gradient torque on the control performance we choose $\zeta^{\text{ref}} = +1$ as the reference value. Having analyzed design parameters for the solar sail spacecraft model we now proceed to derive optimality conditions for the spacecraft system.

6.4.2 Optimality conditions

With motion equations (6.4–6.9) the system Hamiltonian results in

$$\begin{aligned} \mathcal{H} = & \lambda_1 v_r + \lambda_2 v_\theta + \\ & \lambda_3 \left(\frac{v_\theta^2}{r} - \frac{1}{r^2} + \frac{\beta}{r^2} \cos^3 \nu_r \right) + \lambda_4 \left(-\frac{v_r v_\theta}{r} + \frac{\beta}{r^2} \cos^2 \nu_r \sin \nu_r \right) + \\ & \lambda_5 \omega + \lambda_6 \left(\zeta \sin \nu_r \cos \nu_r / r^3 + g_u \right) \quad [+\varepsilon g_u^2] \end{aligned} \quad (6.25)$$

Note that in equation (6.25) we have formulated two different minimization problems. The term in square brackets in the Hamiltonian generalizes the “pure” minimum-time problem to a minimum-time minimum-cost control problem. The weighing constant ε allows one to penalize excessive control cost relative to increased transfer time. Also, by choosing $\varepsilon \ll 1$ the minimum-time problem can easily be recovered. As a matter of fact, the bang-type control we obtain for the “pure” minimum-time problem renders the spacecraft uncontrollable. Therefore, the minimum-time problem can only be solved using the more general approach choosing ε appropriately.

Differentiating the system Hamiltonian with respect to the state vector we obtain for the

costate equations

$$\begin{aligned} \dot{\lambda}_1 = & \lambda_3 (2\beta \cos^3 \nu_r / r^3 + v_\theta^2 / r^2 - 2/r^3) + \lambda_4 (2\beta \sin \nu_r \cos^2 \nu_r / r^3 - v_r v_\theta / r^2) \\ & + \lambda_6 (3\zeta \cos \nu_r \sin \nu_r / r^4) \end{aligned} \quad (6.26)$$

$$\lambda_2 = \text{const.} \quad \begin{cases} = 0 & \text{iff } \theta(t_f) = \text{free} \\ \neq 0 & \text{iff } \theta(t_f) = \theta_f \end{cases} \quad (6.27)$$

$$\dot{\lambda}_3 = -\lambda_1 + \lambda_4 v_\theta / r \quad (6.28)$$

$$\dot{\lambda}_4 = -2\lambda_3 v_\theta / r + \lambda_4 v_r / r \quad (6.29)$$

$$\dot{\lambda}_5 = 3\lambda_3 \beta \sin \nu_r \cos^2 \nu_r / r^2 - \lambda_4 \beta (3 \cos^3 \nu_r - 2 \cos \nu_r) / r^2 - \lambda_6 \zeta \cos 2\nu_r / r^3 \quad (6.30)$$

$$\dot{\lambda}_6 = -\lambda_5 \quad (6.31)$$

Omitting the control cost term the control torque appears only linearly in the Hamiltonian and Pontryagin's Minimum Principle yields a bang-type structure for the optimal control law and logic

$$g_u^* = \begin{cases} g_u^{\min} & \text{if } \lambda_6 < 0 \\ g_u^{\max} & \text{if } \lambda_6 > 0 \\ \text{singular} & \text{if } \lambda_6 = 0 \end{cases} \quad \text{Standard minimum-time problem} \quad (6.32)$$

On the other hand, for the combined minimum-time minimum control cost problem the optimal control law results

$$g_u^* = -\lambda_6 / (2\varepsilon) \quad \text{Minimum-time minimum-cost problem} \quad (6.33)$$

which is considerably less complex than the control law (6.32).

Note that the optimal control law for the standard minimum-time problem (6.32) implies the possible existence of singular control arcs. In the following section we perform singular control arc analysis for the problem at hand.

6.4.3 Singular control arc analysis

The switching function \mathcal{S} is defined as

$$\mathcal{S} \triangleq \frac{\partial \mathcal{H}}{\partial u} \equiv \frac{\partial \mathcal{H}}{\partial g_u} \quad (6.34)$$

Using the control logic (6.32) the control is singular whenever $\mathcal{S} \equiv 0$ during a finite time interval. For a singular control arc, g_u is determined by successive differentiation

of the switching function until the control variable appears explicitly. Furthermore, it is required that \mathcal{S} be differentiated an even number of times for g_u to be optimal.⁸ Hence

$$g_u^{\otimes} = \arg \left\{ \left(\frac{d^{2j} \mathcal{S}}{dt^{2j}} \right) = 0 \right\}, \quad j \in \mathbb{N} \quad (6.35)$$

where we used the superscript notation \square^{\otimes} to denote the singular optimal control arc. In addition, Kelley's optimality condition⁸ has to be satisfied along an optimal singular subarc; that is,

$$(-1)^j \frac{\partial}{\partial g_u} \left(\frac{d^{2j} \mathcal{S}}{dt^{2j}} \right) \geq 0 \quad (6.36)$$

The first time derivative of the switching function yields $\dot{\mathcal{S}} = \dot{\lambda}_6 = -\lambda_5 \equiv 0$. It is also straightforward to show that the second time derivative results

$$\ddot{\mathcal{S}} \equiv \mathcal{S}^{(2)} = 0 \quad \rightarrow \quad [\lambda_4(3 \cos(2\nu_r) - 1) - 3\lambda_3 \sin(2\nu_r)] \cos \nu_r = 0 \quad (6.37)$$

At this point the algebra becomes increasingly involved. Setting the third time derivative of the switching function equal to zero, $\mathcal{S}^{(3)} = 0$, we find

$$\begin{aligned} & -12\lambda_1 r \cos \nu_r^2 \sin \nu_r \\ & + \lambda_3(3\omega r + 2v_\theta)[\cos \nu_r + 3 \cos(3\nu_r)] \\ & + \lambda_4\{\omega r[\sin \nu_r + 9 \sin(3\nu_r)] + 2 \cos \nu_r[v_r - 3v_r \cos(2\nu_r) + 3v_\theta \sin(2\nu_r)]\} = 0 \end{aligned} \quad (6.38)$$

Finally, taking the fourth time derivative of \mathcal{S} and setting the resulting expression equal to zero the control variable appears linearly (first term in the third line in equation (6.39)):

$$\begin{aligned} & -8\lambda_1 r^2 \cos \nu_r \{6\omega r[3 \cos(2\nu_r) - 1] + 3v_r \sin(2\nu_r) + 2v_\theta[3 \cos(2\nu_r) - 1]\} \\ & + 4\lambda_3 \{2 \cos \nu_r^2 \sin \nu_r [12 - 3\zeta - 8\beta \cos \nu_r + 9\zeta \cos(2\nu_r)] \\ & + 3r^3 \{g_u[\cos \nu_r + 3 \cos(3\nu_r)] - \omega^2[\sin \nu_r + 9 \sin(3\nu_r)]\} - 36rv_\theta^2 \cos \nu_r^2 \sin \nu_r \\ & + \omega r^2 \{3v_r[\cos \nu_r + 3 \cos(3\nu_r)] - 4v_\theta[\sin \nu_r + 9 \sin(3\nu_r)]\} \\ & + \lambda_4 \{-2 \cos \nu_r [4 - \zeta + 6\beta \cos \nu_r - 4(3 + 2\zeta) \cos(2\nu_r) + 2\beta \cos(3\nu_r) \\ & + 9\zeta \cos(4\nu_r)] + 4\omega^2 r^3 [\cos \nu_r + 27 \cos(3\nu_r)] + 4g_u r^3 [\sin \nu_r + 9 \sin(3\nu_r)] \\ & + 12\omega r^2 \{v_r[\sin \nu_r + 9 \sin(3\nu_r)] + 2v_\theta[\cos \nu_r + 3 \cos(3\nu_r)]\} \\ & - 8r \cos \nu_r \{v_r^2 [3 \cos(2\nu_r) - 1] - 3v_r v_\theta \sin(2\nu_r) + v_\theta^2 [1 - 3 \cos(2\nu_r)]\} = 0 \end{aligned} \quad (6.39)$$

Therefore, solving equation (6.39) for $g_u \rightarrow g_u^{\otimes}$ and using equations (6.37,6.38) the optimal singular control g_u^{\otimes} is of fourth order and is given by

$$\begin{aligned} g_u^{\otimes} = & \{36\omega^2 r^3 [3 - 12 \cos(2\nu_r) + \cos(4\nu_r)] \\ & - 3 \sin(2\nu_r)^2 \{13\beta \cos \nu_r + 3[6 - 6\zeta + 2(\zeta - 9) \cos(2\nu_r) + 5\beta \cos(3\nu_r)]\} \\ & + 8rv_\theta^2 [19 - 36 \cos(2\nu_r) + 9 \cos(4\nu_r)] \\ & - 72\omega r^2 [\cos(2\nu_r) - 3][v_r \sin(2\nu_r) + v_\theta - 3v_\theta \cos(2\nu_r)]\} / \\ & \{36r^3 \cos \nu_r [-7 \sin \nu_r + \sin(3\nu_r)]\} = 0 \end{aligned} \quad (6.40)$$

Note, that the optimal control on a singular control arc does not depend on any of the costates. Also, for orientation angles of $\nu_r = n\pi/2$, $n \in \mathbb{Z}$ the singular control law becomes, again, undefined.

6.5 Optimal control analysis for nuclear-electric spacecraft

With equations of motions (6.10–6.16) the system Hamiltonian is readily available. The costate differential equations are then given by

$$\dot{\lambda}_1 = -\lambda_2 v_\theta / r^2 + \lambda_3 (-2/r^3 + v_\theta^2 / r^2) + \lambda_4 (-v_r v_\theta / r^2) \quad (6.41)$$

$$\lambda_2 = \text{const.} \begin{cases} = 0 & \text{iff } \theta(t_f) = \text{free} \\ \neq 0 & \text{iff } \theta(t_f) = \theta_f \end{cases} \quad (6.42)$$

$$\dot{\lambda}_3 = -\lambda_1 + \lambda_4 v_\theta / r \quad (6.43)$$

$$\dot{\lambda}_4 = -\lambda_2 / r - 2\lambda_3 v_\theta / r + \lambda_4 v_r / r \quad (6.44)$$

$$\dot{\lambda}_5 = -\lambda_3 \cos(\nu_r + \alpha_\nu) - \lambda_4 \sin(\nu_r + \alpha_\nu) - 2\lambda_5 \tau \kappa \quad (6.45)$$

$$\dot{\lambda}_6 = \lambda_3 \tau \sin(\nu_r + \alpha_\nu) - \lambda_4 \tau \cos(\nu_r + \alpha_\nu) \quad (6.46)$$

$$\dot{\lambda}_7 = -\lambda_6 \quad (6.47)$$

To obtain the optimal control angle we set the first derivative of the Hamiltonina equal to zero, that is

$$\frac{\partial \mathcal{H}}{\partial \alpha_\nu} = -\lambda_3 \tau \sin(\nu_r + \alpha_\nu) + \lambda_4 \tau \cos(\nu_r + \alpha_\nu) - \lambda_6 \varphi \cos \alpha_\nu = 0 \quad (6.48)$$

After performing some trivial algebraic manipulations we find for the optimal thrust vector angle

$$\frac{\sin \alpha_\nu^*}{\cos \alpha_\nu^*} = \frac{-\lambda_3 \sin \nu_r + \lambda_4 \cos \nu_r - \lambda_6 \varphi / \tau}{\lambda_3 \cos \nu_r + \lambda_4 \sin \nu_r} \quad (6.49)$$

To remove sign and quadrant ambiguities associated with the tangent function we compute the second derivative of the Hamiltonian

$$\frac{\partial^2 \mathcal{H}}{\partial \alpha_\nu^2} = -\lambda_3 \tau \cos(\nu_r + \alpha_\nu) - \lambda_4 \tau \sin(\nu_r + \alpha_\nu) + \lambda_6 \sin \alpha_\nu > 0 \quad (6.50)$$

Following a similar line of argumentation as used in Chapter 5 we finally obtain the correct optimal thrust vector angle in the form

$$\alpha_\nu^* = \text{atan2} \left(\frac{+\lambda_3 \sin \nu_r - \lambda_4 \cos \nu_r + \lambda_6 \varphi / \tau}{-\lambda_3 \cos \nu_r - \lambda_4 \sin \nu_r} \right) \quad \text{with} \quad \alpha_\nu^* \in [0, 2\pi) \quad (6.51)$$

Note that $\alpha_\nu^* \in [0, 2\pi)$ since we have not constrained the thrust vector angle. In practice and in particular when using only a single thruster achievable thrust vector angles are constrained to lie in an interval $\alpha_\nu^* \in [\alpha_\nu^{\min}, \alpha_\nu^{\max}]$ with typical upper bounds of $\text{abs}(\alpha_\nu^{\min}) < \pi/2$ and $\text{abs}(\alpha_\nu^{\max}) < \pi/2$. Preliminary optimal control simulation results for constrained thrust vector angles show extremely poor convergence characteristics which we attribute to limited control authority. However, a more in-depth analysis is necessary to achieve a thorough understanding of the constrained thrust vector angle optimal control problem.

6.6 Simulation results

We obtained optimized solution trajectories for both solar sail spacecraft and nuclear-electric spacecraft with trajectory endpoint accuracies of $\|\boldsymbol{\psi}(\mathbf{x}(t_f), t_f)\| < 10^{-6}$ which corresponds to a mismatch, for example, in radial distance in the order of some tens of kilometers. Figures 6.3 and 6.4 show a typical simulation result for an Earth-to-Mars transfer for a solar sail spacecraft with high characteristic acceleration. Note that since $\varepsilon = 1$ we consider a mixed minimum-time minimum-cost control problem, which yields an increased transfer time of $T = 6.83254$ as compared to $T = 5.57134$ for the minimum-time problem obtained using the system model and analysis in Chapter 5. The difference in transfer time corresponds to approximately 73.32 days. Also note that since the final orientation angle and angular velocity are allowed to vary freely the spacecraft is rotating after completing the transfer. Comparing Figure 6.3 with the corresponding figure in the previous chapter (Figure 5.3) we observe a different system behavior, which comes as no surprise since with $\varepsilon = 1$ we do not solve a true minimum-time problem. Figure 6.4 shows Lagrange multipliers, angular velocity, and control torque as functions of time for the transfer illustrated in Figure 6.3. We first note the large magnitudes in λ_1 and λ_4 when compared to the remaining Lagrange multipliers.

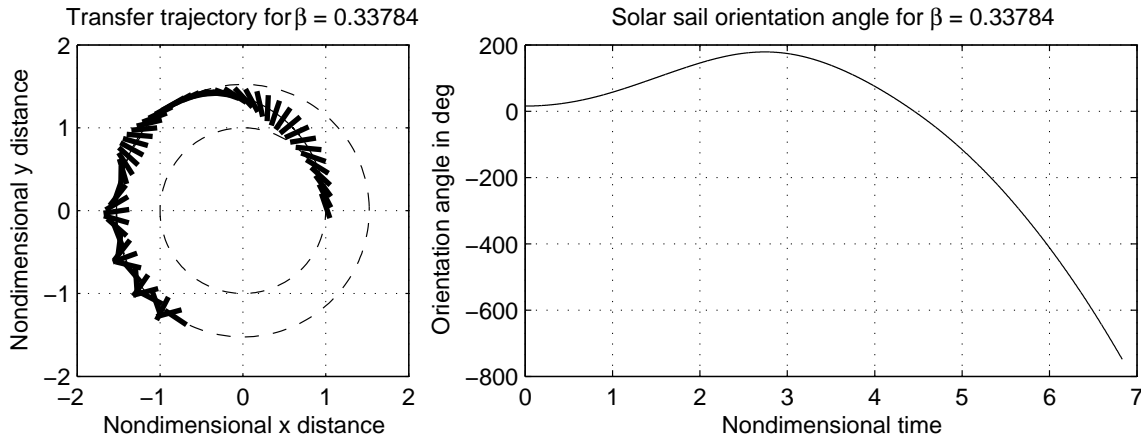


Figure 6.3: Transfer trajectory and solar sail orientation angle history for an Earth-to-Mars transfer. Simulation parameters are $\beta = 0.33784$, $\zeta = 1$, and $\varepsilon = 1$.

Figure 6.5 illustrates a minimum-time Earth-to-Mars transfer for a nuclear-electric spacecraft with $\tau_0 = 0.16892$, $\kappa = 0.50604$, and $\varphi = 1$, which corresponds to the simulation result shown in Figure 5.4. We first note a significant difference in transfer time. The transfer computed in Chapter 5 takes $T = 3.041$ TU; the transfer time for the current system model increases by more than 30% to $T = 3.981$ TU. The increase in transfer time can be explained with the relatively small value of $\varphi = 1$ for the specific thrust vector torque which is also reflected by the modest steering angle deflection; the spacecraft steering angle more or less points in the direction of the velocity vector at all times ($|\nu_r(t)| < 17^\circ$). In other words, the control force (or equivalently torque) in the present case is too small to cause substantial spacecraft rotation required to achieve a solution trajectory comparable to the one in Figure 5.4. Attempts to compute solution trajectories for significantly increased values of φ were not successful because of the sensitivity of the system with respect to variations in φ .

6.7 Summary and conclusions

The minimum-time transfer problem of solar sail and nuclear-electric spacecraft has been studied using a rigid-body representation to model the spacecraft. Even though the system models analyzed in Chapter 5 do provide an in-depth understanding of the physics of the minimum-time transfer problem more complex system descriptions are required to investigate engineering aspects of rotating spacecraft systems.

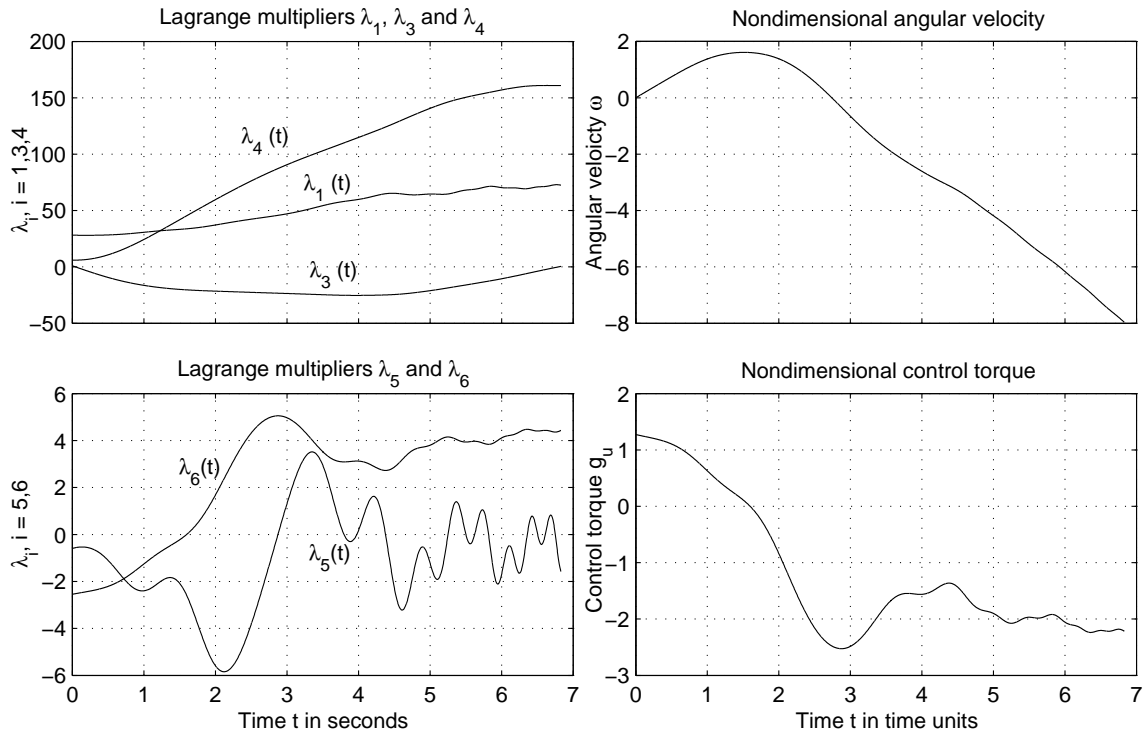


Figure 6.4: Lagrange multipliers λ_i , nondimensional angular velocity ω and control torque g_u as a function of time for an Earth-to-Mars transfer. Simulation parameters are $\beta = 0.33784$, $\zeta = 1$ and $\varepsilon = 1$.

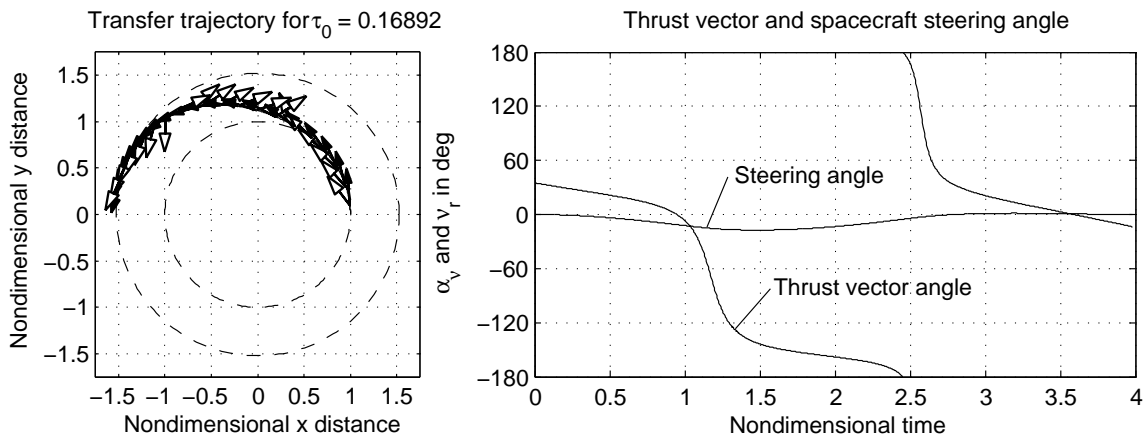


Figure 6.5: Transfer trajectory and thrust vector angle history for an Earth-to-Mars transfer for a nuclear-electric spacecraft with $\tau_0 = 0.16892$, $\kappa = 0.50604$, and $\varphi = 1$.

Several questions remain unanswered: Using a control torque the minimum-time problem for solar sail spacecraft results a bang-type control law which we believe renders the system uncontrollable. Also, simulation results indicate that singular control arcs are rare which leaves for the control law plain square-wave functions, which in turn raises the following question: Under which circumstances does a certain type of control law/logic render a system uncontrollable from an optimal control perspective? Another interesting question in that respect is: What can be said about the existence of singular control arcs for the case when the control on such a subarc does not depend on any of the costates but is a function of (some of) the states only?

Clearly the analysis presented in this chapter is far from being complete. Future work will include the verification of simulation results using available optimization tools such as EZopt⁸⁶ and DIDO.⁸² Both software packages have been used successfully by several researchers to solve a variety of optimal control problems. EZopt and DIDO solve optimization problems using a direct method, nevertheless, one of the most important features of DIDO is its capability to provide estimates for the Lagrange multipliers.²⁰

In addition, further analysis is necessary to investigate the influence of the spacecraft geometry (parameter ς) and the control parameter ε on optimal transfer time and control torque. For example for the solar sail spacecraft analysis and for small ε it should be possible to recover the control angle histories for the reduced system model which does not include spacecraft attitude dynamics.

Summary and Conclusions

We study the minimum-time optimal control problem of low-thrust spacecraft for interplanetary missions. The primary objective of this research effort is to implement and validate an efficient optimization algorithm based on numerical and analytical methods. The secondary research objective is to apply the optimization algorithm to the minimum-time transfer problem of spacecraft using different types of low-thrust propulsion technologies and to compare their performance with interplanetary mission scenarios. We consider nuclear-electric, solar-electric and solar sail spacecraft systems.

We employ unperturbed two-body system models of Sun and spacecraft neglecting the presence of other celestial bodies and other perturbative effects. The Sun is modeled as a point mass with spherically symmetric gravitation and solar radiation fields. Solar sail spacecraft are modelled as perfectly flat and perfectly reflective sails and are treated dynamically as point masses. Spacecraft with nuclear or solar electric propulsion systems are modeled as point masses with variable mass. Solar flux and available solar power are functions of the distance of the spacecraft from the Sun. The equations of motion for all spacecraft system models are described with respect to an inertial reference frame. For two-dimensional analysis we use polar coordinates with, and cartesian and spherical coordinates for three-dimensional system models.

The optimization problem is solved using an indirect method. The cascaded computational scheme is divided into three distinct optimization levels. On the first level a global statistical algorithm based on Adaptive Simulated Annealing is used to find an approximate guess for the Lagrange multipliers and the transfer time. The optimization parameters are then refined in the second level via local optimization methods using

Quasi-Newton and Newton methods. The third optimization level is formed by symmetry and homotopy methods. The key idea behind and novelty of the optimization algorithm is that a global optimization problem needs to be solved only for a single mission scenario, that is, for an arbitrary spacecraft system model and a given set of boundary conditions. Once an optimized trajectory has been obtained, we only use system symmetry and homotopy methods to generate additional optimal control solutions. These additional solution trajectories are not restricted to a particular type of spacecraft system model and can be obtained for arbitrary sets of boundary conditions of the states. The composite algorithm proves extremely efficient in finding highly accurate solutions to the minimum-time control problem.

We obtain optimal trajectories for several interrelated problem families that are described as Multi-Point Boundary Value Problems. We present and prove two theorems describing system symmetries for solar sail spacecraft and discuss symmetry properties and symmetry breaking for electric spacecraft systems models. We demonstrate how these symmetry properties can be used to significantly simplify the solution-finding process. For the minimum-time transfer between two planetary orbits with subsequent return transfer, only a Two-Point Boundary Value Problem has to be solved when using symmetry as opposed to the associated Three-Point Boundary Value Problem. Another system symmetry allows for efficient computation of solution trajectories by replacing a two-parameter continuation problem by a corresponding one-parameter continuation problem.

For fixed initial angular separation of the planets, we show that there exist in general an infinite number of locally optimal solutions but only one or two globally optimal solution trajectories. For both the two-dimensional and three-dimensional analysis these globally optimal solution trajectory are members of two distinctively different solution families. We show that two solution branches corresponding to the two solution families emanate from a common solution trajectory, the minimum-time orbit transfer trajectory. For decreasing values in initial angular separation between initial and target planet we find what we refer to as catch-up type trajectories, whereas for increasing values in initial angular separation so-called sleep-mode transfer solutions turn out to be more time-efficient. The two branches intersect an infinite number of times and in particular at the first crossover point, where the global optimum switches from sleep- to catch-up-type solution trajectories, and vice versa. A further increase or decrease in initial angular separation between origin and target objects yields locally optimal solutions, with faster, globally optimal solutions readily apparent.

Various extensions to the currently employed system models offer opportunities and chal-

lenges for future work. In this dissertation we briefly discuss the implementation of rigid-body representations for spacecraft and analyze system design and control issues related to the combined orbital/attitude dynamics system models. Several future deep-space missions are targeting orbits about the Sun-Earth-spacecraft Lagrangian points.^{46,47,48,49} To facilitate analyses for these missions, system descriptions based on Two-Body models are inadequate and have to be replaced with Three-Body models such as the Circular-Restricted Three-Body Problem (CR3BP). The motion equations of a spacecraft within the context of the CR3BP are moderately complex and give rise to an extremely challenging optimal control problem⁴⁵ which – to our best knowledge – has been addressed adequately in the literature only in the form of the so-called *Trajectory Correction Maneuver* (TCM) problem,^{23,44,45,59} a high-thrust optimal control problem.

Bibliography

- [1] E. L. Allgower and K. Georg. *Introduction to numerical continuation methods*. Society for Industrial and Applied Mathematics, 2003.
- [2] D. L. Bahls and S. W. Paris. A mission analysis tool for complex low thrust interplanetary missions. American Institute of Aeronautics and Astronautics and American Astronautical Society, 1980. Astrodynamics Conference, Danvers, Massachusetts.
- [3] R. R. Bate, D. D. Mueller, and J. E. White. *Fundamentals of Astrodynamics*. Dover, 1 edition, 1971.
- [4] H. Baumann and H. J. Oberle. Numerical computation of optimal trajectories for coplanar, aeroassisted orbital transfer. *Journal of Optimization Theory and Applications*, 107(3):457–479, December 2000.
- [5] J. T. Betts. Survey of numerical methods for trajectory optimization. *Journal of Guidance, Control, and Dynamics*, 21(2):193–207, March–April 1998.
- [6] J. T. Betts and S. O. Erb. Optimal low thrust trajectories to the Moon. *SIAM Journal of Applied Dynamical Systems*, 2(2):144–170, 2003.
- [7] G. W. Bluman and S. Kumei. *Symmetries and Differential Equations*. Springer-Verlag, 1 edition, 1989.
- [8] Jr. A. E. Bryson and Yu-Chi Ho. *Applied Optimal Control*. John Wiley & Sons, 1975. Revised Printing.
- [9] M. Budinich. A self-organising neural network for the Travelling Salesman Problem that is competitive with simulated annealing. *Neural Computations*, 8(2):416–424, February 1996.

-
- [10] J. B. Caillau, J. Gergaud, and J. Noailles. 3D geosynchronous transfer of a satellite: Continuation on the thrust. *Journal of Optimization Theory and Applications*, 118(3):541–565, September 2003.
- [11] G. E. Cameron and G. A. Herbert. System engineering of a nuclear electric propulsion testbed spacecraft. American Institute of Aeronautics and Astronautics, 1993. AIAA Joint Propulsion Conference and Exhibit, Monterey, California.
- [12] L. Casalino, G. Colasurdo, and D. Pastrone. Optimization procedure for preliminary design of opposition-class Mars missions. *Journal of Guidance, Control, and Dynamics*, 21(1):134–140, January–February 1998.
- [13] V. Cerny. A thermodynamical approach to the traveling salesman problem: An efficient simulation algorithm. *Journal of Optimization Theory and Applications*, 45(1):41–51, 1985.
- [14] F. R. Chang-Díaz, M. M. Hsu, E. Braden, I. Johnson, and T. F. Yang. Rapid Mars transits with exhaust-modulated plasma propulsion. Technical report, NASA, March 1995. NASA Technical Paper 3539.
- [15] C. Circi. Mars and Mercury missions using solar sails and solar electric propulsion. *Journal of Guidance, Control, and Dynamics*, 27(3):496–498, May–June 2004. Engineering Note.
- [16] G. Colasurdo and L. Casalino. Optimal control law for interplanetary trajectories with nonideal solar sail. *Journal of Spacecraft and Rockets*, 40(2):260–265, March–April 2003.
- [17] G. Colasurdo and L. Casalino. Optimal low-thrust maneuvers in presence of Earth shadow. American Institute of Aeronautics and Astronautics, 2004. AIAA/AAS Astrodynamics Specialist Conference and Exhibit, Providence, Rhode Island.
- [18] S. R. Dahlke and B. E. McKay. Optimal trajectories for secondary payloads from geosynchronous transfer orbits to the Moon. *The Journal of the Astronautical Sciences*, 50(1):1–15, January–March 2002.
- [19] T. N. Edelbaum. Optimum low-thrust rendezvous and station keeping. *Journal of Spacecraft and Rockets*, 40(6):1196–1201, November–December 2003.
- [20] F. Fahroo and M. Ross. Costate estimation by a Legendre Pseudospectral method. *Journal of Guidance, Control, and Dynamics*, 24(2):270–277, March–April 2001.

-
- [21] D. Fiehler and S. Oleson. A comparison of electric propulsion systems for Mars exploration. American Institute of Aeronautics and Astronautics, 2003. AIAA Joint Propulsion Conference and Exhibit, Huntsville, Alabama.
- [22] R. Fletcher. *Practical Methods of Optimization*, volume 1. John Wiley & Sons, 1980.
- [23] G. Gómez, M. Marcote, and J. J. Masdemont. Trajectory correction maneuvers in the transfer to libration point orbits. American Institute of Aeronautics and Astronautics, 2002. International Conference on Libration Point Orbits and Applications, Parador d'Aiguablava, Girona, Spain.
- [24] J. Gregory and C. Lin. *Constrained Optimization in the Calculus of Variations and Optimal Control Theory*. Van Nostrand Reinhold, 1992.
- [25] M. Guelman. Earth to Moon transfer with a limited power engine. American Institute of Aeronautics and Astronautics, 1994. AIAA/AAS Astrodynamics Specialist Conference, Scottsdale, Arizona.
- [26] M. Guelman. Earth to Moon transfer with a limited power engine. *Journal of Guidance, Control and Dynamics*, 18(5):1133–1138, 1995.
- [27] V. M. Guibout and D. J. Scheeres. Solving relative two-point boundary value problems: Spacecraft formation flight transfers application. *Journal of Guidance, Control, and Dynamics*, 27(4):693–704, July–August 2004.
- [28] P. Hajela. Non-gradient search methods for MDO – Status and future directions. American Institute of Aeronautics and Astronautics, 1997. AIAA/ASME/ASCE/AHS/ASC Structures, Structural Dynamics and Materials Conference, Kissimmee, Florida.
- [29] C. D. Hall and V. Collazo Perez. Minimum-time orbital phasing maneuvers. *Journal of Guidance, Control, and Dynamics*, 26(6):934–941, November–December 2003.
- [30] C. D. Hall and I. M. Ross. Dynamics and control problems in the deflection of near-Earth objects. In *Proceedings of the 1997 AIAA/AAS Astrodynamics Conference, Sun Valley, Idaho*, August 1997.
- [31] C. D. Hall and I. M. Ross. Optimal attitude control for coplanar orbit transfers. In *Proceedings of The John L. Junkins Astrodynamics Symposium, College Station, Texas*, May 2003.

-
- [32] C. R. Hargraves and S. W. Paris. Direct trajectory optimization using nonlinear programming and collocation. *Journal of Guidance, Control, and Dynamics*, 10(4):338–342, July–August 1987.
- [33] R. F. Hartl, S. P. Sethi, and R. G. Vickson. A survey of the maximum principles for optimal control problems with state constraints. *SIAM Review*, 37(2):181–218, June 1995.
- [34] J. W. Hartmann, V. L. Coverstone-Carroll, and S. N. Williams. Optimal interplanetary spacecraft trajectories via a pareto genetic algorithm. *The Journal of the Astronautical Sciences*, 46(3):267–282, July–September 1998.
- [35] J. W. Hartmann, V. L. Coverstone-Carroll, S. N. Williams, and W. J. Mason. Optimal interplanetary spacecraft trajectories via a pareto genetic algorithm. In *Proceedings of the 1998 AAS/AIAA Space Flight Mechanics Meeting, Monterey, California*, volume 99 of *Advances in the Astronautical Sciences*, pages 1439–1454, 1998.
- [36] J.W Hartmann, V. Coverstone-Carroll, and S. N. Williams. Generation of optimal spacecraft trajectories via a Pareto Genetic algorithm. *The Journal of the Astronautical Sciences*, 46(3):267–282, 1998.
- [37] A. L. Herman and D. B. Spencer. Optimal, low-thrust Earth-orbit transfers using higher-order collocation methods. *Journal of Guidance, Control, and Dynamics*, 25(1):40–47, January–February 2002.
- [38] G. W. Hughes and C. R. McInnes. Solar sail hybrid trajectory optimization. In *Proceedings of the 2001 AAS/AIAA Astrodynamics Specialist Conference, Quebec City, Quebec, Canada*, volume 109 of *Advances in the Astronautical Sciences*, pages 2369–2380, 2001.
- [39] R. W. Humble, G. N. Henry, and W. J. Larson. *Space Propulsion Analysis And Design*. McGraw-Hill, 1 edition, 1995.
- [40] L. Ingber and B. Rosen. Genetic Algorithms and Very Fast Simulated Reannealing: A comparison. *Mathematical and Computer Modelling*, 16(11):87–100, November 1992.
- [41] T. S. Jayaraman. Time-optimal orbit transfer trajectory for solar sail spacecraft. *Journal of Guidance and Control*, 3(6):536–542, November–December 1980.
- [42] J. A. Kechichian. Optimal low-thrust transfer using variable bounded thrust. *Acta Astronautica*, 36(7):357–365, 1995.

- [43] J. A. Kechichian. Optimal low-thrust rendezvous using equinoctial orbit elements. *Acta Astronautica*, 38(1):1–14, 1996.
- [44] J. A. Kechichian. The efficient computation of transfer trajectories between Earth orbit and l1 Halo orbit within the framework of the SunEarth restricted three body problem. In *Proceedings of the 2000 AAS/AIAA Space Flight Mechanics Meeting, Clearwater, Florida*, volume 105 of *Advances in the Astronautical Sciences*, pages 1159–1180, 2000.
- [45] J. A. Kechichian. Computational aspects of transfer trajectories to Halo orbits. *Journal of Guidance, Control and Dynamics*, 24(4):796–804, July–August 2001.
- [46] M. Kim and C. D. Hall. Lyapunov and Halo orbits around L2. In *Proceedings of the 2001 AAS/AIAA Astrodynamics Specialist Conference, Quebec City, Canada*, volume 109 of *Advances in the Astronautical Sciences*, pages 349–366, 2001.
- [47] M. Kim and C. D. Hall. Control of a rotating variable-length tethered system. In *Proceedings of the 2003 AAS/AIAA Astrodynamics Specialist Conference, Ponce, Puerto Rico*, volume 114 of *Advances in the Astronautical Sciences*, pages 1713–1732, 2003.
- [48] M. Kim and C. D. Hall. Dynamics and control of tethered satellite systems for NASA’s SPECS mission. In *Proceedings of the 2003 AAS/AIAA Astrodynamics Specialist Conference, Big Sky, Montana*, volume 116 of *Advances in the Astronautical Sciences*, pages 489–508, 2003.
- [49] M. Kim and C. D. Hall. Control of a rotating variable-length tethered system. *Journal of Guidance, Control and Dynamics*, 27(5):849–858, September–October 2004.
- [50] M. Kim and C. D. Hall. Symmetries in the optimal control of solar sail spacecraft. *Journal of Celestial Mechanics and Dynamical Astronomy*, 2005 (accepted for publication).
- [51] S. Kirkpatrick, C. D. Gelatt, Jr., and M. P. Vecchi. Optimization by Simulated Annealing. *Science*, 220(4598):671–680, May 1983.
- [52] C. A. Kluever. Geostationary orbit transfers using solar electric propulsion with specific impulse modulation. *Journal of Spacecraft and Rockets*, 41(3):461–466, May–June 2004.

- [53] C. A. Kluever and B. L. Pierson. Optimal low-thrust Earth-Moon transfers with a switching function. *The Journal of the Astronautical Sciences*, 42(3):269–284, July–September 1994.
- [54] V. Koblik, E. Polyakhova, and L. Sokolov. Controlled solar sail transfers into near-sun regions combined with planetary gravity-assist flybys. *Celestial Mechanics and Dynamical Astronomy*, 86(1):59–80, May 2003.
- [55] J. Krause. On the complete symmetry group of the classical Kepler system. *Journal of Mathematical Physics*, 35(11):5734–5748, November 1994.
- [56] F. L. Lewis and V. L. Syrmos. *Optimal Control*. John Wiley & Sons, 605 Third Avenue, New York, NY 10158-0012, 2 edition, 1995.
- [57] H. S. London. Some exact solutions of the equations of motion of a solar sail with constant sail setting. *American Rocket Society Journal*, 30:198–200, February 1960.
- [58] P. Lu and M. A. Khan. Nonsmooth trajectory optimization: An approach using continuous simulated annealing. *Journal of Guidance, Control, and Dynamics*, 17(4):685–691, July–August 1994.
- [59] D. L. Mains. Transfer trajectories from Earth parking orbits to l1 Halo orbits. Master’s thesis, Department of Aeronautics and Astronautics, Purdue University, May 1993.
- [60] T. T. McConaghy, T. J. Debban, A. E. Petropoulos, and J. M. Longuski. Design and optimization of low-thrust trajectories with gravity assists. *Journal of Spacecraft and Rockets*, 40(3):380–387, May–June 2003.
- [61] C. R. McInnes. *Solar Sailing: Technology, Dynamics, and Mission Applications*. Space Science and Technology. Springer, 1999. Published in association with Praxis Publishing.
- [62] C. R. McInnes. Payload mass fractions for minimum-time trajectories of flat and compound solar sails. *Journal of Guidance, Control, and Dynamics*, 23(6):1076–1078, November–December 2000.
- [63] P. B., Jr. Mendy. Multiple satellite trajectory optimization. Master’s thesis, Naval Postgraduate School, December 2004.
- [64] N. Metropolis, A. W. Rosenbluth, M. N. Rosenbluth, A. H. Teller, and E. Teller. Equation of state calculations by fast computing machines. *Journal of Chemical Physics*, 21(6):1087–1092, June 1953.

-
- [65] R. S. Nah and S. R. Vadali. Fuel-optimal, low-thrust, three-dimensional Earth-Mars trajectories. *Journal of Guidance, Control, and Dynamics*, 24(6):1100–1107, November–December 2001.
- [66] Sir Isaac Newton. *Philosophiae Naturalis Principia Mathematica*. London, 1 edition, 1687.
- [67] J. Nocedal and S. J. Wright. *Numerical Optimization*. Springer-Verlag, 1 edition, 1999.
- [68] M. C. Nucci. The complete Kepler group can be derived by Lie group analysis. *Journal of Mathematical Physics*, 37(4):1772–1775, April 1996.
- [69] H. J. Oberle and K. Taubert. Existence and multiple solutions of the minimum-fuel orbit transfer problem. *Journal of Optimization Theory and Applications*, 95(2):243–262, November 1997.
- [70] P. J. Olver. *Applications of Lie Groups to Differential Equations*. Springer-Verlag, 1 edition, 1986.
- [71] B. Paiewonsky. Optimal control: A review of theory and practice. *AIAA Journal*, 3(11):1985–2006, November 1965.
- [72] D. Pastrone, L. Casalino, and G. Colasurdo. Indirect optimization method for round-trip Mars trajectories. In *Proceedings of the 1995 AAS/AIAA Astrodynamics Specialist Conference, Halifax, Nova Scotia, Canada*, volume 90 of *Advances in the Astronautical Sciences*, pages 85–100, 1995.
- [73] M. Peot, S. Markcross, and M. Stephenfausett. Application of Simulated Annealing and genetic search to a Nonlinear Travelling Salesman Problem. pages 417–421. American Institute of Aeronautics and Astronautics, 1987. AIAA Guidance, Navigation and Control Conference, Monterey, California.
- [74] L. S. Pontryagin, V. G. Boltyanskii, R. V. Gamkrelidze, and E. F. Mishchenko. *The Mathematical Theory of Optimal Processes*. Wiley-Interscience, 1 edition, 1962. (Translated by Tiriogoff, K. N. and Neustadt, L. W., ed.).
- [75] M. Popescu. Applications of canonical transformations in optimizing orbital transfers. *Journal of Guidance, Control, and Dynamics*, 20(4):774–779, July–August 1997.
- [76] R. B. Powers and V. L. Coverstone. Optimal solar sail orbit transfers to synchronous orbits. *The Journal of the Astronautical Sciences*, 49(2):269–281, April–June 2001.

- [77] R. B. Powers, V. L. Coverstone-Carroll, and J. E. Prussing. Solar sail optimal orbit transfers to synchronous orbits. In *Proceedings of the 1999 AAS/AIAA Astrodynamics Specialist Conference, Girdwood, Alaska*, volume 103 of *Advances in the Astronautical Sciences*, pages 523–538, 1999.
- [78] J. E. Prussing. Optimal two- and three-impulse fixed-time rendezvous in the vicinity of a circular orbit. *Journal of Spacecraft and Rockets*, 40(6):952–959, November–December 2003.
- [79] I. M. Ross and F. Fahroo. Convergence of pseudospectral approximations for optimal control problems. In *Proceedings of the 2001 IEEE Conference on Decision and Control, Orlando, Florida*, December 2001.
- [80] I. M. Ross and F. Fahroo. A pseudospectral transformation of the covectors of optimal control systems. In *Proceedings of the First IFAC Symposium on Systems, Structures and Control, Prague, The Czech Republic*, August 2001.
- [81] I. M. Ross and F. Fahroo. A direct method for solving nonsmooth optimal control problems. In *Proceedings of the 2002 IFAC World Congress, Barcelona, Spain*, July 2002.
- [82] I. M. Ross and F. Fahroo. *User’s Manual for DIDO 2002: A MATLAB Application Package for Dynamic Optimization*. Department of Aeronautics and Astronautics, Naval Postgraduate School, Monterey, CA, June 2002. Technical report, NPS Technical Report, AA-02-002.
- [83] C. G. Sauer. Optimum solar-sail interplanetary trajectories. 1976. Paper presented at AIAA/AAS Astrodynamics Conference, San Diego, CA, AIAA Paper 76-792.
- [84] D. J. Scheeres, C. Park, and V. Guibout. Solving optimal control problems with generating functions. In *Proceedings of the 2003 AAS/AIAA Astrodynamics Specialist Conference, Big Sky, Montana*, volume 116 of *Advances in the Astronautical Sciences*, pages 1185–1206, 2003.
- [85] J. Schoenmaekers, D. Horas, and J. A. Pulido. SMART-1 with solar electric propulsion to the Moon. In *Proceedings of the 16th International Symposium on Space Flight Dynamics, Pasadena, California*, page 114, 2001.
- [86] H. Seywald and R. Kumar. *EZopt: An Optimal Control Toolkit*. Analytical Mechanics Associates, Inc., Hampton, VA, 1997.
- [87] H. Seywald and R. R. Kumar. Method for automatic costate calculation. *Journal of Guidance, Control, and Dynamics*, 19(6):1252–1261, November–December 1996.

-
- [88] H. Stephani. *Differential equations: Their solution using symmetry*. Cambridge University Press, 1 edition, 1989.
- [89] R. Stevens and M. Ross. Preliminary design of Earth-Mars cyclers using solar sails. In *Proceedings of the 2003 AAS/AIAA Space Flight Mechanics Meeting, Ponce, Puerto Rico*, volume 114 of *Advances in the Astronautical Sciences*, pages 2075–2088, 2003.
- [90] O. Tekinalp and M. Bingol. Simulated annealing for missile optimization: Developing method and formulation techniques. *Journal of Guidance, Control, and Dynamics*, 27(4):616–626, July–August 2004.
- [91] J. D. Thorne and C. D. Hall. Minimum-time continuous-thrust orbit transfers. *The Journal of the Astronautical Sciences*, 45(4):411–432, October–December 1997.
- [92] K. Tsander. From a scientific heritage. *NASA Technical Translation TTF-541*, 1967 (quoting a 1924 report by the author).
- [93] K. E. Tsiolkovsky. Extension of man into outer space. 1921. Cf. Also K. E. Tsiolkovskiy, Symposium on Jet Propulsion, No. 2, United Scientific and Technical Presses (NIT), 1936 (in Russian).
- [94] T. C. Tsu. Interplanetary travel by solar sail. *American Rocket Society Journal*, 29:422–427, June 1959.
- [95] Urabe. Numerical solution of multi-point boundary value problems in chebyshev series. Theory of the method. *Numerische Mathematik*, 9:341–366, July 1967.
- [96] M. Vasile. A global approach to optimal space trajectory design. In *Proceedings of the 2003 AAS/AIAA Space Flight Mechanics Meeting, Ponce, Puerto Rico*, volume 114 of *Advances in the Astronautical Sciences*, pages 629–648, 2003.
- [97] M. Vasile, R. Biesbroek, L. Summerer, A. Galvez, and G. Kminek. Options for a mission to Pluto and beyond. In *Proceedings of the 2003 AAS/AIAA Space Flight Mechanics Meeting, Ponce, Puerto Rico*, volume 114 of *Advances in the Astronautical Sciences*, pages 1569–1590, 2003.
- [98] J. Vlassenbroeck. A Chebyshev polynomial method for optimal control with state constraints. *Automatica*, 24(4):499–506, July 1988.
- [99] J. Vlassenbroeck and R. Van Dooren. A Chebyshev technique for solving nonlinear optimal control problems. *IEEE Transactions on Automatic Control*, 33(4):333–340, April 1988.

-
- [100] O. von Stryk and R. Bulirsch. Direct and indirect methods for trajectory optimization. *Annals of Operations Research*, 37:357–373, 1992.
- [101] S. N. Williams and V. Coverstone-Carroll. Mars missions using solar electric propulsion. *Journal of Spacecraft and Rockets*, 37(1):71–77, January–February 2000.
- [102] S. N. Williams and V. L. Coverstone-Carroll. Benefits of solar electric propulsion for the next generation of planetary exploration missions. *The Journal of the Astronautical Sciences*, 45(2):143–160, April–June 1997.
- [103] L. J. Wood, T. P. Bauer, and K. P. Zondervan. Comment on time-optimal orbit transfer trajectory for solar sail spacecraft. *Journal of Guidance, Control, and Dynamics*, 5(2):221–224, March–April 1982.
- [104] J. L. Wright. *Space Sailing*. Gordon and Breach Science Publishers, 1992. Second printing 1993.
- [105] A. Wuerl, T. Crain, and E. Braden. Genetic algorithm and calculus of variations-based trajectory optimization technique. *Journal of Spacecraft and Rockets*, 40(6): 882–888, November–December 2003.
- [106] C. L. Yen. Comparing solar sail and solar electric propulsions for propulsive effectiveness in deep space missions. In *Proceedings of the 2001 AAS/AIAA Space Flight Mechanics Meeting, Santa Barbara, California*, volume 108 of *Advances in the Astronautical Sciences*, pages 1587–1600, 2001.
- [107] A. N. Zhukov and V. N. Lebedev. Variational problem of transfer between heliocentric orbits by means of a solar sail. *Kosmicheskie Issledovaniya (Cosmic Research)*, 2:45–50, January–February 1964.
- [108] K. P. Zondervan, Wood L. J., and Caughey T. K. Optimal low-thrust, three-burn orbit transfers with large plane changes. *The Journal of the Astronautical Sciences*, 32(4):407–428, October–December 1984.

Optimal Control of Time-Continuous Systems

The optimal control problem is to find an optimal control input \mathbf{u}^* for a generally non-linear system $\dot{\mathbf{x}} = \mathbf{f}(\mathbf{x}, \mathbf{u}, t)$ such that the associated performance index

$$\mathcal{J} = \phi(\mathbf{x}(t_f), t_f) + \int_{t_0}^{t_f} \mathcal{L}(\mathbf{x}, \mathbf{u}, t) dt \quad (\text{A.1})$$

is minimized, and such that the constraint at final time t_f

$$\boldsymbol{\psi}_f = \boldsymbol{\psi}(\mathbf{x}(t_f), t_f) = \mathbf{0} \quad (\text{A.2})$$

is satisfied. In equations (A.1) and (A.2) \mathbf{x} is the n -dimensional state vector, \mathbf{u} is the m -dimensional control input, and ϕ and \mathcal{L} are the terminal and accumulated costs, respectively. Instead of solving a constrained optimization problem, it is advantageous to consider the corresponding unconstrained optimization problem using the augmented performance index

$$\mathcal{J}^+ = \phi(\mathbf{x}(t_f), t_f) + \boldsymbol{\nu}^\top \boldsymbol{\psi}(\mathbf{x}(t_f), t_f) + \int_{t_0}^{t_f} \{ \mathcal{L}(\mathbf{x}, \mathbf{u}, t) + \boldsymbol{\lambda}^\top (\mathbf{f}(\mathbf{x}, \mathbf{u}, t) - \dot{\mathbf{x}}) \} dt \quad (\text{A.3})$$

Defining the *Hamiltonian function* \mathcal{H} as

$$\mathcal{H}(\mathbf{x}, \mathbf{u}, t) = \mathcal{L}(\mathbf{x}, \mathbf{u}, t) + \boldsymbol{\lambda}^\top \mathbf{f}(\mathbf{x}, \mathbf{u}, t) \quad (\text{A.4})$$

we can rewrite equation (A.3) as

$$\mathcal{J}^+ = \phi(\mathbf{x}(t_f), t_f) + \boldsymbol{\nu}^\top \boldsymbol{\psi}(\mathbf{x}(t_f), t_f) + \int_{t_0}^{t_f} \{ \mathcal{H}(\mathbf{x}, \mathbf{u}, t) - \boldsymbol{\lambda}^\top \dot{\mathbf{x}} \} dt \quad (\text{A.5})$$

In order to obtain necessary optimality conditions we follow the analysis of Pontryagin et al.⁷⁴ and compute the first variation of the augmented performance index. For the sake of readability we omit the arguments of the functional terms in equation (A.5). The first variation of the augmented performance index then yields

$$\begin{aligned} \delta \mathcal{J}^+ &= [\phi_x + \boldsymbol{\nu}^\top \boldsymbol{\psi}_x] \delta \mathbf{x}|_{t_f} + [\phi_t + \boldsymbol{\nu}^\top \boldsymbol{\psi}_t] \delta t|_{t_f} + \delta \boldsymbol{\nu}^\top \boldsymbol{\psi}|_{t_f} + \\ &\quad [\mathcal{H} - \boldsymbol{\lambda}^\top \dot{\mathbf{x}}] \delta t|_{t_f} - [\mathcal{H} - \boldsymbol{\lambda}^\top \dot{\mathbf{x}}] \delta t|_{t_0} + \\ &\quad \int_{t_0}^{t_f} \{ \mathcal{H}_x^\top \delta \mathbf{x} + \mathcal{H}_u^\top \delta \mathbf{u} - \boldsymbol{\lambda}^\top \delta \dot{\mathbf{x}} + \delta \boldsymbol{\lambda}^\top [\mathcal{H}_\lambda - \dot{\mathbf{x}}] \} dt \end{aligned} \quad (\text{A.6})$$

where the subscripts x , u , and t denote differentiation with respect to \mathbf{x} , \mathbf{u} , and t respectively. By integrating by parts the term in equation (A.6) that depends on $\delta \dot{\mathbf{x}}$ we end up with the expression

$$\int_{t_0}^{t_f} \boldsymbol{\lambda}^\top \delta \dot{\mathbf{x}} dt = \boldsymbol{\lambda}^\top \delta \mathbf{x}|_{t_f} - \boldsymbol{\lambda}^\top \delta \mathbf{x}|_{t_0} - \int_{t_0}^{t_f} \dot{\boldsymbol{\lambda}}^\top \delta \mathbf{x} dt \quad (\text{A.7})$$

and equation (A.6) can be rewritten as

$$\begin{aligned} \delta \mathcal{J}^+ &= [\phi_x + \boldsymbol{\nu}^\top \boldsymbol{\psi}_x - \boldsymbol{\lambda}] \delta \mathbf{x}|_{t_f} + [\phi_t + \boldsymbol{\nu}^\top \boldsymbol{\psi}_t + \mathcal{H}] \delta t|_{t_f} + \\ &\quad \delta \boldsymbol{\nu}^\top \boldsymbol{\psi}|_{t_f} + \mathcal{H} \delta t|_{t_0} + \boldsymbol{\lambda}^\top \delta \mathbf{x}|_{t_0} + \\ &\quad \int_{t_0}^{t_f} \{ [\mathcal{H}_x + \dot{\boldsymbol{\lambda}}]^\top \delta \mathbf{x} + \mathcal{H}_u^\top \delta \mathbf{u} + [\mathcal{H}_\lambda - \dot{\mathbf{x}}]^\top \delta \boldsymbol{\lambda} \} dt \end{aligned} \quad (\text{A.8})$$

The necessary condition for the augmented performance index to be minimized is that the first variation of \mathcal{J}^+ equals zero, that is, $\delta \mathcal{J}^+ = 0$. The condition is satisfied by setting to zero the coefficients of the independent increments of $\delta \mathbf{x}$, δt , $\delta \boldsymbol{\nu}$, and $\delta \mathbf{u}$. Note that both t_0 and $\mathbf{x}(t_0)$ are assumed to be known (or fixed) and therefore their variations are equal to zero.

From equation (A.8) we derive the necessary conditions for \mathcal{J}^+ to be optimized as

$$\dot{\boldsymbol{\lambda}} = -\mathcal{H}_x \quad (\text{A.9})$$

$$\mathcal{H}_u = \mathbf{0} \quad (\text{A.10})$$

$$0 = [\phi_x + \boldsymbol{\nu}^\top \boldsymbol{\psi}_x - \boldsymbol{\lambda}] \delta \mathbf{x}|_{t_f} + [\phi_t + \boldsymbol{\nu}^\top \boldsymbol{\psi}_t + \mathcal{H}] \delta t|_{t_f} \quad (\text{A.11})$$

Equations (A.9) define the set of differential equations for the costate vector. The optimal control law follows from equations (A.10) and by considering the second derivative of the Hamiltonian with respect to the control variables to satisfy the convexity conditions. The boundary conditions for the final costates and final Hamiltonian are obtained from equation (A.11).

From a practical point of view the costate equations are only of secondary interest, however, need to be integrated simultaneously with the state equations since the optimal control law is a function of both state and costate equations. We note that the costates enter the augmented performance index linearly (equation (A.3)). As a result, the differential equations for the costates are linear with respect to the costates; the system of costate equations therefore offers one degree of scaling freedom (which is of course due to the underlying scaling symmetry of the system of costates). Scaling freedom “reduces” the number of unknown initial costates by one, since we can freely choose for one of the costates $\lambda_i(t_0) = c$. Note, however, that $\text{sign}(c)$ is undetermined.

For minimum-time problems described by autonomous systems, scaling freedom yields to a “true” dimensionality reduction of the unknown initial costates. To see this, let the time derivative of the Hamiltonian be given by

$$\dot{\mathcal{H}} = \mathcal{H}_t + \mathcal{H}_u^\top \dot{\mathbf{u}} + [\mathcal{H}_x + \dot{\boldsymbol{\lambda}}]^\top \mathbf{f} \quad (\text{A.12})$$

According to conditions (A.9) and (A.10) the second and third terms on the right-hand-side of equation (A.12) are equal to zero. For autonomous systems equation (A.12) therefore yields

$$\dot{\mathcal{H}} = \mathcal{H}_t = 0 \quad \text{or} \quad \mathcal{H} = \text{const.} \quad (\text{A.13})$$

For autonomous, minimum-time problems we can then conclude with condition (A.11) that

$$\text{const.} = \mathcal{H} \equiv \mathcal{H}|_{t_f} = -\phi_t|_{t_f} = -1 \quad \rightarrow \quad \mathcal{H} = \mathcal{H}(\mathbf{x}, \boldsymbol{\lambda}, \mathbf{u}) \equiv -1 \quad (\text{A.14})$$

In practice we can use equation (A.14) to compute one of the initial costates from the remaining $(n - 1)$ unknown costates.

In summary, the state and costate equations are given by

$$\dot{\mathbf{x}} = \frac{\partial \mathcal{H}}{\partial \boldsymbol{\lambda}} = \mathbf{f}(\mathbf{x}, \mathbf{u}, t) \quad \text{and} \quad \dot{\boldsymbol{\lambda}} = -\frac{\partial \mathcal{H}}{\partial \mathbf{x}} = -\frac{\partial \mathcal{L}(\mathbf{x}, \mathbf{u}, t)}{\partial \mathbf{x}} - \frac{\partial \mathbf{f}(\mathbf{x}, \mathbf{u}, t)}{\partial \mathbf{x}} \boldsymbol{\lambda} \quad (\text{A.15})$$

The optimal control law satisfies

$$\mathbf{u}^* = \arg \min_{\mathbf{u} \in \mathbf{U}} \mathcal{H}(\mathbf{x}^*, \boldsymbol{\lambda}^*, \mathbf{u}), \quad \forall t \geq 0 \quad (\text{A.16})$$

Equations (A.15) and (A.16), combined with a set of boundary conditions for the states yield a Two-Point Boundary Value Problem (TPBVP). The initial conditions of the costates $\boldsymbol{\lambda}(t_0)$ are the unknowns of the TPBVP and need to be chosen such that at $t = t_f$ the conditions on the states $\boldsymbol{\psi}_f = \mathbf{0}$ are satisfied.

By introducing additional interior-point constraints on the states we obtain a more general type of boundary value problem, termed Multi-point Boundary Value Problem (MP-BVP).

Interior-point constraints on the state variables

Interior-point constraints on the states frequently appear as a result of specific mission objectives in spacecraft transfer problems. In trajectory optimization problems interior-point constraints are treated similarly to end-point constraints, for example, let

$$\boldsymbol{\psi}_i = \boldsymbol{\nu}(\mathbf{x}(t_i), t_i) = \mathbf{0} \quad (\text{A.17})$$

in some intermediate time interval $t_0 < t_i < t_f$. The corresponding *extended augmented performance index* then assumes the form

$$\begin{aligned} \mathcal{J}^{\boxtimes} = & \phi(\mathbf{x}(t_f), t_f) + \boldsymbol{\nu}^T \boldsymbol{\psi}(\mathbf{x}(t_f), t_f) + \boldsymbol{\pi}^T \boldsymbol{\nu}(\mathbf{x}(t_i), t_i) + \\ & \int_{t_0}^{t_f} \{ \mathcal{H}(\mathbf{x}, \mathbf{u}, t) - \boldsymbol{\lambda}^T \dot{\mathbf{x}} \} dt \end{aligned} \quad (\text{A.18})$$

where $\boldsymbol{\pi}$ are the Lagrange multipliers associated with the interior-point constraints. The first variation of \mathcal{J}^{\boxtimes} then yields

$$\begin{aligned} \delta \mathcal{J}^{\boxtimes} = & [\phi_x + \boldsymbol{\nu}^T \boldsymbol{\psi}_x - \boldsymbol{\lambda}] \delta \mathbf{x} \Big|_{t_f} + \\ & \boldsymbol{\lambda}^T(t_i^+) - \boldsymbol{\lambda}^T(t_i^-) + \boldsymbol{\pi}^T \boldsymbol{\nu}_x \delta \mathbf{x} \Big|_{t_i} - \\ & \mathcal{H}(t_i^+) + \mathcal{H}(t_i^-) + \boldsymbol{\pi}^T \boldsymbol{\nu}_t \delta t \Big|_{t_i} + \boldsymbol{\lambda}^T \delta \mathbf{x} \Big|_{t_i} \\ & \int_{t_0}^{t_f} \{ [\mathcal{H}_x + \dot{\boldsymbol{\lambda}}]^T \delta \mathbf{x} + \mathcal{H}_u^T \delta \mathbf{u} + [\mathcal{H}_\lambda - \dot{\mathbf{x}}]^T \delta \boldsymbol{\lambda} \} dt \end{aligned} \quad (\text{A.19})$$

where t_i^- and t_i^+ signify immediate points in time just before and after $t = t_i$, respectively. In addition to conditions (A.9)–(A.11) we therefore obtain two additional jump conditions at the interior point:

$$\boldsymbol{\lambda}(t_i^-) = \boldsymbol{\lambda}(t_i^+) + \boldsymbol{\pi}^T \frac{\partial \boldsymbol{\nu}}{\partial \mathbf{x}(t_i)} \quad (\text{A.20})$$

$$\mathcal{H}(t_i^-) = \mathcal{H}(t_i^+) - \boldsymbol{\pi}^T \frac{\partial \boldsymbol{\nu}}{\partial t_i} \quad (\text{A.21})$$

Nondimensional Motion Equations

In this chapter we briefly demonstrate the process of obtaining non-dimensional motion equations with a solar sail spacecraft in the $1/r$ -gravitational field of the Sun and described with respect to a spherical reference frame.

The dimensional motion equations can be written as

$$\ddot{r} = r\dot{\theta}^2 \cos^2 \phi + r\dot{\phi}^2 - \frac{\mu_{\odot}}{r^2} + \frac{\beta}{r^2} \cos^3 \alpha_r \quad (\text{B.1})$$

$$\ddot{\theta} = -\frac{2\dot{\theta}\dot{r}}{r} + 2\dot{\theta}\dot{\phi} \tan \phi + \frac{\beta \cos^2 \alpha_r \sin \alpha_r \sin \alpha_{\phi\theta}}{r^3 r \cos \phi} \quad (\text{B.2})$$

$$\ddot{\phi} = -\frac{2\dot{\phi}\dot{r}}{r} - \dot{\theta}^2 \sin \phi \cos \phi + \frac{\beta \cos^2 \alpha_r \sin \alpha_r \cos \alpha_{\phi\theta}}{r^3} \quad (\text{B.3})$$

As a first step we transform the system of second-order differential equations into a system of first-order differential equations by introducing velocity-like variables v_r , v_{θ} , and v_{ϕ} and rename variables to indicate their dimensional character by choosing $\square \rightarrow \tilde{\square}$

$$\tilde{r}' = \tilde{v}_r \quad (\text{B.4})$$

$$\tilde{\theta}' = \tilde{v}_{\theta} \quad (\text{B.5})$$

$$\tilde{\phi}' = \tilde{v}_{\phi} \quad (\text{B.6})$$

$$\tilde{v}_r' = \tilde{r}(\tilde{\theta}')^2 \cos^2 \tilde{\phi} + \tilde{r}(\tilde{\phi}')^2 - \frac{\tilde{\mu}_{\odot}}{\tilde{r}^2} + \frac{\tilde{\beta}}{\tilde{r}^2} \cos^3 \tilde{\alpha}_r \quad (\text{B.7})$$

$$\tilde{v}_{\theta}' = -\frac{2\tilde{\theta}'\tilde{r}'}{\tilde{r}} + 2\tilde{\theta}'\tilde{\phi}' \tan \tilde{\phi} + \frac{\tilde{\beta} \cos^2 \tilde{\alpha}_r \sin \tilde{\alpha}_r \sin \tilde{\alpha}_{\theta\phi}}{\tilde{r}^3 \tilde{r} \cos \tilde{\phi}} \quad (\text{B.8})$$

$$\tilde{v}_{\phi}' = -\frac{2\tilde{\phi}'\tilde{r}'}{\tilde{r}} - (\tilde{\theta}')^2 \sin \tilde{\phi} \cos \tilde{\phi} + \frac{\tilde{\beta}}{\tilde{r}^3} \cos^2 \tilde{\alpha}_r \sin \tilde{\alpha}_r \cos \tilde{\alpha}_{\theta\phi} \quad (\text{B.9})$$

Note that we have also replaced the time derivative $\dot{\square}$ by its dimensional equivalent $\tilde{\square}' \equiv (d/d\tilde{t})\tilde{\square}$. The original variable names and the dot-notation for the time derivative will be used subsequently for the non-dimensional system description.

Step number two of the non-dimensionalization procedure involves choosing a specific non-dimensionalization for distance, time, and angle measures and expressing the non-dimensional time derivative as a function of the dimensional time derivative, that is

$$\tilde{r} = r \text{ AU}, \quad \text{and} \quad \tilde{t} = t \text{ TU}, \quad \rightarrow \quad \frac{d}{d\tilde{t}} = \frac{d}{dt} \frac{dt}{d\tilde{t}} = \frac{d}{dt} \frac{1}{\text{TU}} \quad (\text{B.10})$$

In equations (B.10) we have chosen 1 AU (one astronomical unit) as the representative length unit. The time unit 1 TU will be determined as part of the subsequent analysis. By limiting angular variables to be within the interval $[0, 2\pi)$ (or a subset thereof) we can simply choose 1 rad as the scaling factor to nondimensionalize angles, in other words, $[\tilde{\theta}] = [\theta]$ since $\tilde{\theta} = \mathcal{O}(1)$, for example. With the above non-dimensionalization we obtain for the time derivatives of the generalized coordinates

$$\dot{r} = \tilde{v}_r \frac{\text{TU}}{\text{AU}} \triangleq v_r \quad (\text{B.11})$$

$$\dot{\theta} = \tilde{v}_\theta \text{ TU} \triangleq v_\theta \quad (\text{B.12})$$

$$\dot{\phi} = \tilde{v}_\phi \text{ TU} \triangleq v_\phi \quad (\text{B.13})$$

Transforming equation (B.7) into its non-dimensional counterpart we find

$$\dot{v}_r \frac{\text{AU}}{\text{TU}^2} = r \text{ AU} \frac{v_\theta^2}{\text{TU}^2} \cos^2 \phi^2 + r \text{ AU} \frac{v_\phi^2}{\text{TU}^2} - \frac{\tilde{\mu}_\odot}{r^2 \text{ AU}^2} + \frac{\tilde{\beta}}{r^2 \text{ AU}^2} \cos^3 \alpha_r \quad (\text{B.14})$$

which simplifies to

$$\dot{v}_r = r v_\theta^2 \cos^2 \phi^2 + r v_\phi^2 - \frac{1}{r^2} + \frac{\beta}{r^2} \cos^3 \alpha_r \quad (\text{B.15})$$

by choosing

$$\frac{\tilde{\mu}_\odot \text{ TU}^2}{\text{AU}^3} = 1, \quad \rightarrow \quad \text{TU} = \sqrt{\frac{\text{AU}^3}{\tilde{\mu}_\odot}} \quad \text{and} \quad \frac{\tilde{\beta} \text{ TU}^2}{\text{AU}^3} = \beta \quad (\text{B.16})$$

Note that the angular rate of a spacecraft on a 1 AU, planar, circular orbit about the Sun equals $\tilde{v}_\theta = \sqrt{\tilde{\mu}_\odot/\text{AU}^3}$ which corresponds to a nondimensional value of $v_\theta = \tilde{v}_\theta \text{ TU} = \sqrt{\tilde{\mu}_\odot/\text{AU}^3} \sqrt{\text{AU}^3/\tilde{\mu}_\odot} = 1$ according to equations (B.12) and (B.16).

Having both distance and time units available, we find corresponding expressions for the remaining equations (B.8,B.9). The entire set of non-dimensional motion equation then

results in

$$\dot{r} = v_r \tag{B.17}$$

$$\dot{\theta} = v_\theta \tag{B.18}$$

$$\dot{\phi} = v_\phi \tag{B.19}$$

$$\dot{v}_r = rv_\theta^2 \cos^2 \phi + rv_\phi^2 - \frac{1}{r^2} + \frac{\beta}{r^2} \cos^3 \alpha_r \tag{B.20}$$

$$\dot{v}_\theta = -\frac{2v_\theta v_r}{r} + 2v_\theta v_\phi \tan \phi + \frac{\beta \cos^2 \alpha_r \sin \alpha_r \sin \alpha_{\phi\theta}}{r^3 \cos \phi} \tag{B.21}$$

$$\dot{v}_\phi = -\frac{2v_\phi v_r}{r} - v_\theta^2 \sin \phi \cos \phi + \frac{\beta}{r^3} \cos^2 \alpha_r \sin \alpha_r \cos \alpha_{\phi\theta} \tag{B.22}$$

Comparing the set of nondimensional motion equations to the dimensional counterparts we notice that the nondimensional set operates with a reduced number of system parameters – the system behavior apparently does not depend on μ_\odot , the heliocentric gravitational constant.

Orbital Elements and Cartesian Coordinates

Orbital elements are frequently used in astrodynamics application to describe the configuration of satellite systems. One of the major advantages of using an orbital element description is that for unperturbed two-body motion five orbital elements are constants of motion. For satellite formations and – in particular – relative satellite dynamics problems, the usage of orbital elements proves beneficial, as well. For example, for the case of an uncontrolled formation of two spacecraft in an unperturbed $1/r$ -gravitational field the orbital element barycenter performs Keplerian motion, which is not the case for the true center of mass (see Figure C.1).

To be able to use both cartesian coordinates and the set of orbital elements we briefly review coordinate mappings between the two system descriptions. Let $\mathbf{\Gamma} : \mathbb{R}^6 \rightarrow \mathbb{R}^6$ be the nonlinear mapping that transforms orbital elements $\boldsymbol{\alpha e}$ into Cartesian orbit position and velocity coordinates \boldsymbol{x} , that is,

$$\boldsymbol{x} = \mathbf{\Gamma}(\boldsymbol{\alpha e}), \quad \text{where} \quad \boldsymbol{x} \triangleq (\boldsymbol{r}, \boldsymbol{v}), \quad \boldsymbol{v} = \dot{\boldsymbol{r}} \tag{C.1}$$

The coordinates transformations $\boldsymbol{r}(\boldsymbol{\alpha e})$ and $\dot{\boldsymbol{r}}(\boldsymbol{\alpha e})$ can be written as

$$\boldsymbol{r} = r \mathbf{R}(\Omega, i, \omega) \begin{pmatrix} \cos f \\ \sin f \\ 0 \end{pmatrix} \quad \text{and} \quad \boldsymbol{v} = \sqrt{\frac{\mu}{p}} \mathbf{R}(\Omega, i, \omega) \begin{pmatrix} -\sin f \\ e + \cos f \\ 0 \end{pmatrix} \tag{C.2}$$

where

$$r = \frac{p}{1 + e \cos f}, \quad p = a(1 - e^2), \quad \text{and} \quad f = f(M, e) \tag{C.3}$$

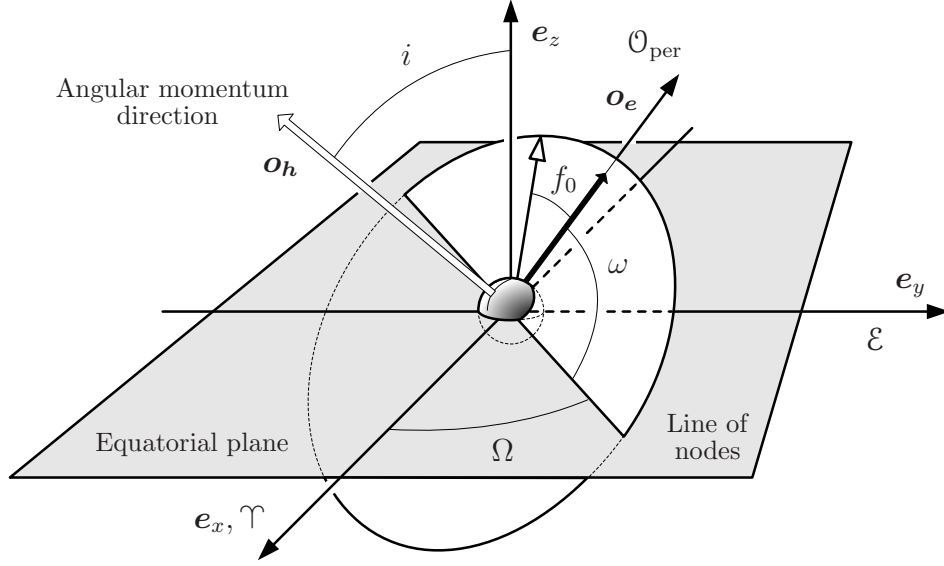


Figure C.2: Orbital elements.

The semi-major axis is readily available via the specific energy of the orbit

$$a = -\frac{\mu}{2E}, \quad E = \frac{v^2}{2} - \frac{\mu}{r} \quad (\text{C.6})$$

The eccentricity vector and eccentricity of the orbit result in

$$e = \|\mathbf{e}\|, \quad \text{where} \quad \mathbf{e} = (e_x, e_y, e_z)^\top = \frac{1}{\mu} \left[\left(v^2 - \frac{\mu}{r} \right) \mathbf{r} - (\mathbf{r}^\top \mathbf{v}) \mathbf{r} \right] \quad (\text{C.7})$$

The three rotational angles i , Ω , and ω are readily available with Figure C.2 and result in

$$\cos i = \frac{h_x}{\|\mathbf{h}\|}, \quad \cos \Omega = n_x, \quad \cos \omega = \frac{\mathbf{n}^\top \mathbf{e}}{e}, \quad (\text{C.8})$$

Note that the inclination is defined within the interval $i \in [0, \pi)$ and therefore the expression for the inclination in equation (C.8) is well defined. For the right ascension of the ascending node we see that $\Omega \in [0, \pi)$ if $n_y > 0$ and $\Omega \in [\pi, 2\pi)$ otherwise. Similarly, $\omega \in [0, \pi)$ if $e_z > 0$ and $\omega \in [\pi, 2\pi)$ otherwise. The true anomaly epoch angle f_0 is simply the angle between \mathbf{e} and the position vector \mathbf{r} , therefore

$$\cos f_0 = \frac{\mathbf{e}^\top \mathbf{r}}{er} \quad (\text{C.9})$$

Note that $f_0 \in [0, \pi)$ if $\mathbf{r}^\top \mathbf{v} > 0$ and $f_0 \in [\pi, 2\pi)$ otherwise.

It has been well documented in the literature that orbital elements exhibit singularities for zero eccentricity and inclinations of $i = 0, \pi$. In addition, the semi-major axis changes discontinuously for orbits with $e = 1$. To eliminate these deficiencies, a modified set of equinoctial orbit elements is frequently used in the literature.^{6,37,43} For our analysis classical orbital elements are adequate since they are used exclusively as a means to define boundary conditions.

Vita

Mischa Kim was raised in the picturesque small town of Feldkirch, Austria, where he graduated from Höhere Technische Bundeslehr- und Versuchsanstalt, Rankweil in 1994. He joined the Austrian Armed Forces that same year and began his university education as a physics major at Technische Universität Wien in 1995.

During his senior year Mischa achieved a once-in-a-lifetime opportunity to study aerospace engineering as an international exchange student at Virginia Tech, Blacksburg, home to the “Fighting Gobblers” and, quite possibly, world’s strongest coffee. After graduating as a *Diplomingenieur der technischen Physik* from Technische Universität Wien in March 2001 he accepted a research assistantship to attend graduate school at Virginia Tech. Mischa earned a M.S. in aerospace engineering in December 2003 and defended his Ph.D. on April 18, 2005.

After graduation Mischa will be moving out west to the Grand Canyon State to join the faculty of the Department of Aerospace Engineering at Embry-Riddle Aeronautical University, Prescott.